OPTIMIZATION OF A SEGS SOLAR FIELD FOR COST EFFECTIVE POWER OUTPUT

A Thesis Presented to
The Academic Faculty

By

Robert W. Bialobrzeski

In Partial Fulfillment
Of the Requirements for the Degree
Master of Science in Mechanical Engineering

Georgia Institute of Technology

August, 2007

OPTIMIZATION OF A SEGS SOLAR FIELD FOR COST EFFECTIVE POWER OUTPUT

Approved by:

Dr. Sheldon M. Jeter, Advisor
School of Mechanical Engineering
Georgia Institute of Technology

Dr. Srinivas Garimella
School of Mechanical Engineering
Georgia Institute of Technology

Dr. Samuel V. Shelton
Provost-VP Academic Affairs
Georgia Institute of Technology

Date Approved: July 6, 2007

ACKNOWLEDGMENTS

The author would like to thank Dr. Sheldon Jeter, of the School of Mechanical Engineering at Georgia Tech., for his continued support throughout the course of this project. In addition, the author extends thanks to Florida Power and Light for their financial support of the research presented herein, and to the personnel at SEGS units VIII and IX, in particular Mike Keller, for their contributions to this study.

TABLE OF CONTENTS

LIST OF TABLES

LIST OF FIGURES

SUMMARY

This thesis presents and demonstrates procedures to model and optimize the collector field of a parabolic trough solar thermal power plant. The collector field of such a plant is universally organized into parallel loops of solar collectors. Heat transfer fluid returning from the energy conversion plant is heated to a moderately high temperature in the field. Typically fluid enters a collector loop around 270 °C and leaves at 380 °C. The fluid is then returned to the plant to generate steam. In the first part of this thesis, the collector field and the energy conversion system of a typical parabolic trough solar thermal power plant are modeled. The model is compared with actual performance data and is enhanced and verified as necessary.

Originally, the collectors in the plants under consideration were provided with evacuated tube receivers of the highest feasible efficiency without much regard for cost effectiveness. In practice, these receivers have failed at an unexpected rate and need replacement. It is unlikely that a very expensive evacuated tube receiver is now the most cost effective for every location in a collector loop. In particular, a receiver optimized for 270 °C operation may not be optimal at 380 °C. For example, a relatively inexpensive receiver with a flat black absorber and no vacuum may be more cost effective in the lower temperature segments of a loop. In the second part of this thesis, a procedure for the optimum deployment of collectors is developed and demonstrated. The results of this research should be directly applicable to the refurbishment and upgrading of several of the largest solar energy plants in the world.

CHAPTER 1: INTRODUCTION

1.1 PROJECT OVERVIEW

The Solar Electric Generating Stations (SEGS) are solar thermal power plants located in the Mojave Desert in Southern California, and have been in operation since the early 1990's. They represent "the only large-scale commercial deployment of solar thermal power plant technologies to date" in the United States [Price, 1999]. These plants harness radiation energy from the sun to produce the steam necessary for electricity generation, an emission-free process that uses a completely renewable energy source. The plants also use a considerable amount of natural gas fuel as a supplemental heat source, but the majority of the heat comes from the solar thermal process. The environmental benefits of solar thermal power have, up to this point, been overshadowed by the high cost of equipment and maintenance involved with the technology. Luz International Limited, the pioneering entity of large-scale solar thermal power, built nine SEGS facilities between 1984 and 1990. Subsequently, in 1991, Luz succumbed to economic pressures, primarily from decreasing energy prices, and declared bankruptcy [Price, 1999]. The original nine SEGS plants remained in operation, but no development of new SEGS facilities was undertaken in the United States for over 10 years after Luz went under. Only recently, within the last few years, have new projects been put into motion and development of similar parabolic trough plants begun again.

This thesis will present the results of an extensive monitoring and modeling study of SEGS unit VIII, as well as a method of improving the collector field design of a SEGS plant to maximize the economic benefit of power production. Design improvements can be used in the refurbishment of current SEGS units or in the development of new facilities in the future. The study explores the concept that the best collector field design will incorporate a combination of collector types with different efficiencies and costs. The project is divided into two main parts. First, the solar field and energy conversion plant of a typical SEGS unit are modeled with the help of extensive data collected from SEGS unit VIII. The energy

conversion plant consists of a Rankine steam turbine/generator cycle that uses the heat collected by the solar field to drive steam generation. Modeling focuses primarily on the solar collectors and incorporates data obtained directly from the facility during normal operation in conjunction with theoretical calculations of proposed new collectors. The second part of the project involves optimization of the solar field design for maximum life-cycle benefit. This is achieved by modeling the plant's output under various combinations of collector types in the field and comparing the benefits and costs of each arrangement.

1.2 BASICS OF SOLAR THERMAL/CONCENTRATING SOLAR POWER

The SEGS plants are similar to any other steam generation power plant, in that they use heat to produce steam which drives a turbine to generate electricity. However, instead of burning fuel to produce the required heat, solar thermal plants harness energy from the sun to heat oil, which is then used to superheat the steam flowing into the turbine generator. Parabolic trough collectors are used to concentrate solar radiation at high intensities onto an absorber pipe, through which the heat transfer fluid (HTF) flows, to heat the fluid to the necessary temperature. Natural gas fired heaters are installed in the plant and used to supplement the solar field at times of high energy demand or insufficient sunlight. Data from SEGS VIII shows that less than 15% of the total annual heat delivered to the plant is from natural gas. The measured annual performance data of this unit is summarized in Table 1.2.1.

Table 1.2.1: Summary of Annual SEGS VIII Plant Performance Data

Gross Electric Power Generated (MW-hr)	Net Electric Power Generated (MW-hr)	Solar Field Heat Generated (MW-hr)	Gas Heater Heat Generated (MW-hr)	Total Heat to Conversion Plant (MW-hr)	Plant Conversion Efficiency
149,643	138,212	438,605	61,250	499,855	0.414

By the year 2000, after Sandia national labs and the Department of Energy developed new solutions for improved operations and efficiency of the SEGS facilities, the nine units had a combined peak capacity of over 350 MW and were able to service the energy needs of about 500,000 citizens [D.O.E., 2000].

In spite of the recent shift in research efforts toward photovoltaic collectors for large-scale power, linear parabolic trough solar thermal technology remains a viable alternative that warrants further research. Several similar plants are currently being built in different parts of the World. Solargenix, in conjunction with NREL (National Renewable Energy Laboratory) and EERE (Engineering Efficiency and Renewable Energy), is in the process of building a 64 MW plant in El Dorado Valley, NV, which is the first new step toward the Western Governors Association and EERE goal of 1000 MW of concentrating solar power in the southwest region by 2010. In Grenada, Spain two 50 MW plants are being built by Solar Millennium, and a 150 MW unit is being developed in the Negev Desert in Israel by Solel, which includes plans to expand to 500 MW of output capacity [Parabolic Trough Solar, 2005].

The current actual and future estimated costs of electricity from concentrator solar power (CSP) plants, such as SEGS, appear to be competitive with photovoltaic systems, which is the principal alternative for large scale power production by direct use of solar energy. The US Department of Energy (DOE) recently estimated that current costs of solar PV electricity are in the range of 13 to 22 cents/kW-hr and further estimates that continued support of research and development might reduce costs to the range of 9 to 18 cents/kW-hr in 2010 [US DOE, 2006]. The assumptions underlying this estimate were not stated and may be optimistic. In any event, since the US DOE is committed to support of PV technology at a high level, it is unlikely that this is an invidiously high cost estimate. This project's sponsor reasonably considers data on costs to produce CSP electricity at the SEGS plants to be highly proprietary information; however, information from open sources is available. A National Research Council report (NRC, 2002), which is otherwise critical of CSP, quotes DOE sources as estimating the current cost of CSP electricity at 11–12 cents/kW-hr, and the report further states that industry analysts suggested the costs to be about 16 cents/kW-hr. One can reasonably assume that current costs for CSP electricity are 11 to 16 cents/kW-hr, while

current costs of PV electricity are somewhat higher at 13 to 22 cents/kW-hr. In fact, the US DOE has recently reversed a trend to only minimally fund CSP research and announced a program to provide $5 Million funding in 2007. These developments, along with the two new trough plants in the US and projects overseas, demonstrate that CSP is a viable and competitive technology.

1.3 PROBLEMS WITH SOLAR THERMAL POWER

Despite its many benefits, solar thermal power is still employed on a very limited basis in the US. The nine SEGS facilities are alone in the use of solar energy for large-scale domestic power production. In fact, solar-generated power accounted for less than 0.1% of the total US energy consumption in 2004 [D.O.E., 2005]. The technology is still relatively new, and there are disadvantages to solar thermal power that have delayed its growth in the US. Primarily, the efficiency of these plants is relatively low compared to that of traditional fossil fuel plants, and their equipment and maintenance costs are higher due to the complexity and vulnerability of the technology.

Many of the problems lie with the receiver tubes, which absorb the intensified solar radiation reflected from the parabolic mirrors. A typical receiver tube consists of a stainless steel absorber pipe which carries the heat transfer fluid, and a cylindrical glass envelope that is concentric to and surrounds the absorber pipe. The annular space between the two serves as a barrier to convective heat losses, and the absorber pipe is coated with a solar-selective material that maintains a high absorptance while minimizing the emittance of infrared radiation.

The first plant receivers were designed for the highest feasible level of efficiency but with little regard for cost effectiveness. The annular space of these receivers was kept at hard vacuum to maximize its insulating capabilities, and the absorber pipe was coated with a solar-selective material to maximize the absorption of the incident beam. Although these features improved efficiency, they have also proven to lead to serious maintenance problems and premature failures. For example, the glass envelopes can leak air into the annular space

so that the vacuum is lost, and increased pressure causes higher heat loss rates. When exposed to oxygen from such a leak, the solar-selective coating can break down and shed fine decomposition particles into the annulus, which can cloud the air or collect onto the inner face of the glass envelope. The cloudy glass resulting from the breakdown of the coating hinders the ability of the reflected light to reach the absorber, thus lowering efficiency. To minimize this problem, the metal bellows that supports the glass must be pierced and water circulated inside the receiver tube to wash out the cloudy precipitate. In more unexpected cases, hydrogen has permeated through the stainless steel pipe and leaked into the annulus. The high conductivity of the hydrogen creates such high heat transfer that these receivers are no longer functional and must either be punctured to release the hydrogen or be completely replaced.

Damage to the glass envelopes is likely the most common problem in the field. The glass envelopes are relatively fragile, and can break easily when exposed to severe weather conditions or when pieces of the reflecting mirrors break off and fall onto the receiver tubes. With a broken envelope, the absorber tube may be fully exposed to the ambient air, greatly increasing thermal losses. The replacement of these highly expensive and easily damaged components upon failure greatly increases the cost of operating and maintaining a SEGS solar field.

1.4 BASIS FOR CURRENT RESEARCH

Original solar collector field designs used the same high efficiency receivers at every location in the field. The collector field of a SEGS unit is universally organized into parallel loops of solar collectors. Heat transfer fluid returning from the energy conversion plant is heated to a moderately high temperature in the field. Typically fluid enters a collector loop around 270 °C and leaves at 380 °C. It is unlikely that the same high efficiency receiver tube is the best suited for operation over the entire range of temperatures experienced in a solar field. In particular, a receiver optimized for 380 °C operation may not be optimal at 270 °C.

This observation poses two important questions: 1) is an expensive, high efficiency, evacuated tube receiver the most cost effective for every location in a collector loop? and 2) can different receiver types be used at different locations in a collector loop to lower costs while maintaining the necessary performance level of the solar field? For example, a relatively inexpensive receiver with a flat black absorber and no vacuum may be more cost effective in the lower temperature segments of the loop. This study attempts to answer these questions and develop a solution for the optimal placement of receiver types in a collector loop to maximize the economic benefits of power production in solar thermal power plants.

The successful development of an optimal collector field model will help to lower costs of producing solar generated electricity. It will be applicable to future refurbishments and upgrades of the nine SEGS units, and also similar plants throughout the world, to make them more cost efficient. Significant decreases in prices could in turn make solar power more competitive with other forms of power generation. This would encourage further commercialization and research and development of solar thermal power technologies, and hopefully lead to the establishment of more solar plants in the US and around the world.

CHAPTER 2: BACKGROUND INFORMATION

2.1 FUNDAMENTALS OF SOLAR RADIATION

The energy emitted by the sun is known as extraterrestrial radiation, and it is a perpetual energy source. The amount of radiation emitted by the sun varies somewhat due to sun spots and other internal abnormalities. Solar radiation flux onto the Earth also varies at different times of the year due to the elliptical pattern of the Earth's orbit and consequential changes in distance from the sun. When comparing the two sources of irregularity, the fluctuations from the sun's internal and surface characteristics are significantly less influential than variations with time of year due to the Earth-sun distance. So, for the purposes of solar radiation calculations it is safe to assume that the intensity of emitted radiation from the sun is constant. This assumption led to the development of an important parameter, the Solar Constant. As defined by Duffie and Beckman, "the Solar Constant, G_{SC}, is the energy from the sun, per unit time, received on a unit of area of surface perpendicular to the direction of propagation of the radiation, at the Earth's mean distance from the sun, outside the atmosphere" [Duffie, 1980]. This constant has been experimentally measured many times, and its universally accepted value is 1353 W/m^2 [Thekaekara, 1971].

The solar radiation flux changes throughout the year because the distance from the Earth to the Sun varies. The solar radiation flux for a given day of the year is represented by the following equation [Duffie, 1980]:

$$G_{on} = G_{sc}\left(1 + 0.033\cos\frac{360n}{365}\right) \tag{2.1.1}$$

where G_{on} is the extraterrestrial radiation on a plane normal to the radiation, and n is the day of the year.

The above equation refers to extraterrestrial radiation measured just outside of the Earth's atmosphere. The amount of radiation that actually reaches the Earth's surface is

reduced through reflection, absorption, and scattering of light by gas molecules located in the atmosphere. The total radiation incident on a surface (at Earth's surface) is comprised of two forms. The first, beam radiation, is solar radiation on a surface that has passed through the atmosphere without being appreciably scattered. The second, diffuse radiation, is that which reaches the surface after being significantly scattered by the atmosphere. The typical measurement of radiation is irradiance, G, which is the amount of radiation per unit time on a surface, per unit area of the surface (W/m^2). Beam irradiance can be given with respect to a surface on any tilted plane, G_{BT}, or it can also be represented by the radiation flux incident normal, or perpendicular, to a surface, G_{BN}.

2.2 SOLAR TIME AND SOLAR ANGLES

Solar position geometry and the processing of solar radiation data are well established techniques. Nevertheless, for completeness and to provide a ready reference for subsequent users of the plant performance models, an overview of the solar position and solar radiation processing is given herein. The performance of any solar absorbing surface is affected by the direction of the incoming beam radiation, or more specifically, the angle at which the incident beam radiation hits the surface. This incidence angle, represented by θ, is based on the position of the sun with respect to the location and orientation of the surface under consideration. It is most effectively defined by its cosine, which is the dot product of the unit normal vector of the surface, $\hat{n}$, and the unit vector from the surface to the sun, $\hat{s}$ [Jeter, 1979].

$$\cos\theta = \hat{n}\cdot\hat{s} = \hat{n}_{\mathbf{x}}\hat{s}_{\mathbf{x}} + \hat{n}_{\mathbf{y}}\hat{s}_{\mathbf{y}} + \hat{n}_{\mathbf{z}}\hat{s}_{\mathbf{z}} \tag{2.2.1}$$

The convention used in this thesis is a right-hand coordinate system where the positive x-direction is West, the positive y-direction is South, and the z-direction is vertical and positive toward the zenith. The unit normal vectors can be defined by several angles that describe the

overall geometry of the system. The factors controlling this geometric relationship are the coordinate location of the surface, the angle of the surface with respect to the horizontal plane, the orientation of the surface with respect to the sun, the angular rotation of the Earth on its axis, and the position of the Earth in its orbital path.

All time values used in the calculations of solar angles are represented by solar time. This parameter is an adjustment to standard time that coincides with the movement of the sun across the sky, such that solar noon occurs when the sun is directly above the local meridian. The standard equation for solar time is as follows:

$$\text{solar time} = \text{standard time} + 4\min\left(L_{ST} - L_{LOC}\right) + EOT \tag{2.2.2}$$

The standard time is that of the local time zone, and the standard meridian of the local time zone is represented by L_{ST}. L_{LOC} is the longitude of the exact location under consideration. The difference $\left(L_{ST} - L_{LOC}\right)$ is multiplied by 4, the time (in minutes) required for the sun to move one radial degree across the sky. EOT represents the Equation of Time, which has units of minutes. This number accounts for disturbances to the Earth's rate of rotation, and can be calculated in minutes with the following approximate equation, attributed to Whillier and as quoted by Duffie and Beckman [1980]:

$$EOT = 9.87\sin(2B) - 7.53\cos B - 1.5\sin B \tag{2.2.3}$$

$$B = \frac{360(n-81)}{364}$$

Several angles are needed to determine the direction of incident beam radiation on a surface of given orientation with respect to the horizontal plane. The geometric significance of each of these angles is summarized in Table 2.2.1. The latitude is fixed for any given location and can be quickly determined from a basic geographical reference. The declination accounts for the changing orientation of the Earth with respect to the sun due to the Earth's orbit. Since the Earth's axis is tilted, the angle between the sun and the equator will be different at different times of the year. Figure 2.2.2 shows a basic illustration of this concept.

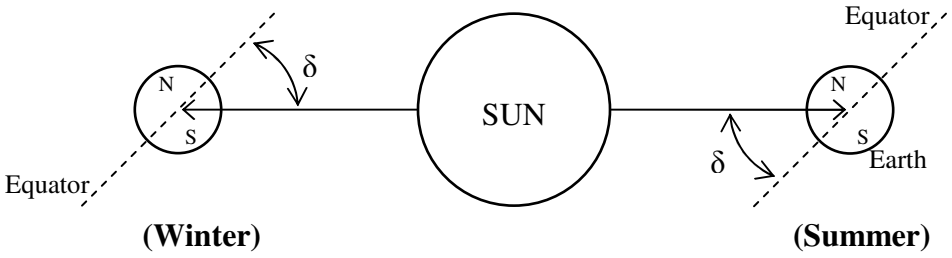

Figure 2.2.2: Variation in Declination due to Earth's Orbit

Table 2.2.1: Solar Angles as Presented by Duffie and Beckman [Duffie, 1980]

Solar Angle	Symbol	Range	Description
Latitude	ϕ	$-90^o \le \phi \le 90^o$	Angular location North/South of Equator (North positive)
Declination	δ	$-23.45^o \le \delta \le 23.45^o$	Angular position of the sun at solar noon with respect to the plane of the equator (North positive)
Slope	β	$0^o \le \beta \le 180^o$	Angle between plane of surface and the horizontal plane
Surface Azimuth Angle	γ	$-180^o \le \gamma \le 180^o$	Deviation of the projection on a horizontal plane of the normal to the surface from the local meridian, with zero due South (East negative, West positive)
Solar Azimuth Angle	γ_s	$-180^o \le \gamma_s \le 180^o$	Deviation of the projection on a horizontal plane of the line of sight to the sun from the local meridian, with zero due South (East negative, West positive)
Hour Angle	ω	$-180^o \le \omega \le 180^o$	Angular displacement of the sun East or West of the local meridian due to the rotation of the Earth on its axis (before solar noon= negative, after solar noon = positive)
Incident Angle	θ	$0^o \le \theta \le 90^o$	Angle between beam radiation on a surface and the normal to that surface
Zenith Angle	θ_z	$0^o \le \theta_z \le 90^o$	Angle subtended by a vertical line to the zenith (point directly overhead) and the line of sight to the sun

The declination can be determined for a given day of the year, n, using the following equation.

$$\delta = 23.45 \sin\left(360 \frac{284 + n}{365} \right) \tag{2.2.4}$$

The hour angle, ω, is calculated by multiplying the angular velocity of the Earth's rotation by the change in solar time with respect to solar noon. Given that the Earth rotates 15º per hour on its axis, the hour angle can be quickly determined by the following equation:

$$\omega = \left(15 \frac{\text{deg}}{\text{hr}} \right) (\text{ solar time} - 12) \tag{2.2.5}$$

The general equation for the cosine of the incidence angle of beam radiation on a surface incorporates all of the aforementioned solar angles [Duffie, 1980].

$$\begin{aligned} \cos\theta = {} & \sin\delta \sin\phi \cos\beta - \sin\delta \cos\phi \sin\beta \cos \\ & + \cos\delta \cos\phi \cos\beta \cos\omega \\ & + \cos\delta \sin\phi \sin\beta \cos\gamma \cos\omega \\ & + \cos\delta \sin\beta \sin\gamma \sin\omega \end{aligned} \tag{2.2.6}$$

For a horizontal surface the slope, β, is zero and the incidence angle will be equivalent to the zenith angle, as the surface will be perpendicular to the zenith vector. Thus the zenith angle can be determined by evaluating a simplified form of Equation 2.2.5 with β=0.

$$\cos\theta_z = \cos\delta \cos\phi \cos\omega + \sin\delta \sin\phi \tag{2.2.7}$$

The complimentary angle of θ_z is called the solar elevation, or solar altitude and is denoted by the symbol α. This is the angle between the line of sight from the sun to the surface and the horizontal plane. The solar altitude and solar azimuth angles are useful

parameters in determining solar geometries, as they eliminate the need of solar time in subsequent calculations. This simplifies the mathematical process and the programming complexity of determining solar angles. Since they are complementary angles the sine of the solar altitude is equal to the cosine of the zenith angle. The sine and cosine of the solar azimuth angle can then be written as a function of solar altitude and other known angles. These equations are as follows. For an example see Jeter [1979].

$$\sin \gamma_s = \frac{\cos \delta \sin \omega}{\cos \alpha} \tag{2.2.8}$$

$$\cos \gamma_s = \frac{\sin \phi \cos \delta \cos \omega - \sin \delta \cos \phi}{\cos \alpha} \tag{2.2.9}$$

Since the azimuth angle ranges from -180º to 180º it can be located in any of the four quadrants. Because of this, it is necessary to define both its sine and cosine to avoid misrepresenting the orientation.

With all of the solar angles determined, there is only one more factor to account for. That is the orientation of the collecting surface with respect to the sun due to solar tracking. For a stationary surface, there is no further calculation necessary; the incidence angle can be defined solely by the solar angle relationships. However, if the collecting surface employs a solar tracking system, then further calculations must be performed to adjust for this tracking movement.

2.3 TRACKING ANGLES

Parabolic trough concentrators are designed to move or rotate so that they can follow the path of the sun and increase the amount of radiation into the collector. Tracking angles are a unique issue with respect to trough concentrators, so the equations governing tracking may not be covered in the usual textbooks. Tracking angles and incident angles are a simple concept, but are critical in the analysis of trough collectors. Therefore, the equations are

reviewed and calculations are verified here. The tracking movement can be one or two-dimensional depending on the type of concentrator being employed. For example, linear concentrators typically have one-dimensional tracking systems which allow the collectors to rotate about a single axis oriented either East-to-West or North-to-South. Point concentrators, which focus incident light onto a single central point, use two-dimensional tracking where the collector can rotate about two axes.

The scope of this project concerns only one-dimensional tracking for linear concentrators, so only equations for this form of solar tracking will be presented here. A general equation for the tracking angle, τ, for a linear concentrating collector that is horizontal ($\beta = 0$) with no particular orientation of the focal line (this concept will be discussed in further detail in the section concerning parabolic trough collectors) was developed by Jeter [1979].

$$\tan\tau = \frac{\tan\alpha}{\cos(\gamma_s - \gamma)} \tag{2.3.1}$$

where, as aforementioned, γ and γ_s are the surface and solar azimuth angles, respectively. In the common cases where the surface azimuth of the collector string corresponds to an east-west or north-south orientation, Equation 2.2.9 can be simplified. For an East-West orientation, γ=0 and the resulting equation is,

$$\tan\tau = \frac{\tan\alpha}{\cos\gamma_s} \tag{2.3.2a}$$

For a North-South collector orientation, the surface azimuth is equal to π/2 and the resultant simplified equation for tracking angle is as follows:

$$\tan\tau = \frac{\tan\alpha}{\sin\gamma_s} \tag{2.3.2b}$$

The natural initial side of the tracking angle is due West; however, for the collector orientations of this project it is desirable to consider the initial side being due East. This way, the tracking angle is initially at 0 ° at the beginning of the day and increases to 180 ° at the day's end. A more general method of determining the tracking angle for a collector that may be tilted, $\beta \neq 0$, was also developed by Jeter [1979]. This case requires the solar azimuth and solar altitude angles to be determined based on a rotated coordinate system and introduces trigonometric functions of β into the angle equations, making the tracking angle calculations more complex. This more general approach was not necessary for the scope of this project, as the solar fields analyzed are oriented horizontally, and the slope angle is assumed to be zero in all cases and models observed.

With the additional knowledge of the tracking angles, the appropriate unit vectors specified in Equation 2.2.1 can be defined, and the cosine of the incidence angle can be calculated. By considering the initial tracking angle side to be due East, the original right hand coordinate system is no longer appropriate for defining the unit vectors. Instead, the vectors must be defined with positive x-direction to the South, positive y-direction to the West, and positive z-direction still to the zenith. For the described geometries and angular relationships, the unit vectors an incident angle cosine based on linear collectors are defined as follows:

$$\hat{s} = (\cos\alpha\cos\gamma_s,\ \cos\alpha\sin\gamma_s,\ \sin\alpha)$$

For East-West Orientation:

$$\hat{n} = (\cos\tau,\ 0,\ \sin\tau)$$

$$\cos\theta = \cos\tau\cos\alpha\cos\gamma_s + \sin\tau\sin\alpha \qquad (2.3.3a)$$

For North-South orientation:

$$\hat{n} = (0,\ \cos\tau,\ \sin\tau)$$

$$\cos\theta = \cos\tau\cos\alpha\sin\gamma_s + \sin\tau\sin\alpha \qquad (2.3.3b)$$

The more general equations accounting for tilted collectors were developed by Jeter, but are not included here as the scope of this project does not necessitate the consideration of tilted

collectors. The SEGS unit observed and modeled in this study employs a North-South collector orientation. Thus, the simplified relationships in Equations 2.2.5b and 2.3.3b are used in all solar angle calculations. Figure 2.3.1 shows the variation in incidence angle over the course of one year in southern California, at the location of the SEGS facilities. The values of incidence angle were calculated at solar noon of each day of the year using Equations 2.2.1 through 2.3.3. For a N-S collector orientation, the incident angle is equal to the zenith angle, which is the latitude minus the declination, at solar noon.

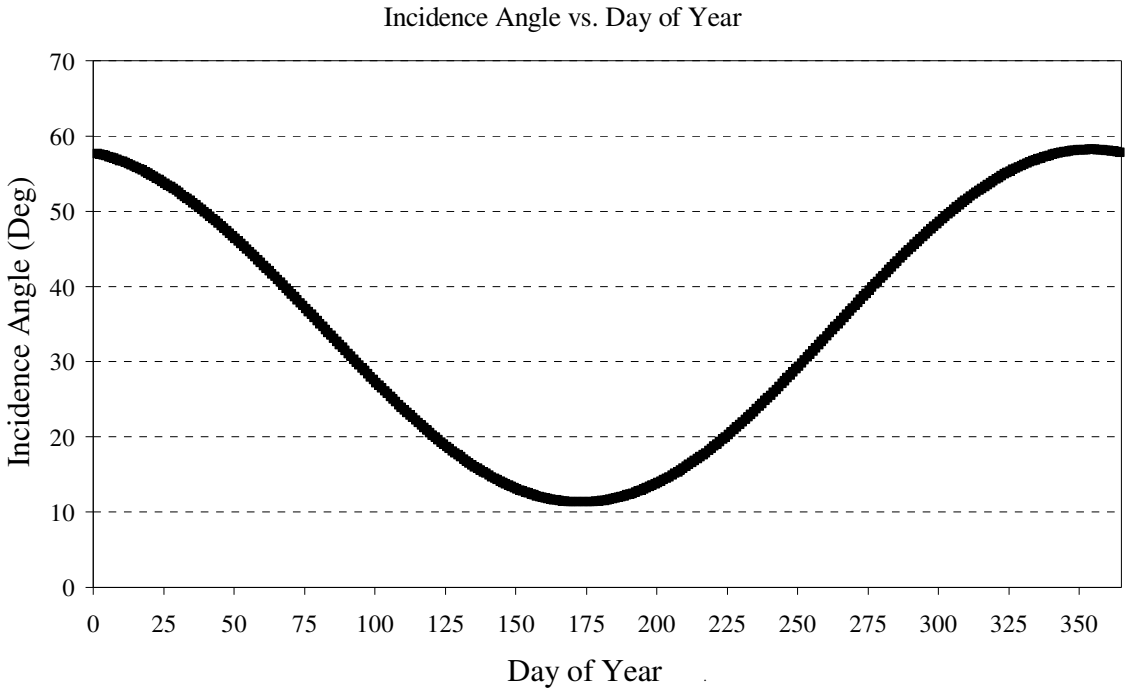

Figure 2.3.1 Variation of Incidence Angle at Solar Noon Over One Year Period

As the chart illustrates, incidence angles are highest in the winter months when the Sun is above the southern hemisphere. In summer months, the Sun passes above the northern hemisphere, so incidence angles in California are lowest at this time. The calculation results in Figure 2.3.1 thus prove the validity of the solar angle equations, as their results agree with fundamental observations of the Sun's location and path with respect to the Earth.

Figure 2.3.2 shows hourly values of incidence angle and tracking angle for an arbitrary day of the year. For convenience, the tracking angle, in degrees, is defined with its

initial side due East. Tracking angle calculations appear to be accurate, as they produce values near 0° in the morning when the Sun is due East, and values near 180° at the end of the day when the Sun is due West. The calculations also show the variation in incidence angle over the course of one day, with the highest angles occurring during the middle of the day.

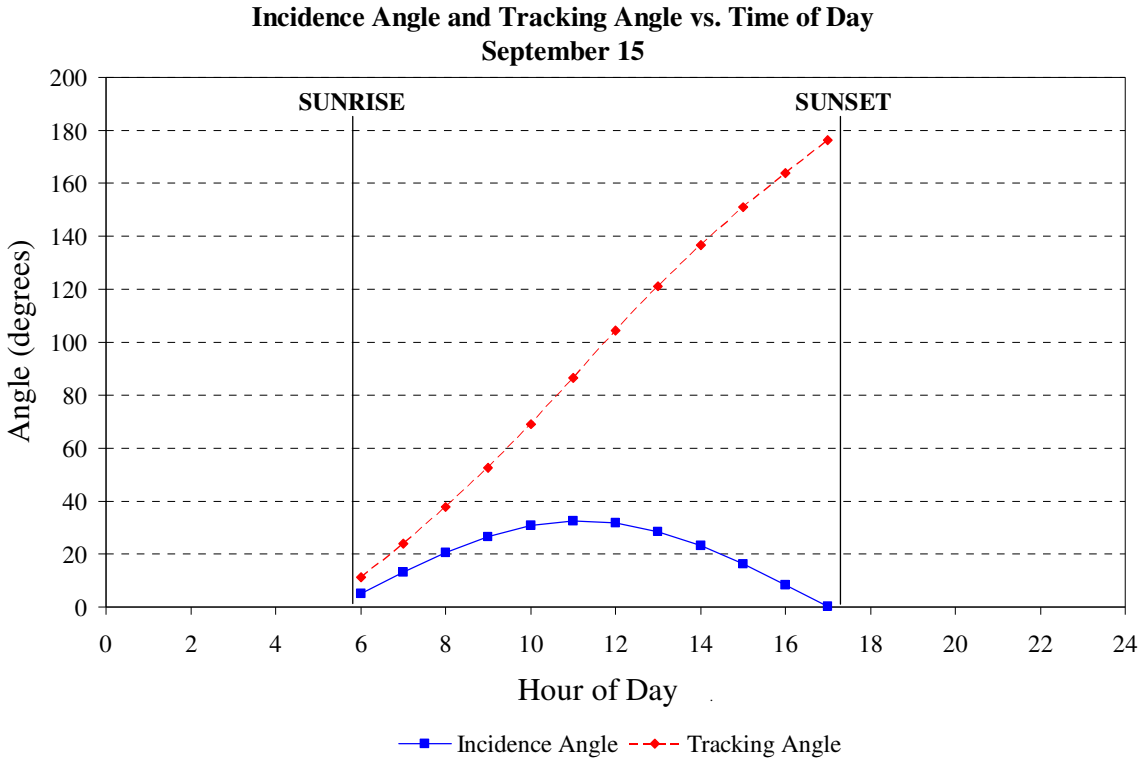

Figure 2.3.2: Example of Hourly Incidence Angle and Tracking Angle Calculations

The magnitude of the incidence angle affects the optical performance of solar collectors in several ways. For example, at large angles of incidence more light is reflected from surfaces receiving solar radiation allowing less energy to be absorbed. The reflected image of solar light is expanded at higher incidence angles. Also, a high incidence angle results in increased reflected beam path length from concentrating mirrors and a large concentrated image at the receiver, which in some cases can cause reflected light to miss the

receiving surface. These sources of optical losses will be discussed more thoroughly in the next section, concerning parabolic trough solar collectors.

2.4 PARABOLIC TROUGH SOLAR COLLECTORS

Linear imaging concentrators, also known as cylindrical concentrators, use mirrors or specularly reflecting surfaces to reflect incident beam radiation and focus it onto a line. The focal line, onto which the beam radiation is reflected, is comprised of all focal points at each cross-sectional location of the concentrator. These concentrators can come in various shapes, but always have a constant cross-sectional geometry.

Parabolic trough solar collectors employ linear imaging concentration. These collectors are comprised of a cylindrical concentrator, of parabolic cross-sectional shape, and a circular cylindrical receiver located along the focal line of the parabola. The projection of the reflecting surface parallel to the collector plane is known as the collector aperture. Figure 2.4.1 shows a cross-sectional view of a parabolic trough collector assembly. The radius of the parabola at an arbitrary location is denoted by r, and is called the "mirror radius". The maximum mirror radius occurs at its outer rim, and is fittingly called the "rim radius", r_r. The angle between the reflected beam radiation and the central plane (defined by Duffie and Beckman as the line connecting the axis and focal point of the parabola [Duffie, 1980]) is represented by φ. The "rim angle", φ_r, corresponds to beam radiation reflected from the outer rim of the concentrator.

The size of a reflected solar image at the focal point is dependent upon the mirror radius at the point of incidence of the beam radiation. The farther away from the vertex the beam radiation hits the more diffused the image will be. A simple equation for the image width, W_{im}, was developed by Jeter [1979].

$$W_{im} = L_{path}\theta_s \tag{2.4.1}$$

where θ_s represents the angular width of the incident beam radiation, and L_{path} is the reflected path length of the incident beam radiation. For near normal incidence, the value of the beam angle is virtually fixed at 0.53º ($\approx$ 0.00925 rad), and the reflected beam path length is equal to the parabolic radius. So, for near normal incidence, occurring more frequently in the summer months, Equation 2.4.1 can be rewritten as $W_{\text{im}} = 0.00925r$.

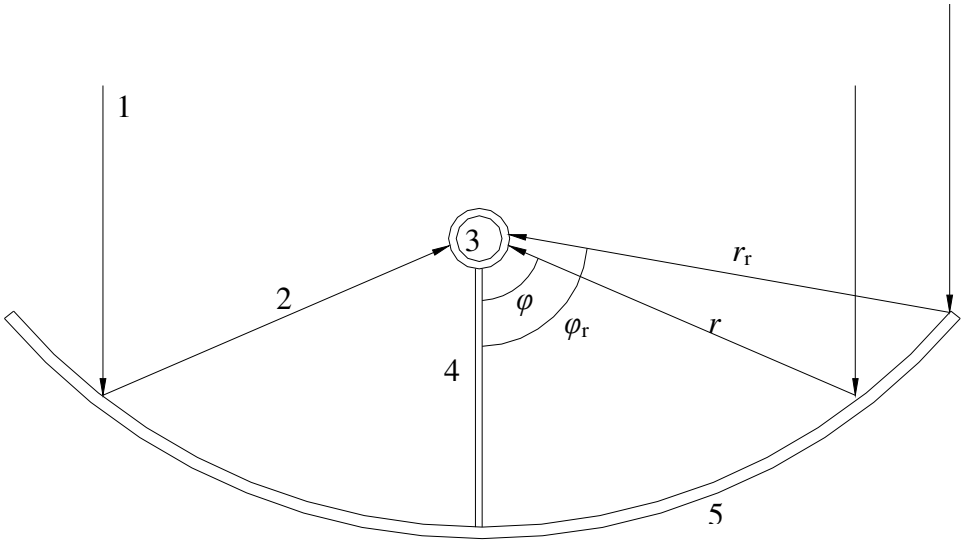

1. Incident Beam Radiation 2. Reflected Beam Radiation 3. Receiver Tube	4. Receiver Tube Support Bracket 5. Parabolic Trough Reflector

Figure 2.4.1: Cross-Sectional View of Parabolic Trough Solar Collector (Not to Scale)

The mirror radius at an arbitrary point on the parabola can be calculated from the following equation [Duffie, 1980],

$$r = \frac{2f}{1+\cos\varphi} \tag{2.4.2}$$

The geometric characteristics of any parabola defined in the x-y plane create a relationship between x and y where the focal length, f, is constant. Thus, the focal length of any parabolic trough collector can be derived given an equation for its shape.

$$y = \frac{x^2}{4f} \text{ OR } f = \frac{x^2}{4y} \tag{2.4.3}$$

Equations 2.4.1 to 2.4.3 present a useful mathematical relationship between solar image size and the geometry of the parabolic reflector. For optimal performance, the receiver should be large enough to intercept all of the reflected light from the concentrating surface during near normal operation, so it must be at least as wide as the most dispersed solar image, which is reflected from the rim of the collector as explained above. Thus, the diameter of a cylindrical receiver should be at least as large as the image width from rim angle reflection.

$$D_{\text{rec}} \geq W_{\text{im,max}} = r_{\text{r}}\theta_{\text{s}} = \frac{2f}{1+\cos\varphi_{\text{r}}}\theta_{\text{s}} = \frac{2x^2}{4y\left(1+\cos\varphi_{\text{r}}\right)}\theta_{\text{s}} \tag{2.4.4}$$

These relationships must be considered in the design of any parabolic trough collector to ensure that the shape of the parabola and size of the receiver will work together to yield optimum radiation collection. To evaluate a collector's effectiveness in concentrating incident beam radiation, a parameter called the concentration ratio must be introduced.

The concentration ratio, C, is a measure of the multiplicative capability of the concentrating aperture with regards to the solar radiation flux density. More simply, it

measures the flux density, or intensity, of radiation on the receiver for a given flux density intercepted by the aperture.

$$C = \frac{\text{flux density at receiver}}{\text{flux density at aperture}} \tag{2.4.5}$$

The aperture intercepts a specific amount of beam radiation energy over its area and redirects the same amount of total energy onto a much smaller area. Thus, it is intuitive that the concentration ratio will be much greater than 1 for a properly designed collector. The concentration ratio for parabolic reflectors is typically represented by a simpler, more easily calculated geometric ratio of aperture area to receiver area.

$$C_g = \frac{\text{Aperture Area}}{\text{Receiver Area}} \tag{2.4.6}$$

The geometric ratio is only an approximation of the true concentration ratio, as it does not account for losses from the reflector, such as mirror absorption, defective mirrors, or reflected radiation that misses the receiver. Also, the geometric ratio assumes uniform reflectance at all locations of the aperture, which is not the case on practical applications. However, these losses are generally negligible compared to receiver optical and thermal losses, particularly in large scale collector fields where reflected solar flux density is high, so the geometric approximation of the concentration ratio, C_g, is sufficient. It is entirely accurate in terms of the geometric design of the collector apparatus.

2.5 COLLECTOR PERFORMANCE

The general method of determining the performance of a parabolic trough collector is to compare the rate of useful heat energy absorption by the receiver, $\dot{Q}_u$, to the amount of

solar radiation incident on the collector aperture. The collector efficiency is the ratio of absorbed energy to incident beam irradiance and will be from this point forward represented by η_{coll}. The basic relationship is presented here.

$$\eta_{\text{COLL}} = \frac{\dot{Q}_{\text{u}}}{G_{\text{BT}} A_{\text{ap}}} \tag{2.5.1}$$

Here, G_{BT} is the solar beam irradiance on the tilted, aperture plane, and A_{ap} is the aperture area. Useful heat collection by the receiver is reduced by two main factors, optical losses and thermal losses.

Optical losses represent the amount of incident radiation that either does not reach or is not absorbed by the receiver. These losses are caused by imperfections in both the concentrator and receiver surfaces, as well as by incidence angle effects. In the ideal case, 100% of the beam radiation hitting the concentrator would be reflected onto the receiver, and 100% of this reflected energy would then be absorbed by the receiver; however, in practical applications, the materials employed by these collector systems are not ideal. A small percentage of radiation is either absorbed or scattered by the reflecting surface and does not get reflected. Similarly, the receiver surface is not perfectly absorptive, so a small amount of incident light will reflect off of this surface and be lost to the atmosphere. Typical cylindrical receivers are comprised of an absorber tube with a protective transparent covering that allows incident light to transmit through to the absorber while protecting it from damage via environmental effects. This glass covering further adds to optical losses, as some incident light is absorbed by or reflected from it and does not pass through to the absorber. Also, transmitted light may be refracted at an angle such that it can bypass the absorber and exit through the other side of the covering.

The transmitting, absorbing, and reflecting capacities of all surfaces are interdependent and related by a simple equation.

$$\tau + \alpha + \rho = 1 \tag{2.5.2}$$

where τ is the material transmittance, α is the absorptance, and ρ is the reflectance. The overall effectiveness of the collector assembly, as a unit, to gather incident solar radiation is defined by the optical efficiency, η_o. The optical efficiency defines the percent of radiation intercepted by the aperture that is ultimately absorbed by the receiver. It is a function of the reflectance of the concentrating mirrors, the transmittance and refractive index of the receiver covering, the absorptance of the receiver surface, and the incidence angle, θ.

$$\eta_o = \eta_o(\tau_{cover}, n_{cover}, \alpha_{rec}, \rho_{mirror}, \theta, \text{other variables})$$

The effect of incidence angle on the optical efficiency is represented in part by an incidence angle modifier, IAM, which is a function of θ. Off-normal incidence angles also cause optical losses at the ends of collector strings, because a small portion of the incident radiation does not hit the concentrating mirror. These "end-effects" are typically insignificant for long collector strings like those dealt with in this project; however, for shorter strings, or at extreme incidence angles, the losses may not be negligible. End-effects can be represented by a ratio of aperture area reflecting radiation to total aperture area [Jeter, 1979].

$$X_{END} = \frac{A_{ap} - A_L}{A_{ap}} \tag{2.5.3a}$$

For the solar field arrangement at SEGS this ratio can be approximated by the following expression derived from analysis of the geometry of the collector and SCA string.

$$X_{END} = 1 - \tan\theta \frac{f}{L_{STRING}} \tag{2.5.3b}$$

Here, f is the collector focal length and L_{STRING} is the length of the collector string. Other, more ambiguous variables also contribute to the optical efficiency of a given collector, so it is difficult to implicitly define this important parameter. Past studies have relied on

experimentation to determine an empirical value for the optical efficiency of a given type of collector.

Thermal losses occur when energy that has already been absorbed by the receiver is released to the environment. These losses occur by way of heat transfer out of the receiver due to a temperature difference between the receiver and ambient air. The amount of heat transfer losses can vary depending on the components, geometry, and thermodynamic conditions of the receiver. Typically, heat is lost to the environment by three modes, convection between the outer receiver surface and ambient air, radiation from the outer receiver surface to the sky, and conduction through the support structures of the receiver. The latter is relatively small compared to the convection and radiation losses; on average, it is estimated to account for only about 1% of the total system heat loss [Forristal, 2003]. The bracket conduction is also difficult to quantify based on the complex geometry of the supports. Therefore, it is typically considered negligible in heat loss calculations. The receiver heat loss is hence controlled by the radiation and convection from the outer surface to the ambient.

Based on the thermal circuit analogy for heat transfer, the total heat loss, $\dot{Q}_{\mathrm{L}}$, from the receiver to the ambient can be represented by a temperature change and an effective system resistance, as shown in Equation 2.5.4.

$$\dot{Q}_{\mathrm{L}} = \frac{\left(T_{\mathrm{R}} - T_{\mathrm{amb}}\right)}{R_{\mathrm{sys}}} \tag{2.5.4}$$

where T_{R} is the receiver temperature, T_{amb} is the ambient temperature, and R_{sys} is the thermal resistance between the receiver surface and ambient. The system resistance depends on several factors including the material properties of the receiver and covering, ambient conditions including temperature and wind speed, and the state of gas between the receiver and cover. Because these conditions vary between collector types and geographical locations, a universal expression for resistance is not feasible; specific evaluation of the receiver assembly under consideration is necessary to determine its heat loss characteristics. The schematic in Figure 2.5.1 illustrates the general resistances to modes of heat loss within the

receiver tubes employed at SEGS. The corresponding thermal network is shown in Figure 2.5.2.

The useful heat collection by the receiver can be written in terms of optical and thermal losses, where optical losses are represented by the optical efficiency, η_o and thermal losses are represented by $\dot{Q}_L$.

$$\dot{Q}_u = \eta_o G_{BT} A_{ap} - \dot{Q}_L \tag{2.5.5}$$

The optical efficiency is multiplied by the tilted beam radiation on the aperture, so as to represent a reduction in the incident radiation that reaches the receiver. Receiver thermal losses must be subtracted independently since they represent absorbed energy by the receiver that was later lost. Substituting Equation 2.5.5 into Equation 2.5.1 yields a new expression for collector efficiency.

$$\eta_{COLL} = \eta_o - \frac{\dot{Q}_L}{G_{BT} A_{ap}} \tag{2.5.6}$$

This form is more practical, as it allows for optical and thermal effects to be considered separately.

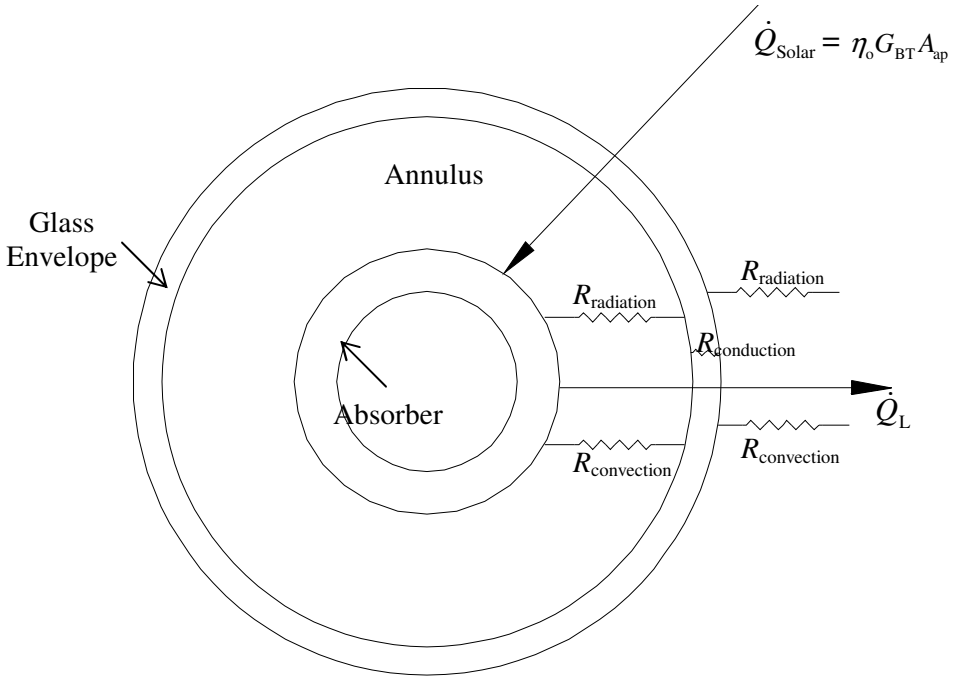

Figure 2.5.1: Cross-Sectional Schematic of Receiver Tube with Thermal Resistances and Heat Flows (Not to Scale)

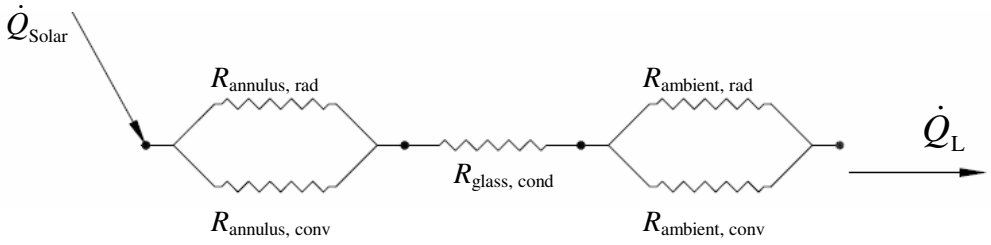

Figure 2.5.2: Thermal Network Corresponding to Figure 2.5.1 Schematic

2.6 SOLAR ELECTRIC GENERATING SYSTEMS (SEGS)

Solar Electric Generating Systems, denoted by the acronym SEGS, are the primary source of solar thermal electric power production in the United States. There are currently nine SEGS units operating in the US, and all are located in the Mojave Desert of southern California. All units were built and originally owned and operated by Luz International, and have since been sold to other utility companies. The first station built, SEGS I, was made operational in 1985 and had an output capacity of about 14 MW. Over the next six years Luz built eight more SEGS units, one in Dagget, CA where SEGS one is located, and the rest at nearby Kramer Junction in Barstow. As the technology improved, the newer units had increasingly higher efficiencies and employed larger solar collection fields. The two latest units built, SEGS VIII and IX, were put into operation in 1989 and 1990, respectively, and designed for an output capacity of 80 MW. Through various improvements since their original construction, the SEGS performance data used in this project shows that the peak capacity of these units has increased to about 90 MW.

The SEGS stations employ parabolic trough collectors, similar to those previously described, to collect solar energy which is then converted to electric power. In order to collect the large amounts of heat necessary to drive steam generation in the turbine cycle, SEGS units have large solar fields filled with hundreds of parabolic collectors. Figure 2.6.1 shows the layout of a typical SEGS unit, which consists of two main fluid flow loops; the hot oil (or heat transfer fluid) loop and the solar steam loop. Heat transfer fluid (HTF) is heated as it flows through the solar field. After exiting the field the high temperature HTF is sent through several heat exchangers, interacting with the water in the solar steam loop and creating the steam necessary to power the turbine generator.

The original receiver tubes used in these fields were developed by Luz and are called Heat Collection Elements (HCE) [Dudley, 1993]. In these HCEs, the vacuum between absorber and glass envelope is maintained by a welded glass-to-metal seal at the bellows, at both ends of the tube. Figure 2.6.2 shows the basic schematics of a typical HCE. Recently, a new receiver tube was developed with improved heat collection capabilities, called the Universal Vacuum Collector (UVAC). The UVACs have been installed at some locations in the SEGS units.

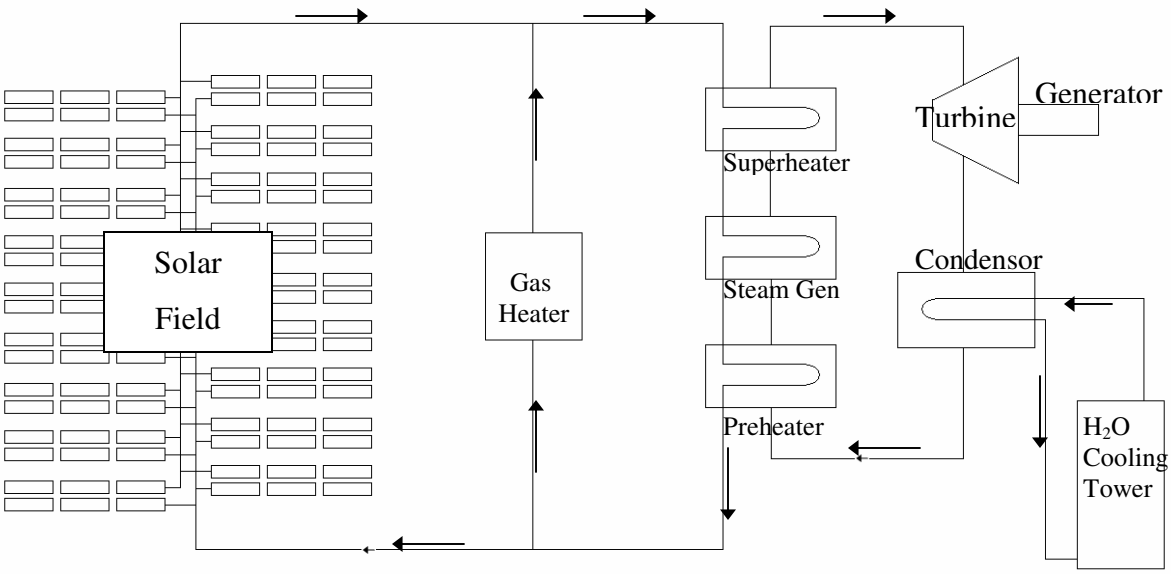

Figure 2.6.1: Basic Layout of Typical SEGS Plant

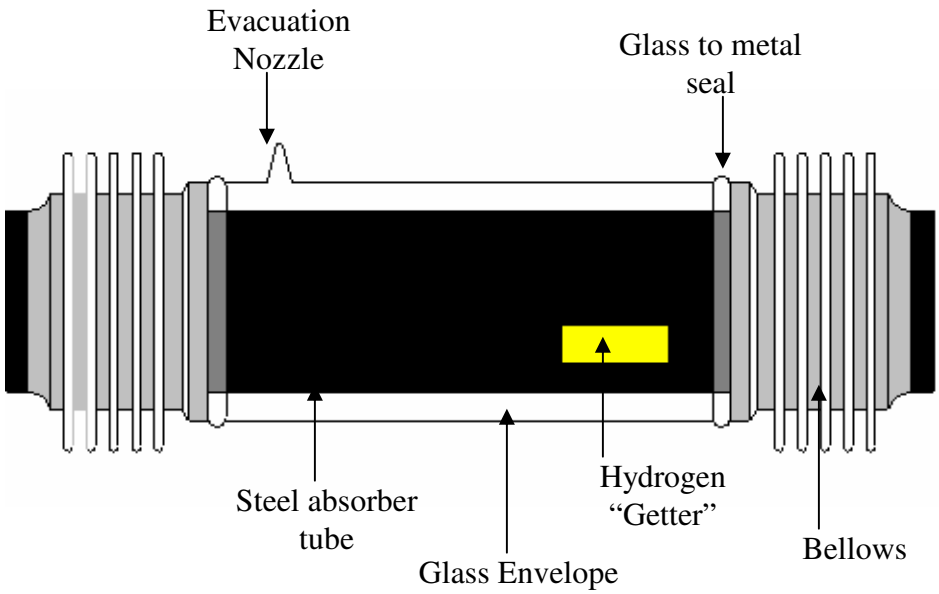

Figure 2.6.2: Schematic of a Typical Heat Collection Element

The stainless steel absorber tubes are typically coated with the aforementioned "solar selective" material, but in some cases highly absorptive, but non-selective, black enamel has also been used effectively. The original HCE developed by Luz used a flat black enamel coating, but as new SEGS units required higher solar field outlet temperatures Luz developed a second generation HCE, the LS-2 receiver, to meet these needs. The first LS-2 receivers employed a black chrome solar selective coating, and later the black chrome was replaced by a more effective cermet material. The UVACs have a coating similar to the Luz cermet, but with slightly improved solar absorption capabilities.

The chemical sponges, or "getters", shown in the figure are used to detect and absorb hydrogen that may leak into the evacuated annulus. In some cases, particularly at high operating temperatures, hydrogen can diffuse through the stainless steel absorber pipe into the annulus, causing unwanted convective heat loss. The getters are employed to minimize these effects. A single HCE stretches approximately 4m in length and has a total diameter of about 5.7 cm.

The collector units, HCE with parabolic trough reflector, are grouped in series to form Solar Collector Assemblies (SCA), the basic cell unit of a solar field. SCAs are organized in the field into loops that receive cooled heat transfer fluid from the steam generator at the inlet end and deliver high temperature heat transfer fluid to the steam superheater at the outlet. One loop contains six SCAs in series. Figure 2.6.3 shows a crude representation of a typical SCA loop with hot and cold headers that run to and from the steam turbine power block, located at the center of the solar field. The number of loops and size of individual SCAs differs between the nine SEGS units, and the output capacity of each is roughly proportional to the total aperture area of the solar field. Table 2.6.1 lists the solar field aperture area, net output capacity, and annual production for each of the SEGS units [Dudley et al, 1993].

Table 2.6.1: Solar Field Area/Output Comparison of Nine SEGS Units

Unit	I	II	III	IV	V	VI	VII	VIII	IX
Solar Field Aperture Area (hectares)	8.3	19.0	23.0	23.0	25.1	18.8	19.4	46.4	48.4
Rated Capacity, MWe	13.8	30	30	30	30	30	30	80	80
Annual Net Electricity Production (GW-hr)	30.1	80.5	91.3	91.3	99.2	90.9	92.6	252.8	256.1

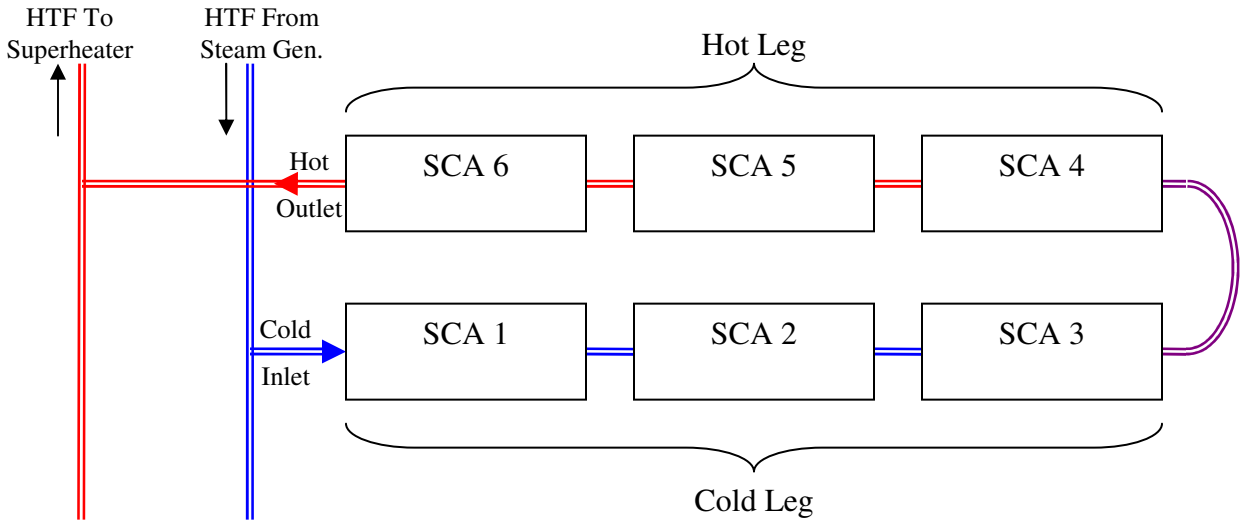

Figure 2.6.3: Basic Schematic of SCA Loop in SEGS Collector Field

2.7 PREVIOUS STUDY OF COLLECTOR PERFORMANCE

In 1993, Sandia National Laboratories (SNL) performed experiments on their rotating platform parabolic trough collector test unit to measure the optical properties and thermal behavior of a typical collector in the field. The test apparatus was modeled after the SEGS parabolic troughs, and was the length of a single HCE. Twelve LS-2 HCEs, four cermet-coated (a composite of ceramic and metallic materials) and eight black chrome-coated, were individually tested in the apparatus. They included receivers whose annulus vacuum had been compromised and ones that still had vacuum. Separate experiments were conducted to measure the optical efficiency at normal incidence, the effect of incidence angle on optical efficiency (Incident Angle Modifier), and the thermal losses from the receiver during operation. The HTF used in the testing was Syltherm 800 [Dow, 2001], whose fluid properties are nearly equal to those of Therminol-VP1 [Solutia, 1999]. The published results of these experiments are reproduced in Figure 2.7.1.

The incident angle modifier, IAM, is a coefficient that accounts for the affect of off-normal incident beam radiation on the optical efficiency of the collector. For example, at high incident angles, the optical efficiency decreases, while at near normal incidence the optical efficient is maximized. The IAM varies with incident angle to accurately reflect this change in optical efficiency. Figure 2.7.1b shows the difference in receiver thermal losses between the case of an irradiated absorber and the case of an absorber that is not irradiated. When irradiated, the absorber surface temperature is elevated, causing an increase in thermal losses. The peak optical efficiency corresponds to the case of normal incidence where the change in temperature between the HTF and ambient is zero. Based on Figure 2.7.1c, the peak optical efficiency is 73.3%, as presented by SNL [Dudley et al, 1993]. These test results are used in this project as a benchmark for modeling the efficiency of different collector types.

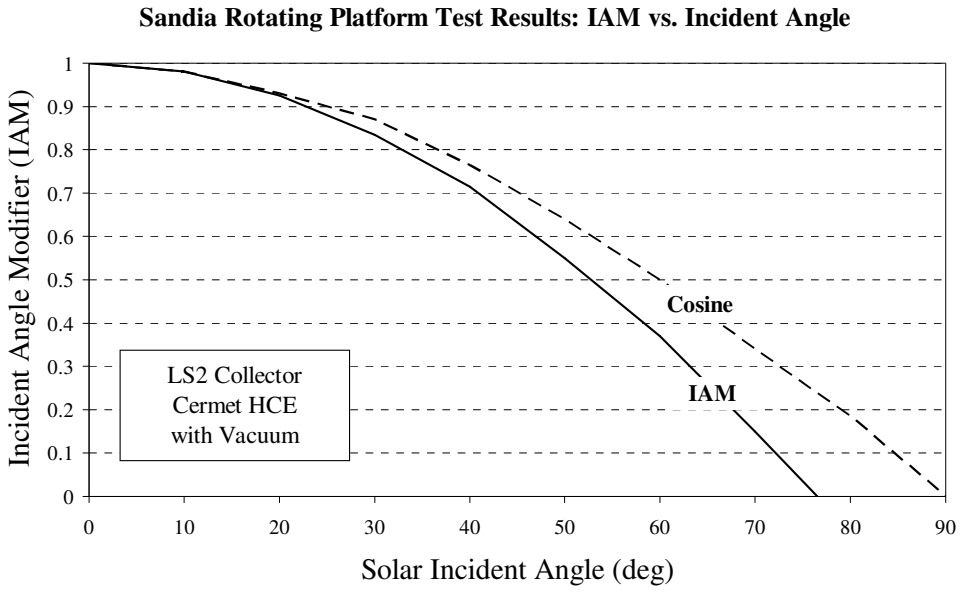

Figure 2.7.1a: IAM Results from Sandia Rotating Platform Collector Tests [Dudley et al, 1993]

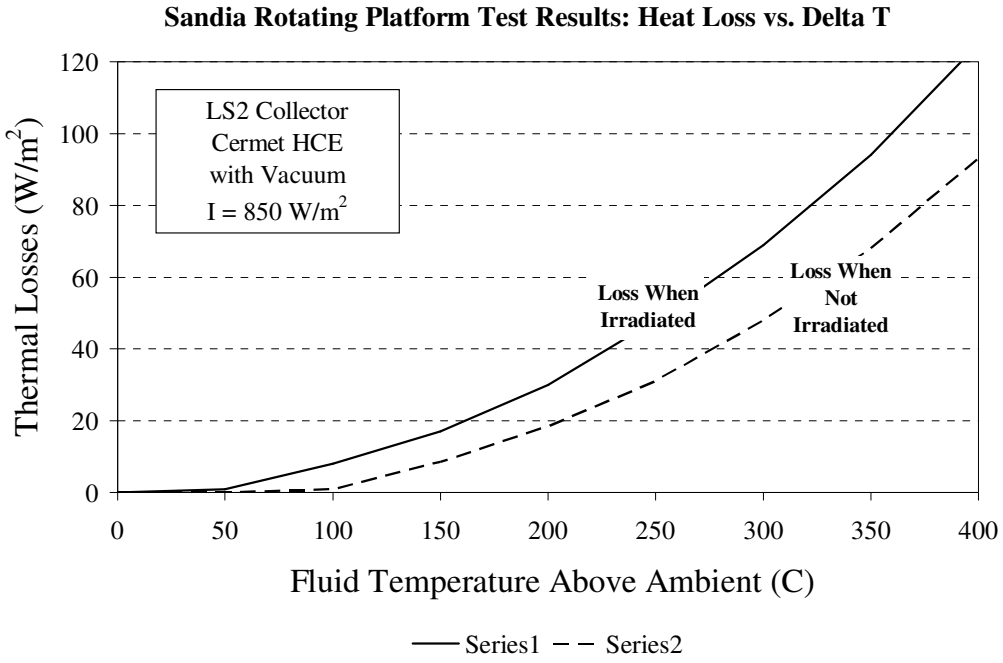

Figure 2.7.1b: Heat Loss Results from Sandia Rotating Platform Collector Tests [Dudley et al, 1993]

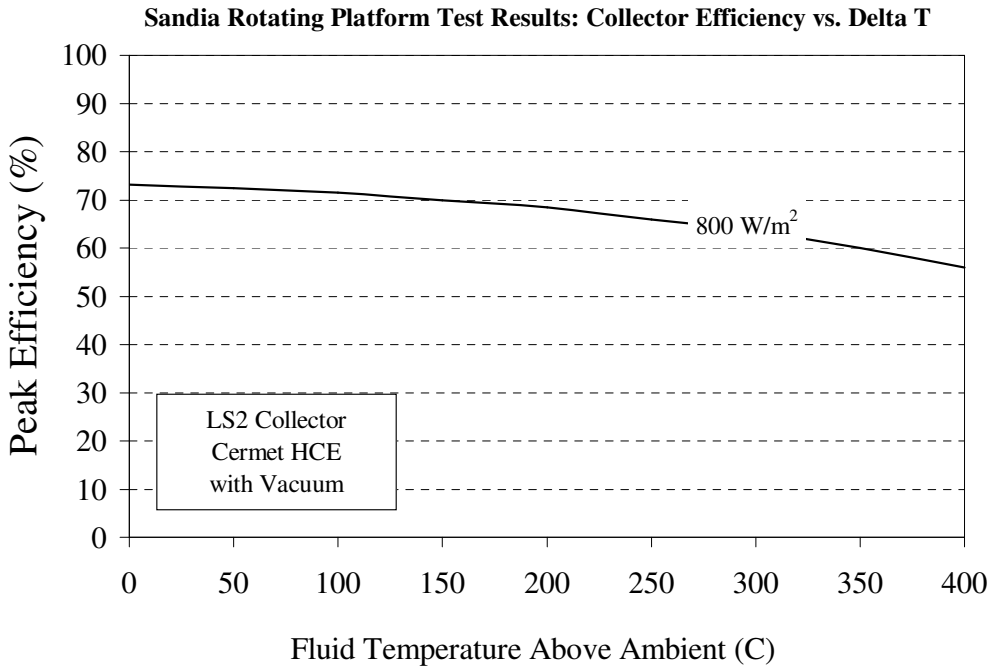

Figure 2.7.1c: Collector Efficiency Results from Sandia Rotating Platform Collector Tests [Dudley et al, 1993]

CHAPTER 3: PROJECT OVERVIEW

3.1 PROJECT OBJECTIVES AND GENERAL PROCEDURES

The goal of this project was to determine the optimal placement of collector types in a typical SEGS solar field to maximize cost effectiveness and maintain operating efficiency. Motivation for this study stems from the observation that the current receiver tube technology focuses on maximized efficiency at the highest temperatures, but gives little consideration to performance at lower operating temperatures. It is unlikely that a receiver tube designed for optimal performance at 370 C is also the most suitable at 280 C. Moreover, the high cost of the state-of-the-art receivers is due in large part to the solar selective absorber coating material and the vacuum annulus, both of which may not be necessary features for a collector designed for low temperature operation. A receiver tube with a flat black enamel absorber coating and no vacuum in the annulus would cost significantly less to manufacture and maintain than the current receivers. It was hypothesized that employing specially designed "low temperature receivers", with a flat black enamel absorber coating and low conductivity gas in the annulus, at the cool ends of the SCA loops would increase the cost effective operation of a SEGS solar field.

The proposed receiver design employs Pyromark [Wade, 1962] as the absorber coating, because of its low cost and demonstrated high absorptive power and stability at high temperatures. It has already been used in the refurbishment of broken collectors in SEGS solar fields, and has proven to be a relatively effective alternative coating, but it has a higher emissivity than the cermets currently used in the SEGS units. Filling the annular space with air is considered, because it has been observed at SEGS that the annulus vacuum can be compromised in some cases, either from cracks or holes in the glass envelope or from failure of the glass to metal seal at the bellows. Although air-filled receivers would have lower performance, they may be sufficient to use in the cold section of the collector loop. If so, using such receivers could significantly lower cost and negate any maintenance required from air leaking into the annulus. In addition, the presence of a low conductivity gas in the

annulus would neutralize the heat loss effects of a hydrogen leak in the annulus. At the highest operating temperature, with a vacuous annulus, a small amount of leaked hydrogen gas would have a conduction coefficient of approximately 0.324 W/m·K [Incropera, 2002]. However, if the Hydrogen leaked into an annulus filled with air at atmospheric pressure, the relative amount of Hydrogen in the two gas mixture would likely be very small, probably around a mole fraction of 0.01. Based on the equations for the conduction of gas mixtures developed by Mason and Saxena [1958] the conduction coefficient of the Hydrogen-Air mixture at this mole ratio would be approximately 0.051 W/m·K, a dramatic drop in value from that of pure Hydrogen. Two different gases were analyzed in the annulus of the low temperature receiver; air and argon. Argon was considered for its superior insolating capabilities.

The hypothesis was tested by simulating the performance of a SEGS solar field and energy conversion plant with different arrangements of collector types in the field. In order to develop and execute an accurate simulation program, several intermediate tasks needed to be completed. The individual phases of this project are presented sequentially below:

1) Collection and processing of solar field (test loop) and energy conversion plant (plant performance) data from an operational SEGS facility.
2) Evaluation of solar collectors in the field and development of efficiency models for each type of collector (categorized by type/condition of receiver tubes) based on processed test loop data.
3) Modeling of entire SEGS unit performance (including solar field, gas heaters, steam power plant, and energy conversion) using plant performance data.
4) Development of theoretical individual receiver tube model to simulate and predict the thermal performance of proposed “low cost” receiver tubes under typical solar field operating conditions.
5) Integration of data-based collector efficiency models, theoretical receiver tube performance models, and overall SEGS unit performance models to simulate solar field and plant operation based on various theoretical collector arrangements in the solar field.

The data used for the SEGS modeling was collected at the SEGS VIII facility at Harper Dry Lake in the southern Mojave Desert. A more detailed explanation of the specific data collected and instrumentation used will be given in a later section. SEGS VIII is the second newest unit, beginning operation in 1990, and it has the largest solar field, with a total

aperture area of 484,000 square meters, and highest output capacity of the nine plants, 80 MW. SCA specifications and collector field information for SEGS IX relevant to modeling calculations are listed in Table 3.1.1.

Table 3.1.1: SCA and Solar Field Specifications for SEGS Unit VIII

Number of SCA Loops	142
Number of SCAs	852
Solar Field Aperture Area	464,340 m^2
Number of Collectors per SCA	24
SCA Length	95.2 m (net)
SCA Aperture Area	545 m^2
Focal Length	1.71 m
HCE Radius	3.5 cm
Parabolic Reflectivity	0.94

Three computer software programs were employed to complete the five main tasks of this project; Microsoft Excel, Visual Basic for Applications (VBA), and Engineering Equation Solver (EES). Excel was used to organize collected data and simulation results. VBA code was used in the processing and summarizing of data, development of collector efficiency models, and plant simulation. The theoretical receiver tube model was written and executed in EES. Table 3.1.2 lists the main programs written to accomplish all project tasks and their basic functions.

Table 3.1.2: Computer Programs Written to Complete Project Tasks

Program Title	Code Source	Function
Test Loop Processor	VBA/Excel	- Process Test Loop data - Develop data-based collector efficiency models
Plant Performance Processor	VBA/Excel	- Summarize Plant Performance date - Create Summary date file for SEGS Simulator - Use data to generate energy conversion models
Receiver Model	EES	- Model the heat loss from theoretical receiver types
SEGS Simulator	VBA/Excel	- Simulate performance of theoretical SEGS solar fields by integrating all other program results

The following text in this thesis will present and explain in detail each program that was written in the completion of the project tasks.

3.2 INSTRUMENTATION AND DATA COLLECTION

SEGS data was collected and organized from the two main cycles of the facility; the solar field HTF cycle and the steam turbine cycle. The solar collectors at SEGS VIII were originally installed with resistance temperature detectors (RTD) at the midpoint of each SCA. At the onset of this project, additional RTDs were strategically installed in two test loops in the field. An RTD was placed at each junction of two SCAs, so that SCA inlet and outlet temperatures could me measured and used for modeling purposes. The two test loops were comprised of a variety of collectors whose receiver tubes ranged in condition from brand new UVACs to completely degraded Luz HCEs. Collectors of similar receiver type and condition were grouped together so that their performance could be analyzed more readily. Figure 3.2.1 illustrates the arrangement of instrumentation in the two test loops and the organization of the collector groups.

The circles labeled with "T__" are the RTDs. The labels in the figure represent the specific identification number of the RTDs used for data processing. RTDs labeled in bold and red represent those that were installed and calibrated after 2002, while ones labeled in standard text represent the originally installed instruments. The two symbols marked "FM1" and "FM2" represent flow meters placed within the HTF pipe/absorber tube. These are used to measure the volumetric flow rate of the heat transfer fluid, an important parameter in heat rate calculations. The cold and hot headers are represented by "CH" and "HH", respectively.

As Figure 3.2.1 shows, row 41 is made up of new UVACs. Row 42 is comprised of a variety of collector types, the majority of which show significant degradation. The "cloudy glass" collectors in group 424 are those whose absorber coating has broken down and formed particulates on the glass envelope's inner surface, leaving a cloudy or "fluoresced" receiver tube. The "silvery surface" collectors in group 422 have had significant coating breakdown and have been washed out, which leaves the steel absorber surface exposed in some areas

giving it a silvery look. Receivers whose glass envelope has been broken are located in group 421, and receivers that have lost vacuum in the annulus are in group 423. The "OK used HCEs" in row 43 and group 426 have not exhibited any significant degradation and still have glass envelope and absorber coating intact and vacuum in the annulus. The "refurbished HCEs" in row 44 and group 425 have had the absorber tube recoated with Pyromark enamel and have air at atmospheric pressure in the annulus.

Additional data collected in the field, and included with the test loop data, are ambient temperature and beam irradiation on the tilted plane, I_T. Beam irradiation was measured in the field using a shielded tracking pyranometer. Measurements in the test loop were recorded every four minutes and collected into a data file, which was used in the Test Loop Processor spreadsheet.

Data pertaining to the overall performance of the solar field and energy conversion plant was simultaneously collected. This included inlet and outlet HTF temperatures of the solar field, gas heaters, and heat exchangers, HTF flow rates in the solar field, gas heaters, and heat exchangers, and relevant steam temperatures throughout the steam turbine cycle. Solar beam normal irradiation was measured by three, independently operating, Normal Incidence Pyrheliometers (NIP). Data for ambient conditions, temperature, wind speed, and relative humidity, was also gathered and included in the spread sheets generated at SEGS VIII. Plant performance data was collected in four minute increments and assembled into Excel spreadsheets for each month. These records were used to model the operation/performance of SEGS VIII over a one year period. Figure 3.2.2 shows a schematic of the SEGS VIII facility with data collection instrumentation included.

The current model does not consider transient effects. A transient model was initially considered, but was deemed unnecessary for accurately representing system performance. One may speculate that a transient model would predict slightly lower performance, due to lower solar irradiation and solar field heat collection during morning start-up and evening shut-down. This consideration would lead to model results somewhat closer to measured performance; however, as will be presented, the model without transient effects still produces results that are in excellent agreement with measured data.

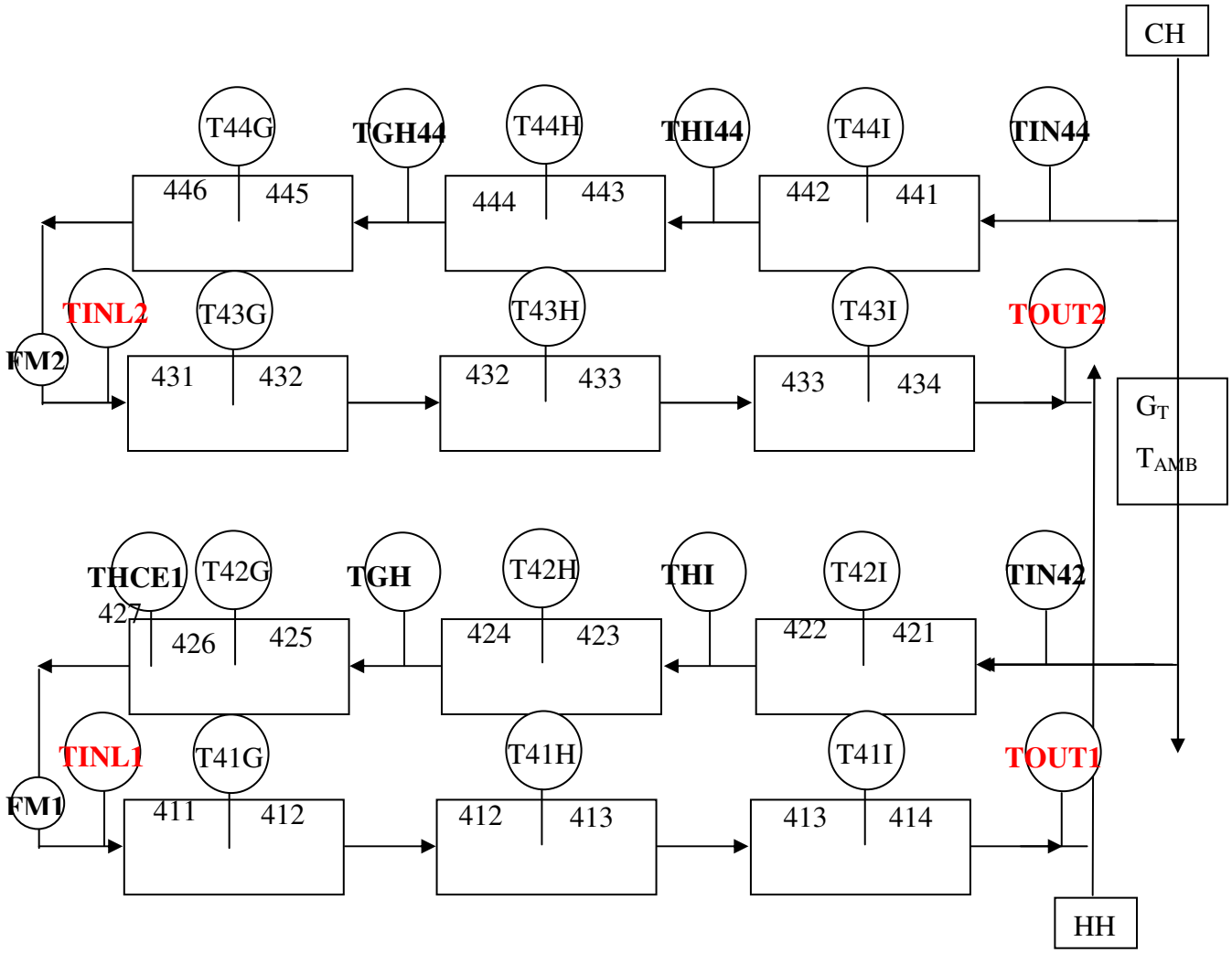

Receiver Groups

411	12 UVACs	421	12 HCEs broken glass
412	24 UVACs	422	12 HCEs silvery surface
413	24 UVACs	423	12 HCEs lost vacuum
414	12 UVACs	424	12 HCEs cloudy glass
		425	12 refurbished HCEs
		426	9 used OK HCEs
		427	3 new Schott
431	12 OK used HCEs	441	12 refurbished HCEs
432	24 OK used HCEs	442	12 refurbished HCEs
433	24 OK used HCEs	443	12 refurbished HCEs
434	12 OK used HCEs	444	12 refurbished HCEs
		445	12 refurbished HCEs
		446	12 refurbished HCEs

Figure 3.2.1: Schematic of Field Instrumentation and Receiver Identification

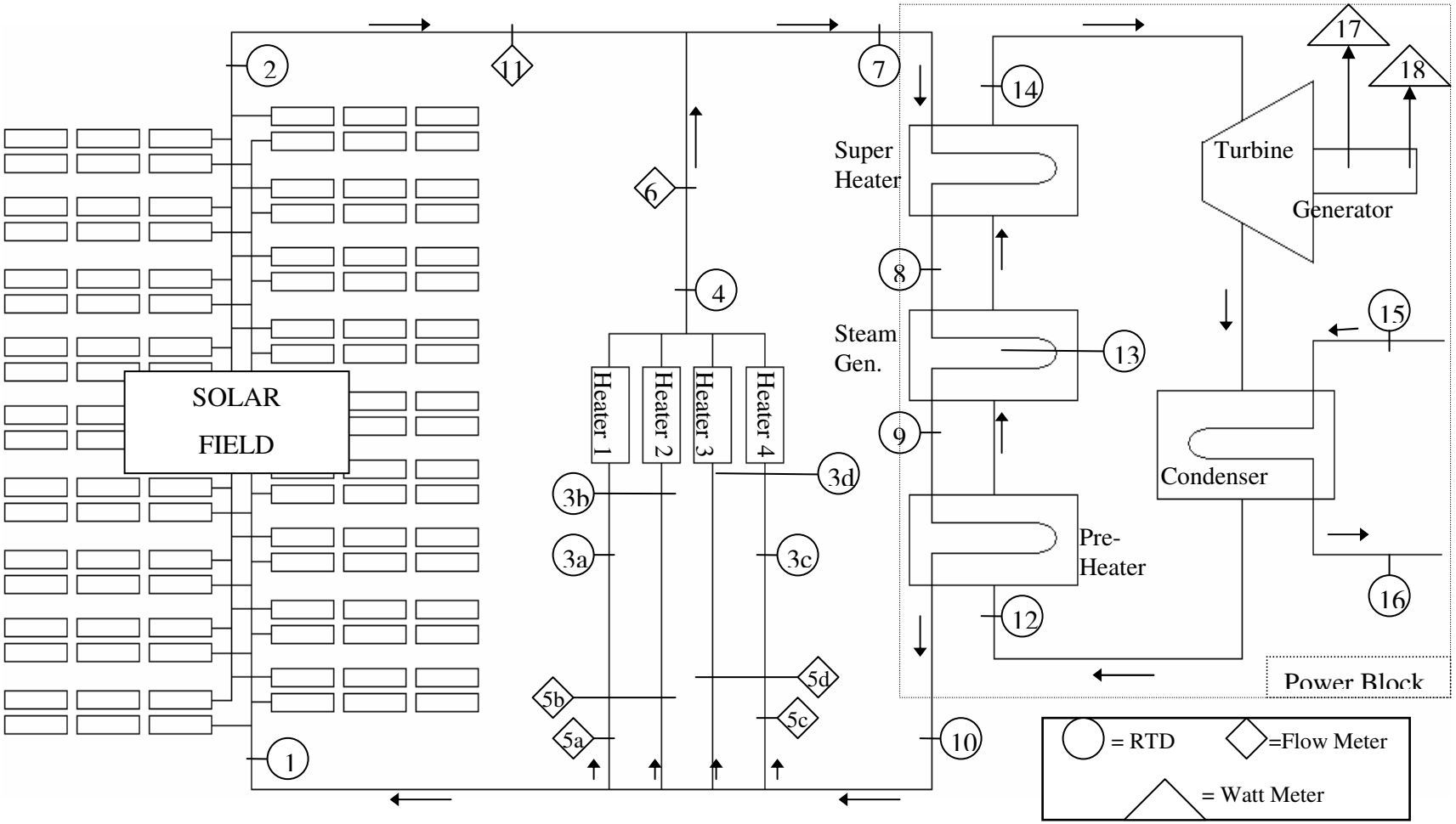

1. Solar Field inlet HTF temperature	7. Power Block inlet HTF temperature	13. Steam Generation temperature
2. Solar Field outlet HTF temperature	8. Steam Generator inlet HTF temperature	14. Superheater outlet steam temperature
3(a-d). Gas Heater inlet HTF temperatures	9. Steam Generator outlet HTF temperature	15. Condenser inlet cooling water temp
4. Gas Heater outlet HTF temperatures	10. Power Block outlet HTF temperature	16. Condenser outlet cooling water temp
5(a-d). Gas Heaters HTF flow rate	11. Solar Field HTF flow rate	17. Gross MW output
6. Combined Gas Heaters HTF flow rate	12. Preheater inlet water temperature	18. Net MW output

Figure 3.2.2 Schematic of SEGS Facility with Plant Performance Data Collection Instrumentation

CHAPTER 4: ANALYSIS AND EVALUATION OF SEGS TEST LOOP

4.1 COLLECTOR EVALUATION USING "TEST LOOP PROCESSOR"

The Test Loop Processor program is written in Visual Basic language and is executed in Microsoft Excel. This program is used primarily to process temperature data from the two SEGS test loops and to use this data to develop mathematical models for the efficiency of each employed collector type. As the majority of results and conclusions of this study relied on computational modeling, it is important to describe the various modeling routines and procedures used. Hence, the following will give a detailed explanation of the test loop program and how it is executed.

Data from the test loops, represented in Figure 3.2.1, is recorded in four minute increments and organized into a basic text file. Each line of data includes the year, day, and time of the given measurements, the HTF temperature at the input, output, and center of each SCA, HTF flow rates through each test loop, and the tilted beam irradiance incident on the collectors. A data averaging routine in the processor inputs this data line by line and calculates the average value of each measured parameter over an hour time period. This hourly data is recorded into an averaged test loop data file which is used for processing.

The averaged test loop data is then inputted into a conversion routine where the raw data is adjusted based on instrument calibrations, which were performed prior to the start of this project. The originally installed RTDs were calibrated in 2004, and the newly installed RTDs were calibrated in October of 2005. All converted data is recorded into an Excel spreadsheet. For each hour, the HTF temperature at each RTD in the test loop is recorded in a temperature scan, which monitors the temperature distribution across the loop. Figure 4.1.1 shows a representative temperature scan. HTF temperature is plotted against the distance from the loop inlet, illustrating the effects of heat collection by the HTF as it flows through the loop.

Periods of low irradiance measurements are neglected by the data converter. The conversion routine incorporates a threshold irradiance value of 800 W/m^2, and it discards any periods of data with irradiance under this value. 800 W/m^2 was selected to ensure that only clear sky conditions prevailed in the data processing. With unclear sky conditions, the oil pump speed and flow is typically varied excessively to maintain the nominal field inlet temperature (270°C), causing lag in the field outlet temperature, which in turn caused widely varying collector efficiency data. Thus, when the irradiance is variable, the efficiency data is consequently erratic. To avoid this misleading variation, it is desirable to analyze the collector performance when only considering hours of sufficient irradiance. Figure 4.1.2 illustrates the difference in scattering, of a typical efficiency plot for "Used HCEs", between results using 800 W/m^2 and 400 W/m^2.

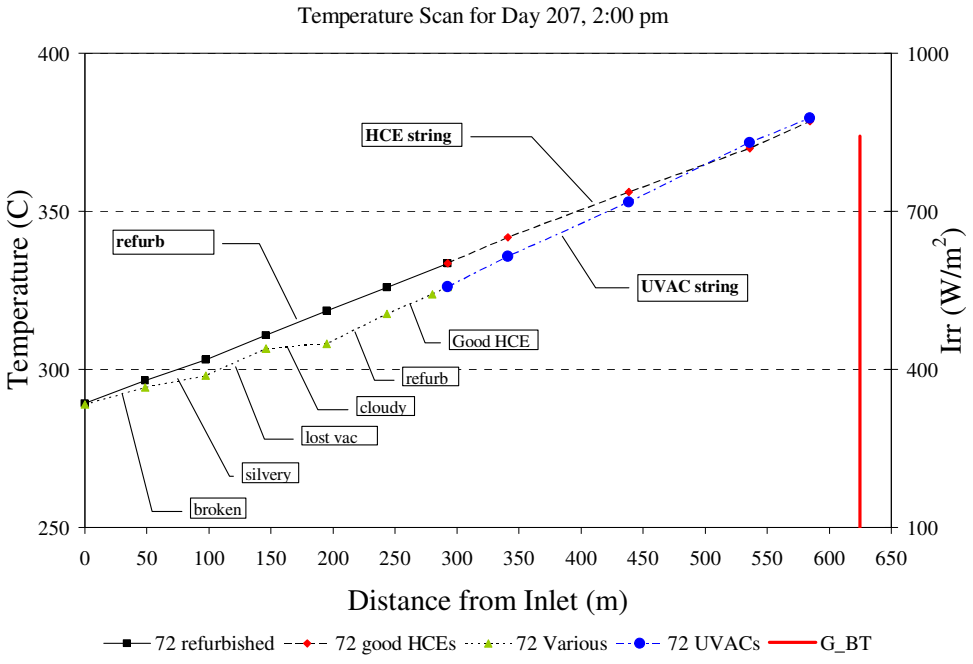

Figure 4.1.1: Typical Temperature Scan of Test Loop Data

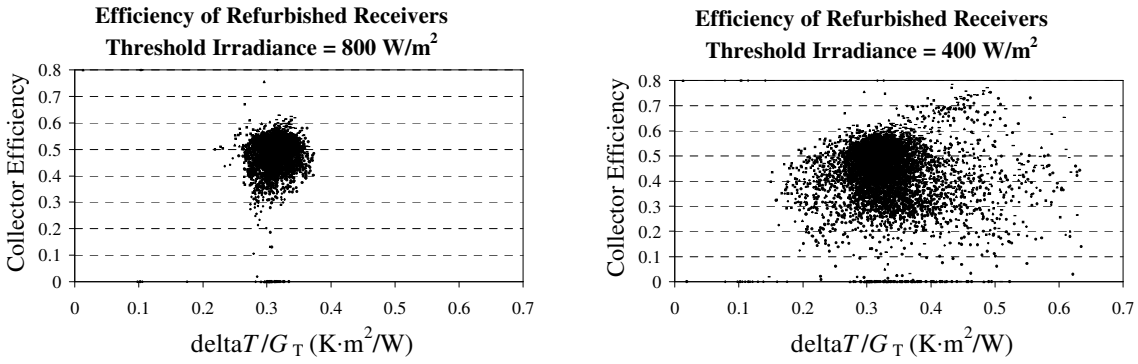

Figure 4.1.2: Comparison of Efficiency Data for Different Threshold Irradiances

Once the data is calibrated and organized, by day and time, in the spread sheet, the Test Loop Processor calculates the efficiencies of each group of collector types for each hourly period of data. Efficiencies are calculated by Equation 2.5.1, where the useful heat collected, $\dot{Q}_u$, is found using the basic equation for the total heat collected by a fluid flowing through a circular tube. It has units of kilowatts (kW).

$$\dot{Q}_u = \dot{m}_{HTF} C_{p,HTF} \Delta T \tag{4.1.1}$$

The change in temperature is the difference between the measured inlet and outlet temperatures of the collector group under consideration, corresponding to the instrumentation shown in Figure 3.2.1. The HTF mass flow rate, $\dot{m}_{\mathrm{HTF}}$ $[\mathrm{kg/s}]$, is computed from the data for volumetric flow rate, $\dot{V}_{\mathrm{HTF}}$,which is measured in m^3/hr.

$$\dot{m}_{\mathrm{HTF}} = \dot{V}_{\mathrm{HTF}} \rho_{\mathrm{HTF}} \Big/ 3600 \tag{4.1.2}$$

The fluid density, ρ_{HTF} $[\mathrm{kg/s}]$, is a function of HTF temperature. The Test Loop Processor contains regression coefficients for the temperature dependence of density and

specific heat, $C_{p,HTF}$ $[kJ/kg \cdot K]$, of Therminol VP1, the HTF used in SEGS VIII. These fluid properties are calculated at the average fluid temperature of the collector group.

In accordance with Equation 2.5.1, the useful heat collection is divided by the total incident beam irradiance, $G_{BT}A_{ap}$ $[kW]$, to determine the collector efficiency. The aperture area is not fixed for all groups, because the number of collectors differs between them. Each collector group's aperture area is determined, based on SCA data in Table 3.1.1 and collector group data in Figure 3.2.1, at the start of the Test Loop Processor and designated as a public variable. The computed efficiency for each collector group is recorded in the spreadsheet for each hourly period, along with the solar parameter, which is defined by,

$$\text{Solar Parameter} = \frac{T_{avg} - T_{amb}}{G_{BT}} \tag{4.1.3}$$

Ever since the development of the Hottel-Whillier-Bliss equation for solar collector performance [Hottel and Whillier, 1955, and Bliss, 1959], it has been universally recognized that such a plot of collector efficiency versus the so-called solar parameter of Equation 4.1.3 is the best concise representation of solar collector performance. This model or an appropriate upgrade, is still arguably the best acceptable presentation model even for concentrators and for collectors of any type that operate higher than usual operating temperatures. In the case of linear concentrators, special caution must be observed when interpreting data to recognize the additional scatter in data will be caused by off normal operation. In off-normal operation, the optical efficiency, which is effectively the vertical intercept on the plot, will decrease and shift the entire efficiency curve downward as the transmittance and absorptance is decreased. In addition, the non-linear heat loss resulting at high temperature operation of a concentrator in solar power applications will cause additional scatter in the data.

Even considering the previous limitations this plot of efficiency versus solar parameter remains the best concise representation and is the best choice for representing the research in this thesis. Plots of collector efficiency vs. solar parameter are generated for each collector type in Excel. These plots are used to develop the collector efficiency models.

4.2 INSTRUMENT CALIBRATION IN THE TEST LOOP PROCESSOR

Preliminary results from the Test Loop Processor showed that certain instruments in the field were giving erroneous data. The inaccurate data collected from these sources, mainly two RTDs in the refurbished collector group and the shielded tracking pyranometer, were causing noticeable deviations from expected results. Closer evaluation of the data from these instruments showed that further calibrations, in addition to the standard calibrations done in the field, would need to be incorporated into the Test Loop Processor program.

Calibration of RTDs in the Refurbished Collector Test Loop Group

Preliminary collector efficiency data showed significant scattering for collectors in the refurbished HCE group, as is illustrated by Figure 4.2.1. Further observation of the test loop temperature scans led to the conclusion that RTDs THI44 and TGH44, located in the refurbished string, were reading a fluid temperature that appears to be erroneously low. Figure 4.2.2 shows a typical test loop temperature scan, which illustrates the trend of low readings at THI44 and TGH44. During normal operation, the refurbished string is expected to have a linear temperature distribution across the length of the SCA, as the inlet and outlet temperatures are kept constant; however, the temperature scans generated showed a clear deviation from the expected linear behavior at RTDs THI44 and TGH44. These RTDs were added just for this test program, and the exposed thermowell and junction boxes were not well insulated, as were the originally installed RTDs. It was assumed that exposure of the protruding RTDs to ambient conditions was creating a fin effect, causing convective heat transfer and altering the temperature read by the RTD at the bottom of the thermowell. The erroneously low temperature readings could cause the calculated efficiencies of collector rows 442 and 444 to be too low and the efficiencies of collector rows 443 and 445 to be too high, resulting in the scattered data in Figure 4.2.1.

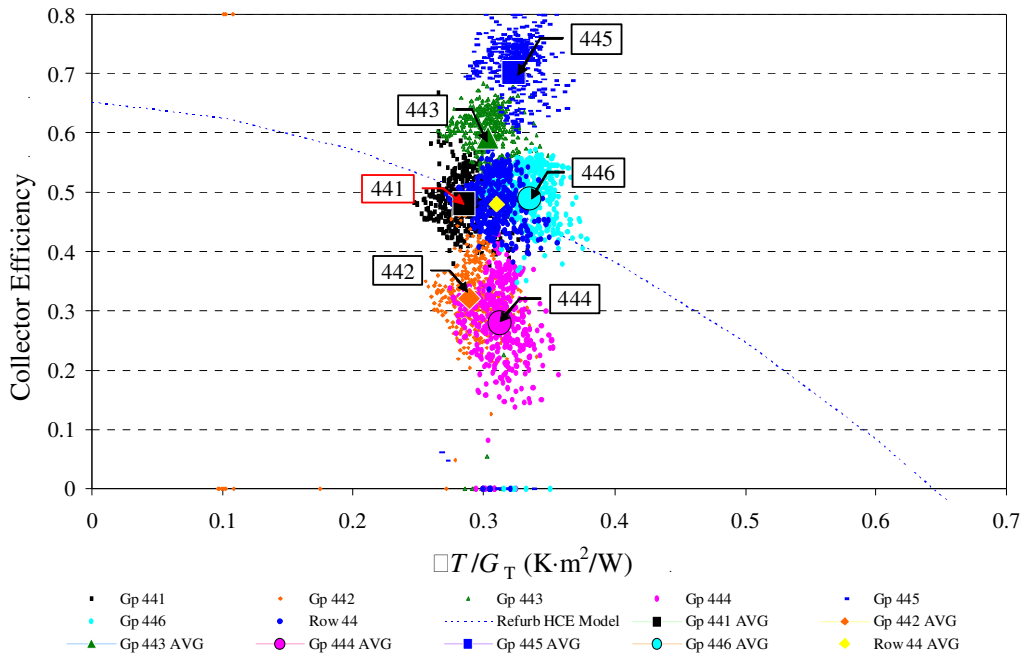

Figure 4.2.1: Initial Efficiency Data for Row of Refurbished HCE

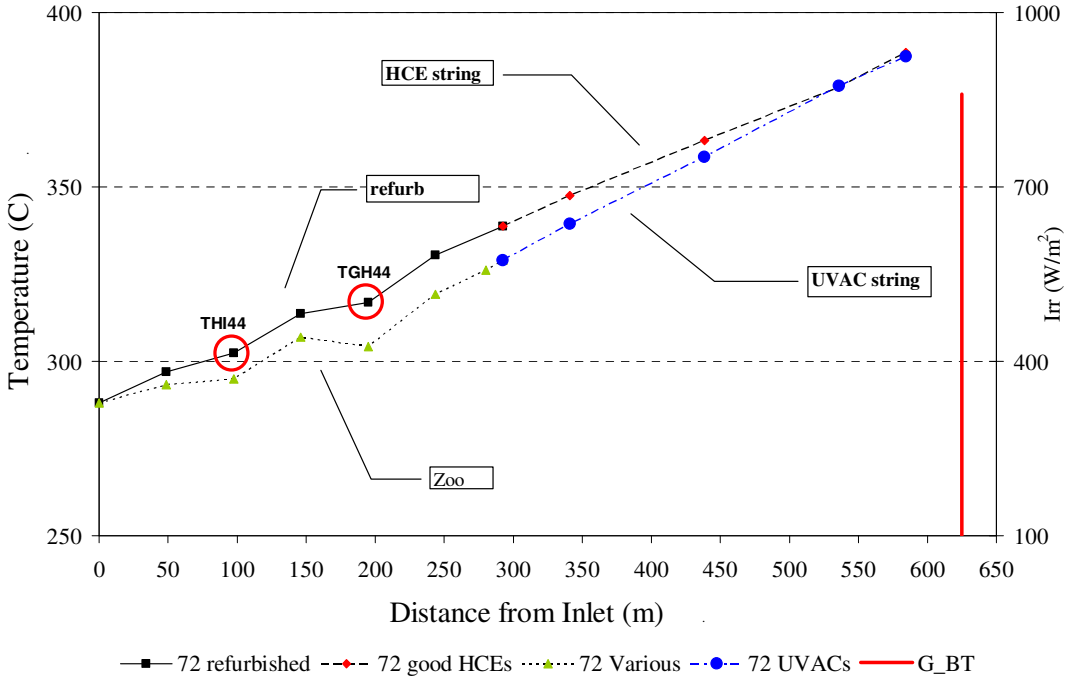

Figure 4.2.2: Typical Test Loop Temperature Scan Generated for an Arbitrary Hour of Data

In April of 2006, the suspected faulty instruments were insulated to correct the problem. Subsequent measurements showed an increase in THI44 and TGH44 temperature readings and the temperature distribution over the refurbished collector string was linear in the temperature scans, as expected. Figure 4.2.3 shows the temperature scan for the same hour of data as that of Figure 4.2.2, but with the faulty RTDs now insulated. RTDs THI42 and TGH42 in the "Zoo" group were also insulated, also resulting in higher temperature readings at these locations. Group 42 still does not have a fully linear distribution, but due to the extreme degradation of most collectors in this group, a constant temperature increase is not necessarily expected for those SCAs.

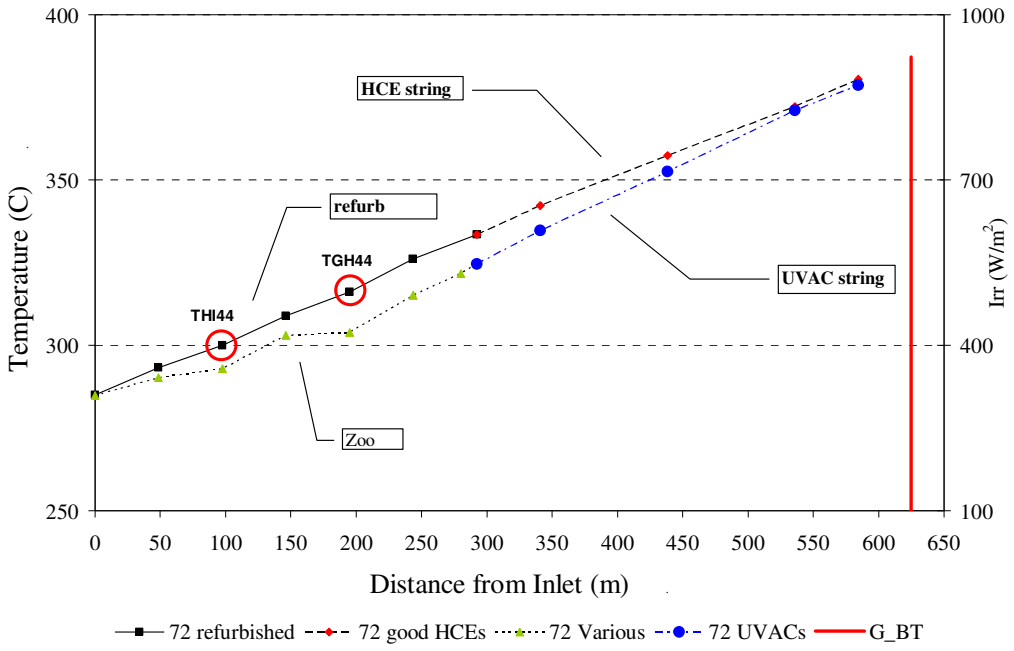

Figure 4.2.3: Typical Test Loop Temperature Scan with Insulated THI44 and TGH44 RTDs

With the new, more accurate temperature measurements, the corresponding efficiency calculations led to a dramatic reduction in scatter in the efficiency data. Figure 4.2.4 shows the efficiency data for the refurbished HCE group collected after the insulation of the RTDs.

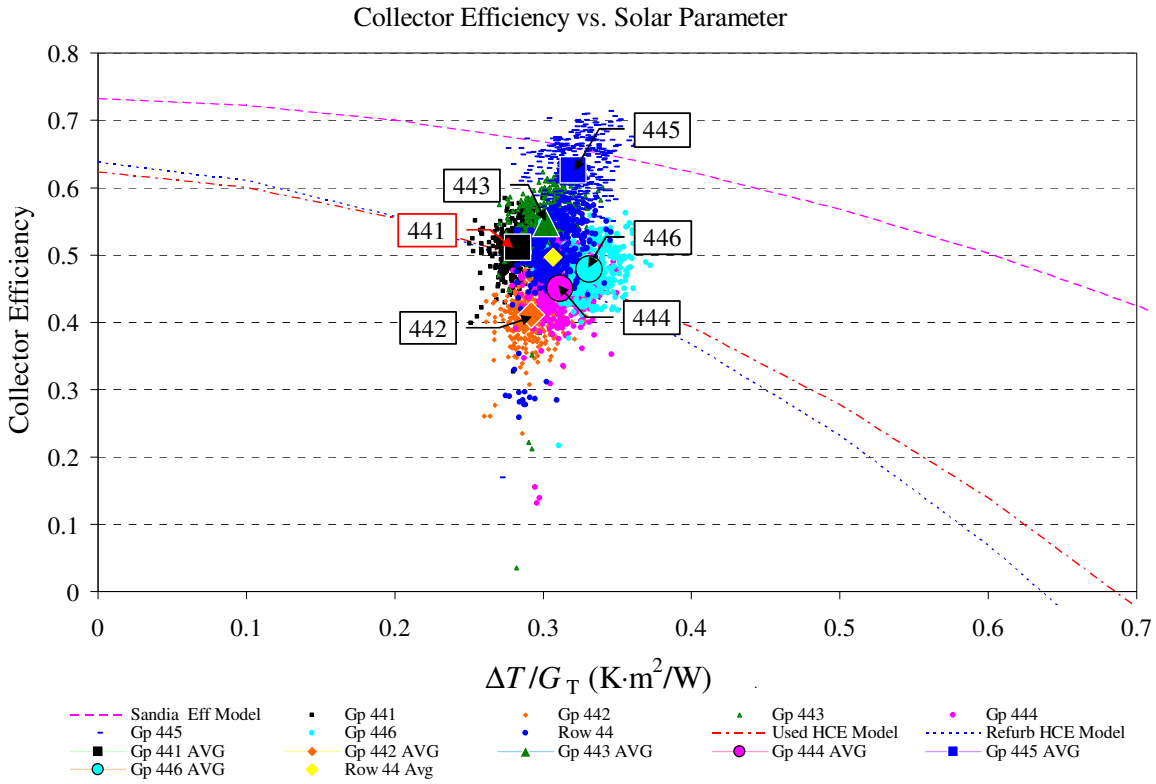

Figure 4.2.4: Refurbished Row Efficiency Data After Insulation of THI44 and TGH44 RTDs

All data collected after the insulation was added is considered correct and raw values can be used for processing; however, any data collected prior to this insulation is erroneously low, and must be corrected before any processing can be done. Because collector efficiency models were developed from data collected before the RTD insulation, this data needed to be calibrated to agree with the new more accurate data. Thermowell THI44 and TGH44 temperature data was statistically calibrated to coincide with the correct data gathered after insulation of the RTDs. These corrections were crucial, as they salvaged over a year's worth of data that would have otherwise been lost and impossible to reproduce.

Under ideal operating conditions the temperature at any RTD can be approximated by the average temperature of the two adjacent thermowells. According to the order of thermowells in the test loop, the approximate temperatures of THI44 and TGH44 can be calculated from the following equations:

$$THI44_{\text{Calc}} \approx \frac{T44H + T44I}{2} \quad ; \quad TGH44_{\text{Calc}} \approx \frac{T44G + T44H}{2} \tag{4.2.1}$$

THI44 and TGH44 temperature data from the 42 days prior to insulation and from the 42 days following insulation were simultaneously plotted against the calculated approximate temperatures from the Equation 4.2.1. The plots are shown in the following figures.

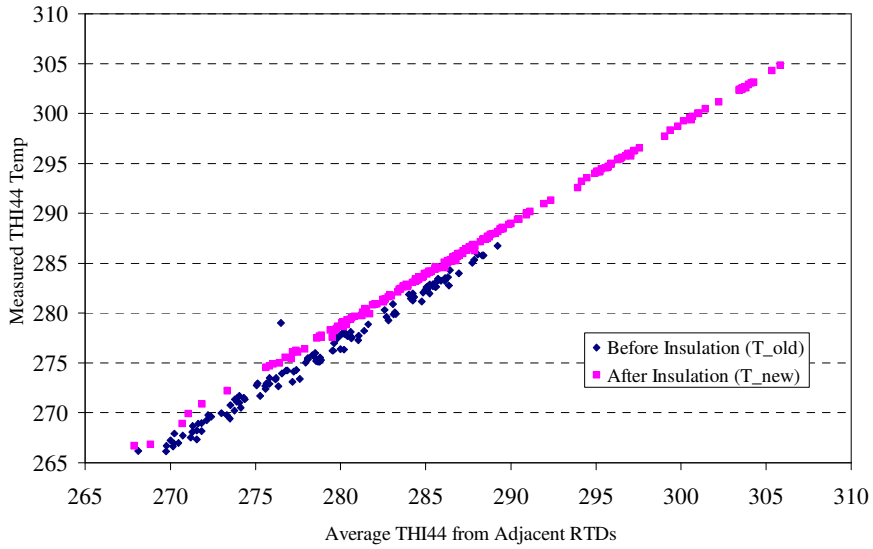

Figure 4.2.5: Comparison of THI44 Temp. vs. Calculated THI44 Temp. BEFORE and AFTER Insulation of THI44

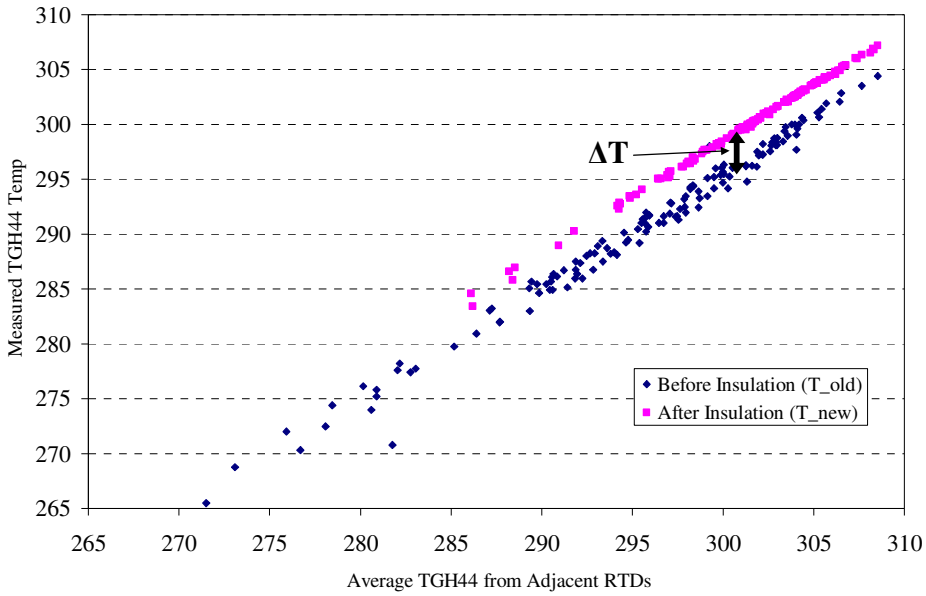

Figure 4.2.6: Comparison of TGH44 Temp. vs. Calculated TGH44 Temp. BEFORE and AFTER Insulation of TGH44

As Figures 4.2.5 and 4.2.6 illustrate, both pre and post-insulation temperatures are linearly dependent on the calculated temperature from Equation 4.2.1. The erroneous pre-insulation temperature, T_{old}, can be adjusted to the correct post-insulation temperature, T_{new}, by adding the difference between the two, ΔT.

$$T_{Corrected} = T_{old} + \Delta T \qquad (4.2.2)$$

Where, $\Delta T = T_{new} - T_{old}$

Both T_{old} and T_{new} can be represented as linear functions of the approximate temperature based on the adjacent RTDs, T_{Calc}. These linear equations can then be combined to generate an equation for ΔT based on T_{Calc} as the only independent variable.

$$T_{old} = C_{old} + b_{old} T_{Calc} \qquad (4.2.3)$$

$$T_{new} = C_{new} + b_{new} T_{Calc} \qquad (4.2.4)$$

Where C and b are constants/coefficients of the linear regression.

$$\Delta T = T_{\text{new}} - T_{\text{old}}$$

$$\Delta T = (C_{new} - C_{\text{old}}) + (b_{\text{new}} - b_{\text{old}})T_{\text{Calc}} \quad (4.2.5)$$

Then,

$$T_{\text{Corrected}} = T_{\text{old}} + (C_{\text{new}} - C_{\text{old}}) + (b_{\text{new}} - b_{\text{old}})T_{\text{Calc}} \quad (4.2.6)$$

Thus, the corrected temperatures of THI44 and TGH44 can be calculated from the measured erroneous fluid temperature and the average temperature of the two adjacent RTDs, two values provided in the collected test loop data. Tables 4.2.1 and 4.2.2 list the regression constants determined by the statistical comparison of data. The model uncertainties in these tables, and all subsequent uncertainties presented in this thesis, represent the 95% uncertainty limit.

Table 4.2.1: Regression Coefficients for THI44 Statistical Analysis

Constant	T_{Calc} Coefficient	Model R^2	Model Avg Uncertainty (U_A)
C_{old} = - 5.36	b_{old} = 1.01	0.996	0.30
C_{new} = - 3.75	b_{new} = 1.01	0.999	0.040

Table 4.2.2: Regression Coefficients for TGH44 Statistical Analysis

Constant	T_{Calc} Coefficient	Model R^2	Model Avg Uncertainty (U_A)
C_{old} = - 4.53	b_{old} = 1.00	0.985	0.51
C_{new} = - 7.66	b_{new} = 1.02	0.999	0.075

Figures 4.2.7 and 4.2.8 show the post-insulation temperatures and corrected pre-insulation temperatures plotted against T_{Calc}.

As the Figures show, the calibrated pre-insulation temperature data agrees with the data after insulation. Figure 4.2.9 shows the updated efficiency data using the corrected RTD temperatures. The calibration significantly reduces the scatter in data.

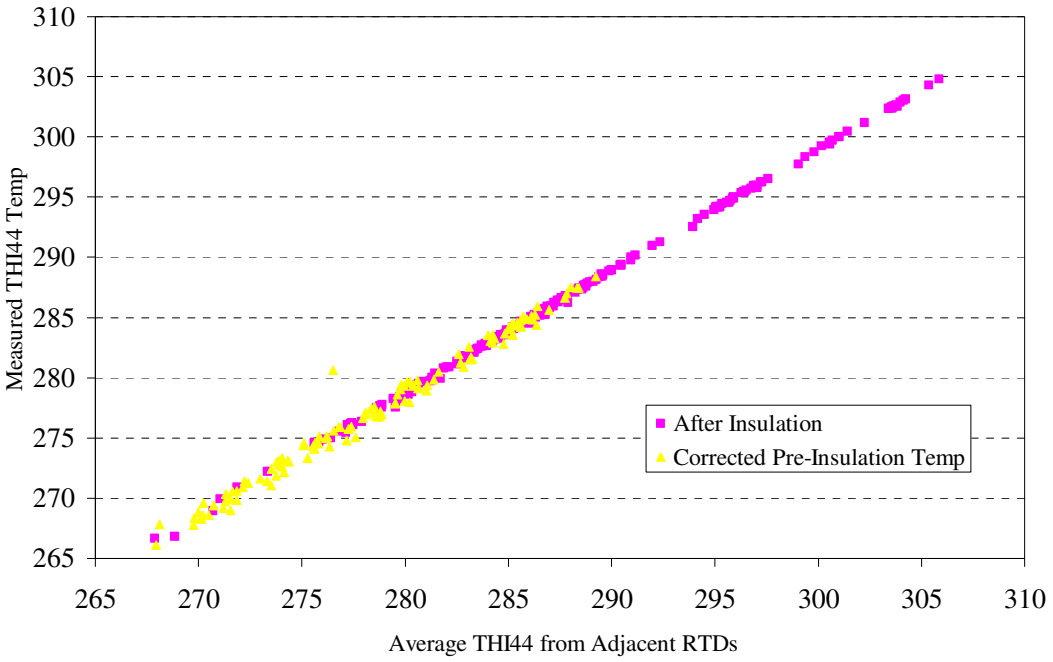

Figure 4.2.7: Comparison of Corrected pre-insulation temp and post-insulation temp of RTD THI44

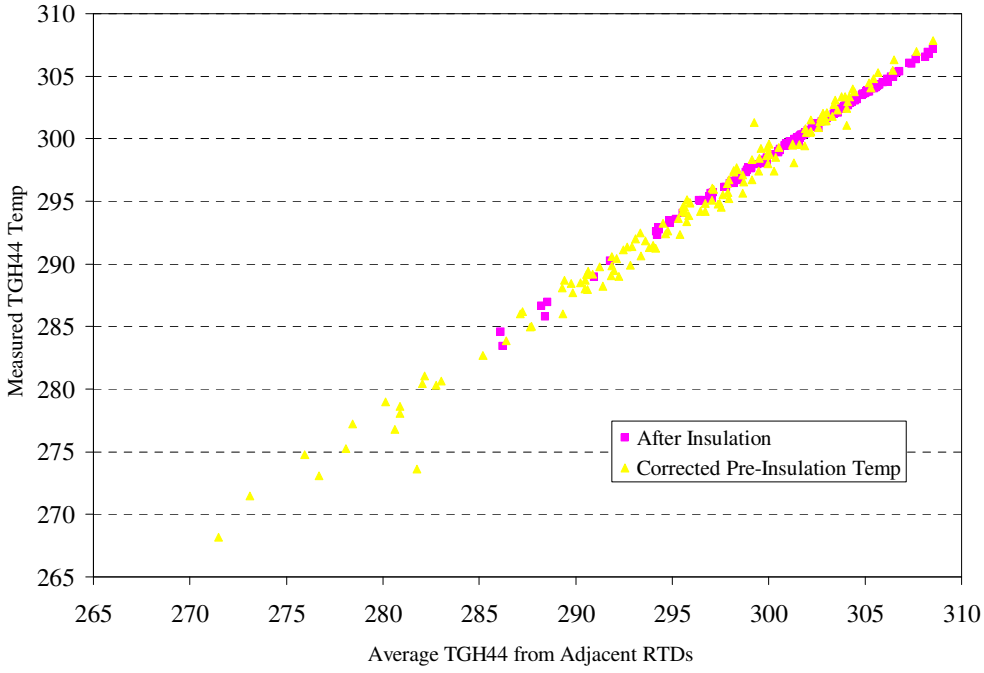

Figure 4.2.8: Comparison of Corrected pre-insulation temp and post-insulation temp of RTD TGH44

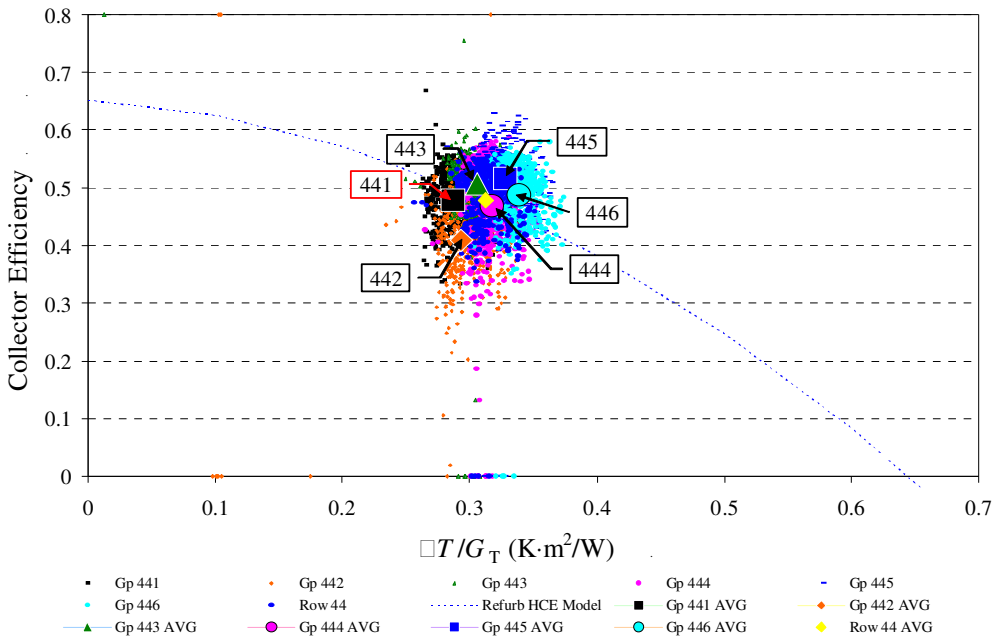

Figure 4.2.9: Collector Efficiency Data for Refurbished HCE Collectors with THI44 and TGH44 Calibrations

Calibration of the Shielded Tracking Pyranometer Tilted Beam Irradiation Data

The shielded tracking pyranometer is used at the SEGS plant to measure the solar irradiation on the tilted plane, I_T. Measurements are collected from this device in four minute increments, then averaged over each hour in the Test Loop Processor. The tilted plane irradiance can be used to calculate the average beam normal irradiance for each hour from the following equation:

$$I_{BN} = I_T / \cos\theta_T \qquad (4.2.7)$$

Where I_{BN} is the hourly average beam normal irradiation (W/m^2), I_T is the measured tilted plane irradiance, and cos θ_T is the cosine of the incident angle on the tracking (T) plane. This incident cosine was calculated in the Test Loop Processor for each hourly period using the solar angle relationships presented in Section 2.2. The time at the middle of the hour was used as the standard time for the solar angle calculations.

As aforementioned, the beam normal irradiance was also directly measured at four minute increments by three independently operating Normal Incidence Pyrheliometers (NIPs). Hourly measured NIP data was compared to the beam normal irradiance calculated in the Test Loop Processor with raw tilted plane irradiance data and Equation 4.2.7. These values were simultaneously plotted against time, along with a clear-sky model of solar irradiance. Figure 4.2.10 shows a representative sample of the calculated and measured beam normal irradiance for data from the end of August.

As the plot illustrates, the values of I_{BN} calculated in the Test Loop Processor were abnormally high; significantly higher than the measured NIP data and also higher than the clear sky model at times, which is theoretically erroneous since the clear sky model represents the maximum possible I_{BN}. Since the data from the three NIPs are in relative agreement with each other, it was assumed that this data is accurate. Solar time/angle calculations were manually performed and compared to the Test Loop Processor calculations. The results were in agreement, verifying the accuracy of the processor's calculations. It was concluded that the pyranometer used to measure I_T was producing erroneously high readings. To correct this problem the pyranometer data was calibrated to match the NIP data.

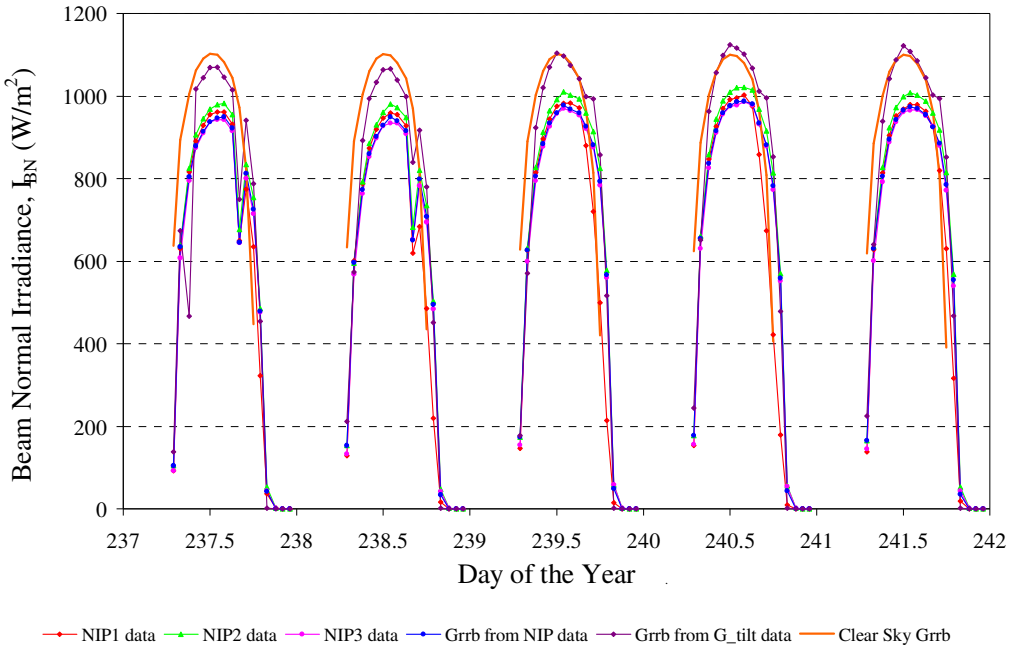

Figure 4.2.10: Plot of Beam Normal Irradiance vs. Time

Using time-corresponding test loop and plant performance data from July 12 to September 30, the values of hourly I_{BN} determined from the NIP data were plotted against the values of hourly I_{BN} calculated from the pyranometer titled plane irradiation data. The group of points is not roughly circular as might be expected, but is elongated in the horizontal direction. This distortion is inevitable since the actual measured irradiation is never much more than 1000 W/m^2, while the erroneous data from the field pyranometer is significantly higher than 1000 W/m^2. A homogeneous linear regression revealed that the I_{BN} values calculated from the pyranometer data were approximately 13% higher, on average, than the values measured by the NIPs. Figure 4.2.11 shows the regression plot and the linear regression trend line, and Table 4.2.3 shows the statistical results of the analysis. To minimize scatter and uncertainty in the analysis only I_{BN} values above 900 W/m^2 were included in the regression calculations.

Table 4.2.3: Pyranometer vs. Pyrheliometers Irradiance Regression Results

Regression Coefficient	0.8706 ± 0.0048
Alpha Risk	~ 0
R^2	0.998
Model Uncertainty (U_A)	± 5.3 W/m^2

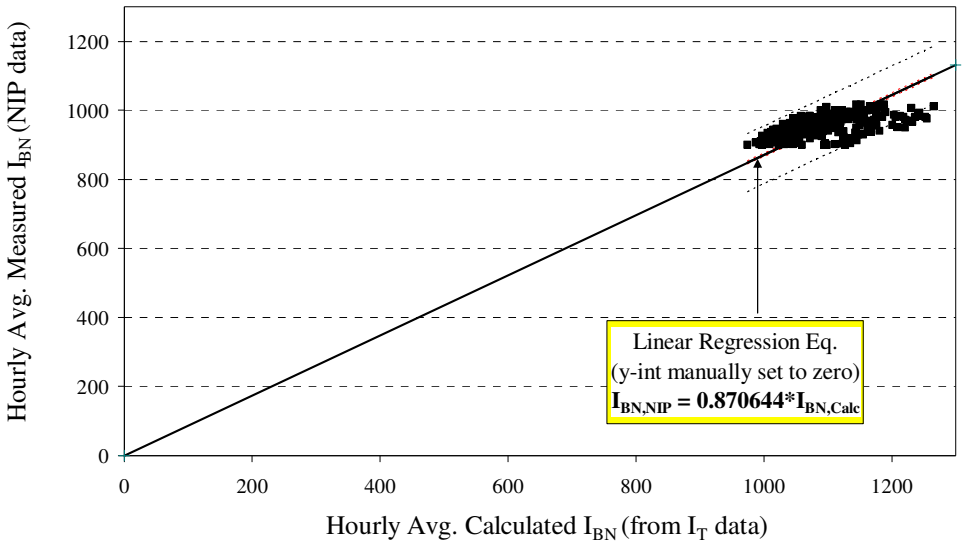

Figure 4.2.11: Regression Plot of I_{BN} from NIP data vs. I_{BN} Calculated from I_T data

The regression coefficient, 0.8706, gives the basic linear relationship between the two plotted parameters. The relatively small uncertainty in this value, ±0.0048, demonstrates that the estimation is accurate. The Model Uncertainty is only ± 5.3 W/m^2, which, when compared to values of solar irradiance between 900 and 1200 W/m^2, is a trivial amount of uncertainty.

The regression coefficient, 0.8706, was used as the calibration factor for the tilted plane irradiation data. Each value of I_T in the test loop spreadsheet was multiplied by this coefficient, so that the corrected beam normal irradiation would follow the modified equation:

$$I_{BN} = \frac{\mathbf{0.8706} I_T}{\cos\theta} \tag{4.2.8}$$

Calculations using Equation 4.2.8 produced values of beam normal irradiance in much better agreement with the NIP data. Figure 4.2.12 shows the same sample plot as Figure 4.2.10, but with the calculated I_{BN} employing the adjustment factor of 0.8706. Equation 4.2.8 was thus implemented into the Test Loop Processor's calculations of beam normal irradiance.

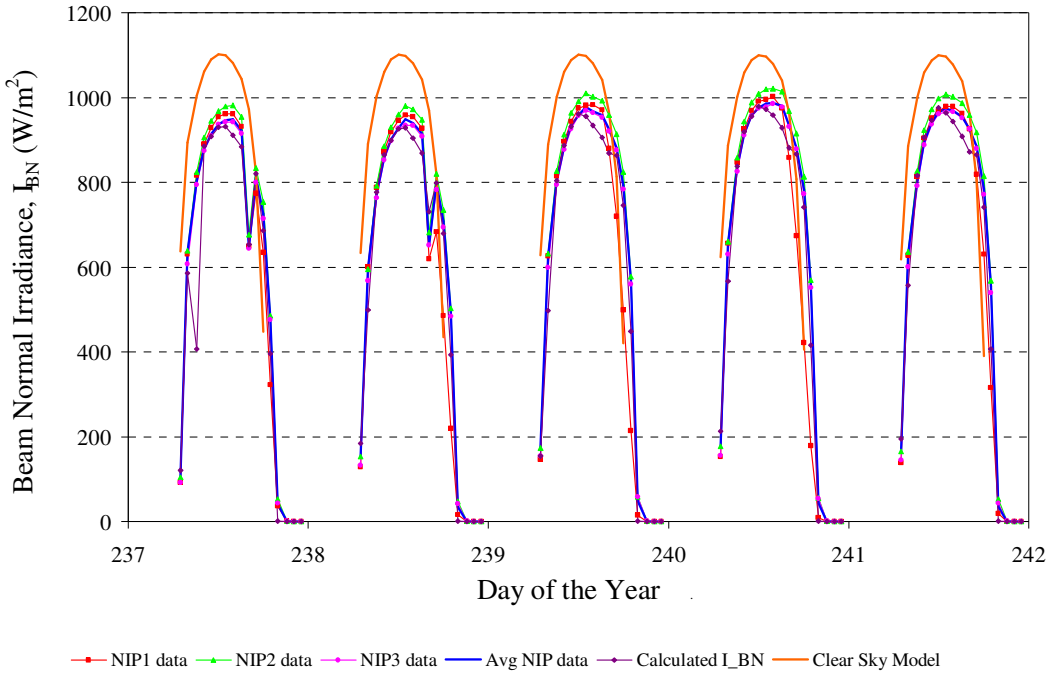

Figure 4.2.12: Plot of beam normal irradiance vs. time for days 237-242 w/ Calculated I_{BN} from Equation 4.2.8

4.3 ANALYSIS OF TEST LOOP DATA

With all calibrations from Section 4.2 applied, the raw SEGS data was processed and recorded in the temperature scans and efficiency plots described in Section 4.1. The temperature scan in Figure 4.1.1 shows the processed temperature data for all test loop locations on day 207 at 2:00 pm. This scan is representative of the majority of the temperature data. As the figure illustrates, one test loop consists of refurbished receivers in the cold leg and in-tact used HCEs in the hot leg. The other contains various degraded receivers in the cold leg and UVAC collectors in the hot leg. The fluid temperature is the same at each loop inlet, since all loops draw fluid from the same header.

The temperature change is nearly linear along each string of collector types, aside from the row of degraded HCEs (row 42). Temperature data from row 42 is expected to be somewhat irregular, as the collectors are significantly damaged and their performance is inconsistent. The largest deviation from a constant temperature increase occurs at the string

of silvery collectors and the string of cloudy collectors. This can be explained by the high reflectivity of the receivers under these conditions, as well as increased heat loss due to the particles in the annulus.

The slope of the temperature scan gives an indication of the performance of each collector type over the range of temperatures in which they are operating. A lesser slope corresponds to a smaller increase in temperature across a collector string and suggests lower receiver efficiency. In contrast, a large temperature increase over the same length of collectors indicates higher receiver efficiency. Based on Figure 4.1.1, the efficiency of the refurbished receivers at temperatures between 270 and 330 °C appears to be equal to that of the original in-tact used HCEs at temperatures between 330 and 380 °C, because the slopes of the two collector strings are virtually equal. The UVAC string has the largest slope and operates over the range of highest field temperatures. It can thus be inferred that these receivers have the highest heat collection efficiency. The UVACs maintain the same performance level at relatively high temperatures; however, a significant decrease in slope of the UVAC curve occurs at temperatures above about 370 °C. This may mean that the extreme high operating temperatures affect UVAC performance to some degree.

The processed efficiency data for the collector rows is presented in Figures 4.3.1 – 4.3.4. Each efficiency plot presents data for one collector type over the entire time period of data collection. Each point in a given plot represents one hour of data. Each isolated group of collectors within a row is designated by color, so that performance behavior at different fluid temperatures and SCA locations can be monitored. The mean of all data points is represented by a yellow diamond. The range of operating temperatures for each collector type is limited, making it difficult to observe any temperature dependent trends in performance. The scattering in the data is likely due to variations in ambient conditions such as wind and temperature, fluctuations in fluid flow rates, or minor inconsistencies in the instrumentation.

Within a given row of collector types, the variation in efficiency is somewhat sporadic from one group to another; however, the data does show a trend of decreasing efficiency over the length of each SCA. For example, in the refurbished receiver row, row 44, the first SCA is comprised of groups 441 and 442. The average efficiency drops from about 48% in group

441 to about 41 % in group 442. Similarly, the efficiency drops from 51% to 47 % between groups 443 and 444, which make up the second SCA. In the third SCA, the efficiency decreases by about 3% as well (group 445 to group 446). The same trend can be seen in the UVAC data, Figure 4.3.3. Here there is a significant loss of efficiency between groups 411 and 412, and also between groups 413 and 414. The UVAC plot also shows a considerable decrease in efficiency in the hottest receiver group, group 414. This is consistent with the temperature scans, in which the slope of the UVAC string generally decreased in the last group of collectors. These trends illustrate the decrease in collector performance at maximum operating temperatures.

Table 4.3.1 lists the calculated mean values of efficiency and solar parameter, $\Delta T/G_T$, for each collector type. The UVAC collectors are the most efficient, with an average efficiency of 61.2% at the highest operating temperatures. As was inferred from observation of the temperature scans, the efficiency of the refurbished receivers operating in the cold leg, 47.9%, is nearly equal to the efficiency of the in-tact vacuum HCEs operating in the hot leg, 48.8%. The 12 HCEs with lost vacuum and solar selective coating located in the cold leg, group 423, have an average efficiency of 58.8%. According to the temperature data, these receivers were exposed to temperatures in the range of 290 – 315 °C. Based on this information it can be assumed that the in-tact HCEs, still held at vacuum, would perform at above 60% efficiency in the cold leg of the loop.

The data suggests that a solar field loop comprised of low cost receivers, with no vacuum and non-selective coating, in the cold leg and normal vacuum HCEs in the hot leg would perform uniformly at nearly 50% efficiency over the entire length of the loop. The temperature scans show that such a collector arrangement is sufficient to raise the fluid temperature to 370 °C, the desired collector field output temperature for steam generation.

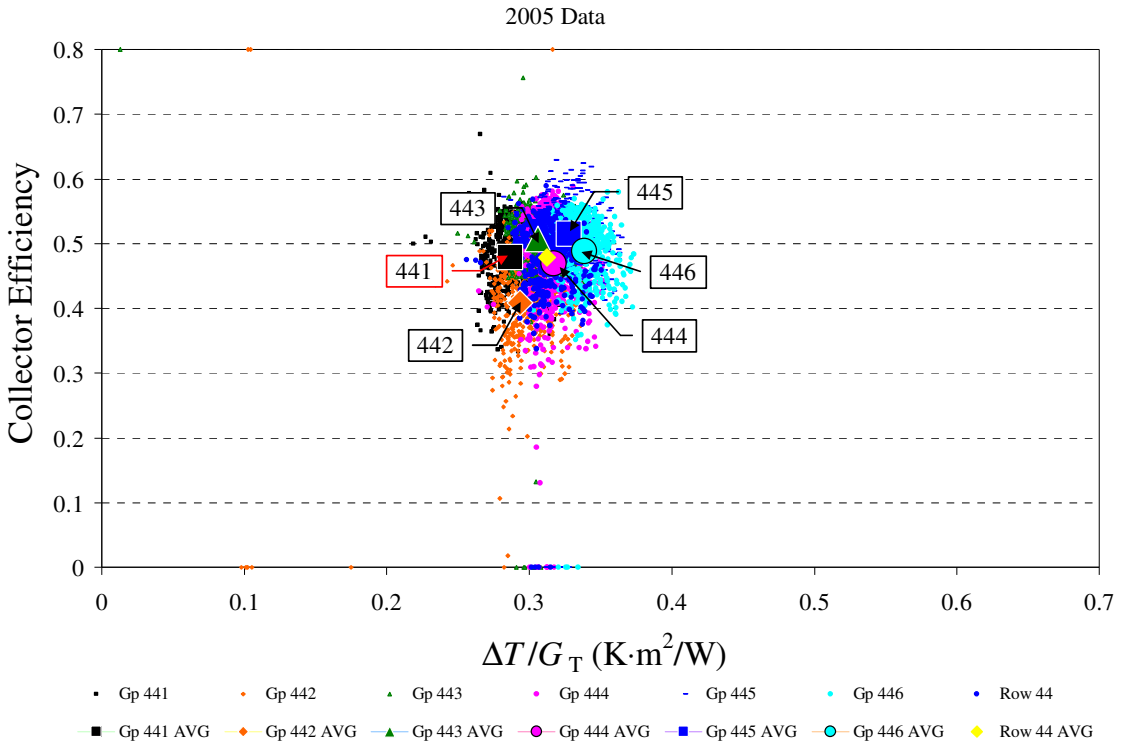

Figure 4.3.1: Efficiency Data for Refurbished Receiver Collector Row

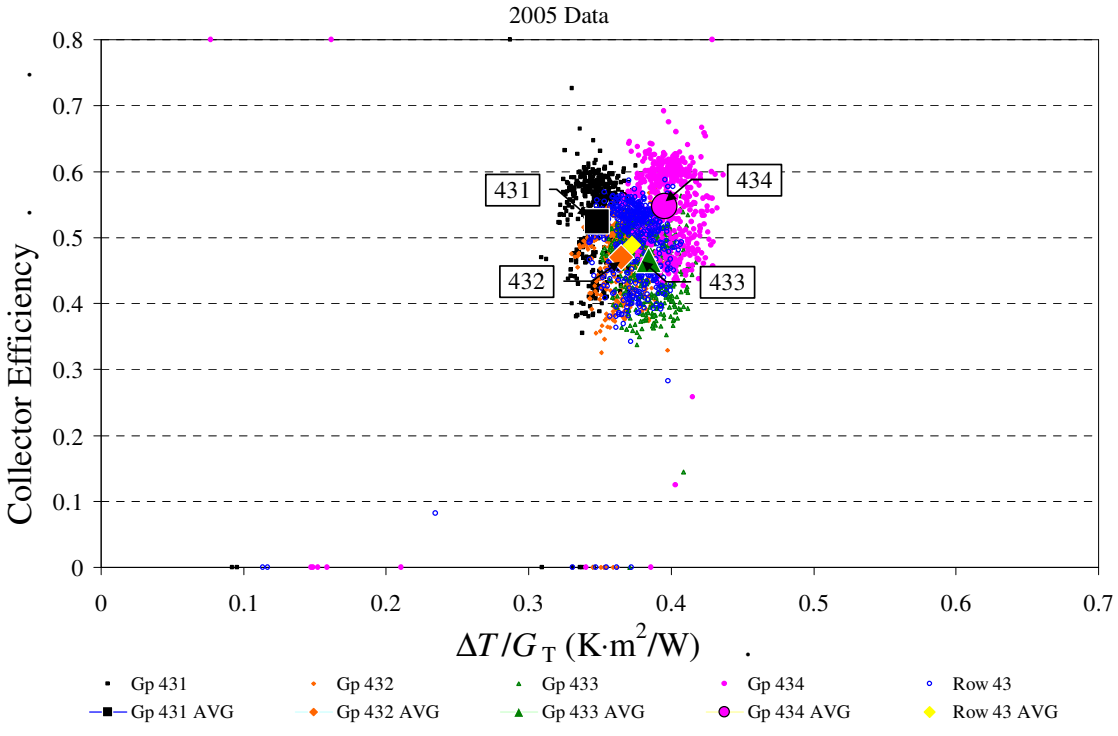

Figure 4.3.2: Efficiency Data for Used HCE Receiver Row

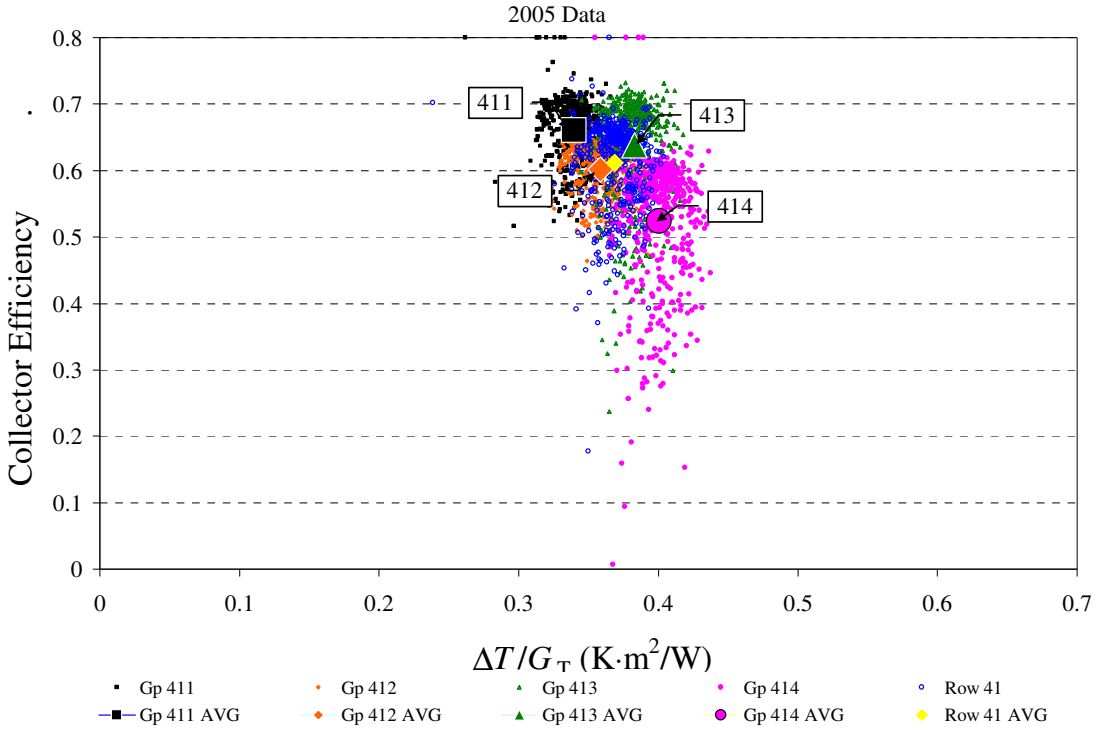

Figure 4.3.3: Efficiency Data for UVAC Collector Row

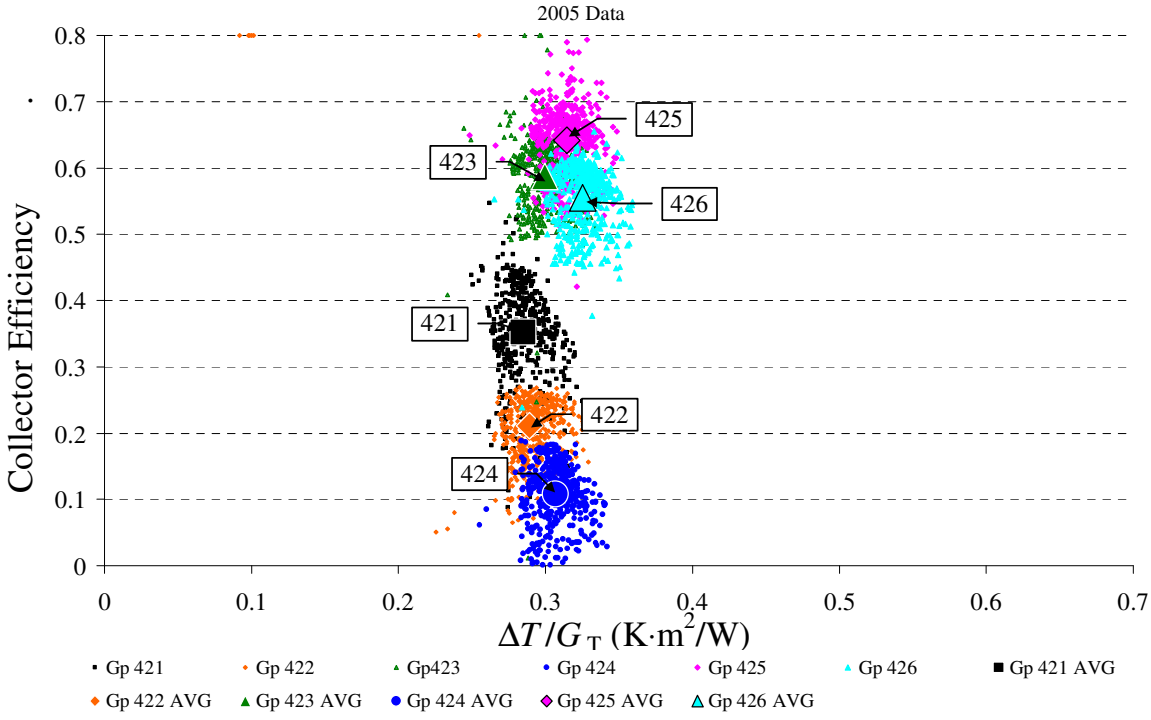

Figure 4.3.4: Efficiency Data for Various Degraded Collectors Row

Table 4.3.1: Average Efficiency Data for Various Collector Types

Collector Type	Average Operating Solar Parameter ($\Delta T/G_T$)	Average Efficiency
UVAC	0.3687	0.612
Used HCE	0.3726	0.488
Refurbished	0.3126	0.479
Broken	0.2850	0.352
Cloudy	0.3070	0.108
Silvery	0.2890	0.211
Lost Vacuum	0.2993	0.588

4.4 COLLECTOR EFFICIENCY MODELS

Collector efficiency models were developed for use in the plant simulation program to calculate the performance of the different collector type arrangements. The purpose of these models is to provide a simple and quick method of predicting collector behavior from available plant performance data and solar angles. The models are based on Equation 2.5.6, in which the efficiency is represented by a combination of optical efficiency and thermal losses. A nominal efficiency equation, based on results from the Sandia rotating platform test presented in Section 2.7, was used as a benchmark for each model.

$$\eta_{\text{COLL,NOM}} = \eta_{\text{OPT,NOM}} - \frac{q''_{\text{LOSS,NOM}}}{G_{\text{T}}} \tag{4.4.1}$$

The nominal optical efficiency, $\eta_{\text{OPT,NOM}}$, is 0.733 corresponding to the case of normal solar incidence and a ΔT, temperature difference between the HTF and ambient air, of zero (See Figure 2.7.1c). The nominal heat loss, $q''_{\text{LOSS,NOM}}$, is represented by a quadratic regression model of Sandia collector heat loss data for the LS-2 HCE with Cermet coating and annulus vacuum. This data is illustrated in Figure 2.7.1b. Two modifying coefficients, one for the optical efficiency and one for the heat loss term, are introduced to adjust the nominal model for each collector type, so that each model fits to its corresponding Test Loop efficiency data. The resulting equation for the efficiency of a given collector type is the following:

$$\eta_{\mathrm{COLL}} = f_{\mathrm{OPT}}\,\eta_{\mathrm{OPT,NOM}} - f_{\mathrm{RHL}}\,\frac{\left(C_1\,\Delta T + C_2\,(\Delta T)^2\right)}{G_{\mathrm{T}}} \qquad (4.4.2)$$

where f_{OPT} and f_{RHL} are the optical efficiency modifier and heat loss modifier, respectively. The constants C_1 and C_2 are the quadratic regression coefficients of the Sandia heat loss data. In this form, the model requires only temperature and irradiance data to calculate efficiency.

Figure 4.4.1 shows a typical plot of measured collector efficiency vs. solar parameter, ΔT/G, with the adjusted efficiency model plotted as a curve through the center of the data. The small range of solar parameter values represented by the field data makes it difficult to analyze collector heat loss affects. The absence of low *ΔT/G* data makes it impossible to extrapolate the data down to a solar parameter of zero, which is the point indicating the collector type's optical efficiency. Since no experimental data is available for the optical efficiency or heat loss of different collector types, there is no basis for definitively choosing the values of each efficiency modifier. A qualitative method could be used, wherein f_{OPT} and f_{HL} are simultaneously chosen so that the model fits with the measured data. However, this method allows for several possible models to fit the data, because an infinite number of modifier pairs exist that would make the given model pass through the center of the plotted data points. This concept is illustrated in Figure 4.4.2.

Figure 4.4.2 implies that the selection of the efficiency modifiers becomes somewhat arbitrary, and ideally the values of these modifiers should be supported by some experimental or statistical evidence. A statistical analysis of the two modifiers was conducted in an attempt to find a pair of values with the most mathematical credibility, and in turn an accurate estimation of the optical efficiency and heat loss behavior for each collector type.

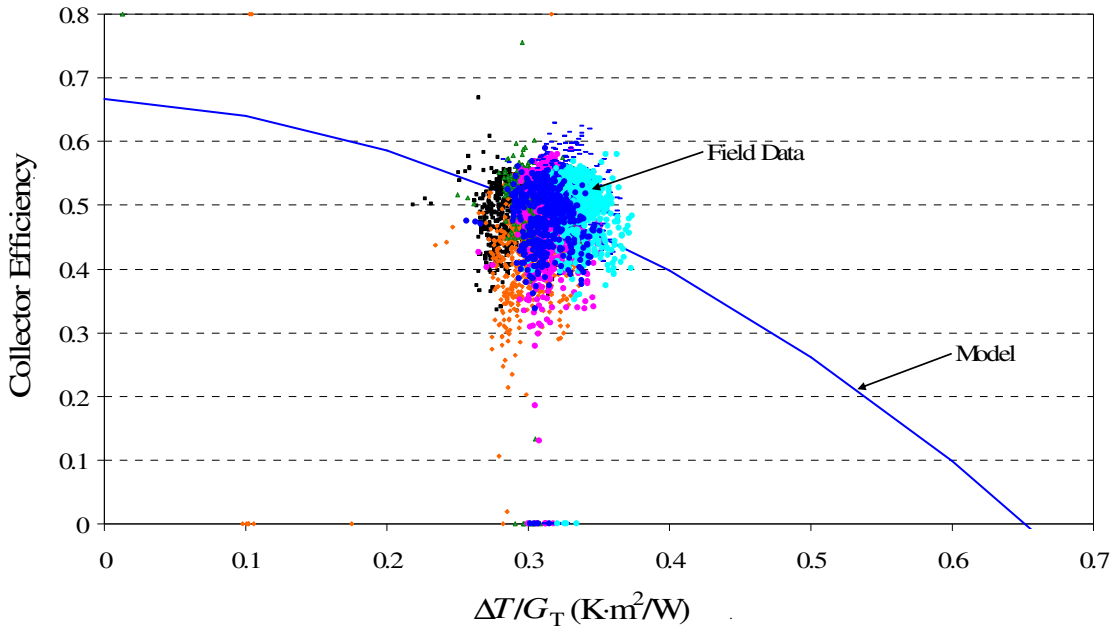

Figure 4.4.1: Typical Plot of Measured Collector Efficiency vs. ΔT/G with Theoretical Model

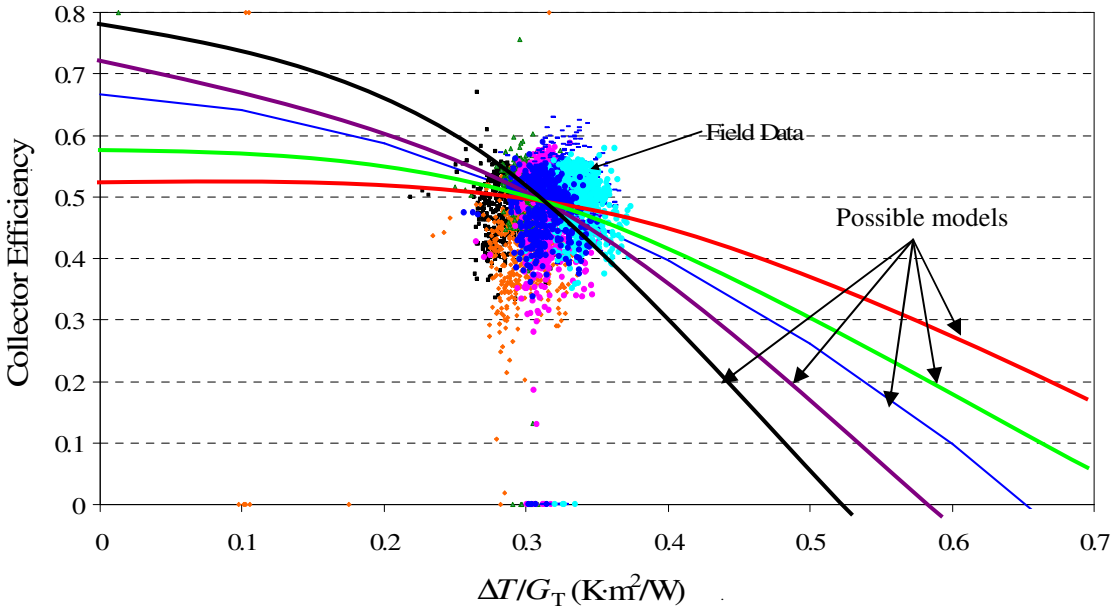

Figure 4.4.2: Illustration of Multiple Possible Efficiency Curves When Qualitatively Selecting Efficiency Model Modifiers

Statistical Analysis of Efficiency Modifiers

By rearranging and grouping terms, Equation 4.4.2 can be expressed as a simple linear equation in the form of y = bx.

$$\underbrace{(f_{\mathrm{OPT}}\eta_{\mathrm{OPT,NOM}} - \eta_{\mathrm{COLL}})}_{\mathbf{y}} = \underbrace{f_{\mathrm{HL}}}_{\mathbf{b}} \underbrace{\left\{\frac{C_1\Delta T + C_2\Delta T^2}{G_{\mathrm{T}}}\right\}}_{\mathbf{x}} \quad \textbf{====>> y = bx} \tag{4.4.3a}$$

The value of the optical efficiency modifier, f_{OPT}, was estimated and the Test Loop Processor was used to calculate the x and y variables, shown above, using measured field data. Ordered pairs of x and y were determined for each hour of data, and the collection of points was plotted as a homogeneous linear regression. The heat loss modifier, f_{HL}, is represented by the slope, b, of the linear y vs. x relationship, as seen in Equation 4.4.3a. This slope is given by the calculated regression coefficient. By this method, the heat loss modifier can be statistically calculated for any value of f_{OPT}.

This process was repeated for a range of f_{OPT} values, and the change in uncertainty, U_{A}, of the statistical results was observed. If a minimum value for U_{A} exists, then the corresponding modifier values could be assumed to be the most statistically credible, and the optical efficiency could be accurately estimated. Figure 4.4.3 shows the results of this analysis for the row of used Luz HCEs, Row 43.

It should be noted that using optical efficiency modifier values below 0.7 yielded heat loss modifiers less than zero. Since this is not a realistic result, only values for f_{OPT} between 0.7 and 1.0 were used in the analysis. The upper limit of 1.0 is due to the fact that the nominal optical efficiency, $\eta_{\mathrm{OPT,NOM}}$, represents the highest possible optical efficiency based on the Sandia test results.

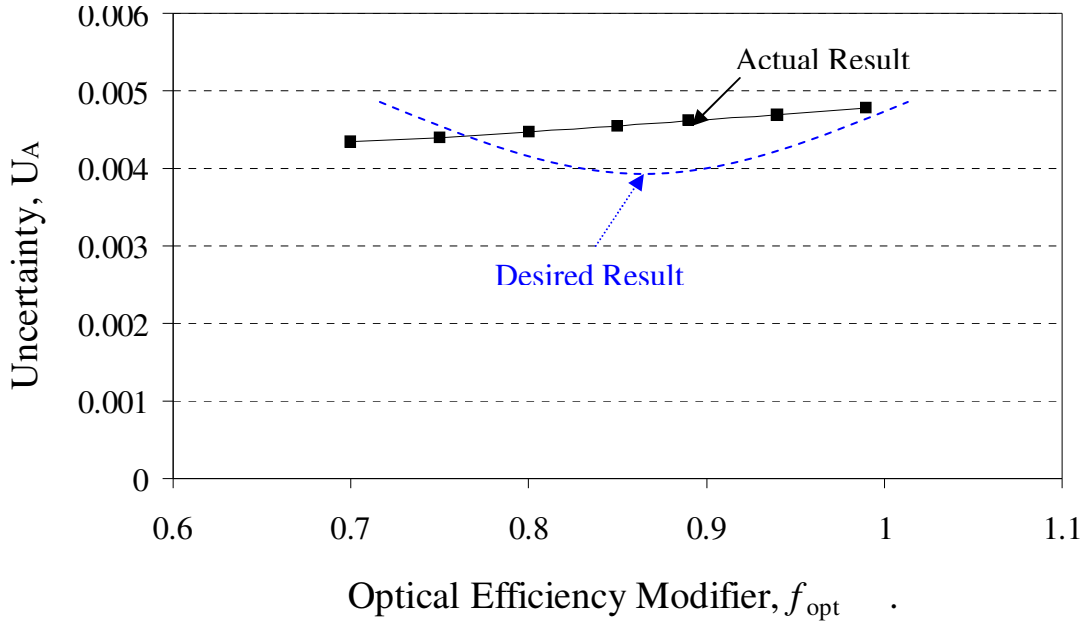

Figure 4.4.3: Results of Statistical Analysis of Efficiency Modifiers for Used HCE Row

As the figure shows, the desired result of this analysis would produce a distinct minimum point in the curve. This point would signify a particular f_{OPT} having less uncertainty than the rest. However, the actual results did not show this behavior; instead, the uncertainty increased with the optical modifier value. This shows that there is no substantial connection between the statistical uncertainty and the values of the modifiers. Therefore, it was concluded that there is no way of predicting the optical efficiency or the model modifiers by statistical methods. Without experimental data, there appears to be no feasible method of determining the optical efficiency of the different collector types. Hence, a qualitative approach was taken, wherein a reasonable value for f_{OPT} was estimated and f_{HL} was subsequently chosen so that the model fit with the measured data. Table 4.4.1 lists the modifiers used for each collector type's efficiency model.

Table 4.4.1: Efficiency Model Modifiers

HCE type	f_{OPT}	f_{HL}
broken	1.00	6.00
cloudy	0.43	3.00
washed	0.50	2.50
lost vacuum	0.98	2.10
refurb	0.91	2.30
used Luz HCE	0.98	1.90
UVAC	1.03	1.50

The relatively large heat loss modifier value for the broken receivers, 6.00, is due to the fact that their absorber tubes are exposed to the ambient air, drastically increasing convection heat loss. The cloudy, washed, lost vacuum, and refurbished receivers all are assigned heat loss modifiers between 2 and 3, because their annular regions have all lost vacuum and heat is transferred more easily through air in the annulus. The modifier for the lost vacuum receivers is lowest among these four types, because its absorber coating is still intact. The refurbished HCE absorbers use a less effective Pyromark coating, which is more emissive than the original coating, so these collectors are assigned a slightly higher heat loss modifier than the lost vacuum types. The deteriorated absorber coating in the cloudy and washed HCE types increases the emissivity of their absorbers, so these types have even higher heat loss modifiers.

The cloudy and washed HCEs have the lowest optical efficiency modifiers, because the collection of broken down coating material on the glass envelope further prevents solar radiation from reaching the absorber tube. The washed HCEs have had some of this particulate material removed, so the optical modifier for these is slightly higher than that of the cloudy HCEs. For the lost vacuum, refurbished, and used Luz HCEs a small degradation of optical efficiency over time was assumed, resulting in modifiers slightly less than one.

Figures 4.4.4 and 4.4.5 show the plotted collector efficiency models for all collector types, with modifiers corresponding to Table 4.4.1.

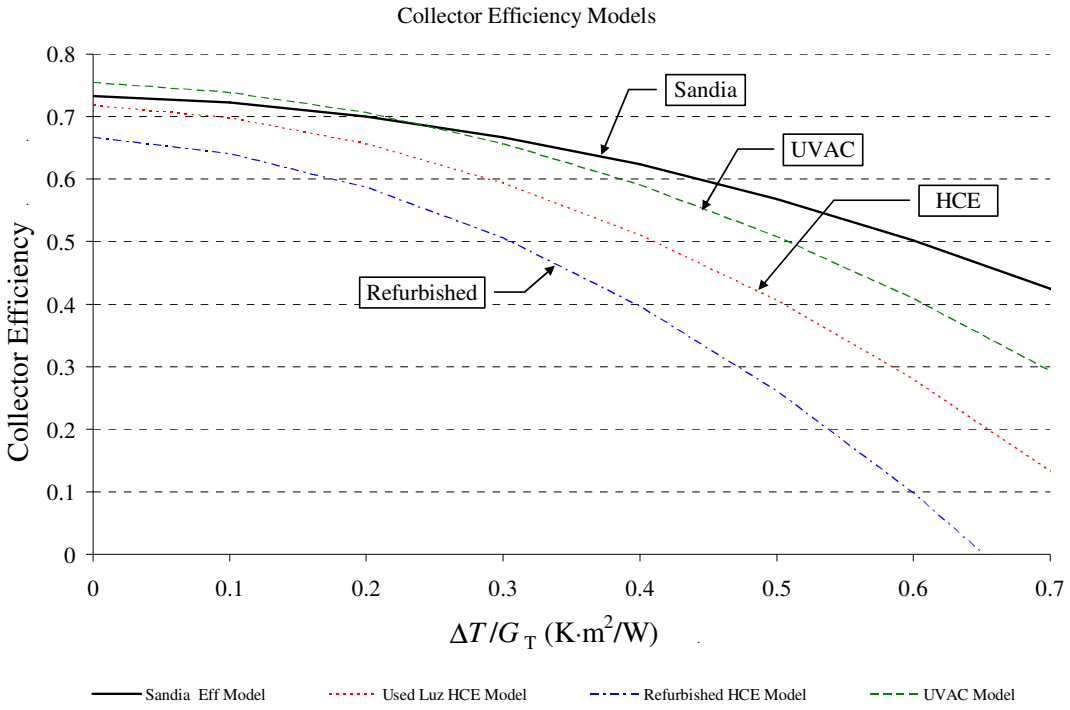

Figure 4.4.4: Collector Efficiency Models (Efficiency vs. Solar Parameter)

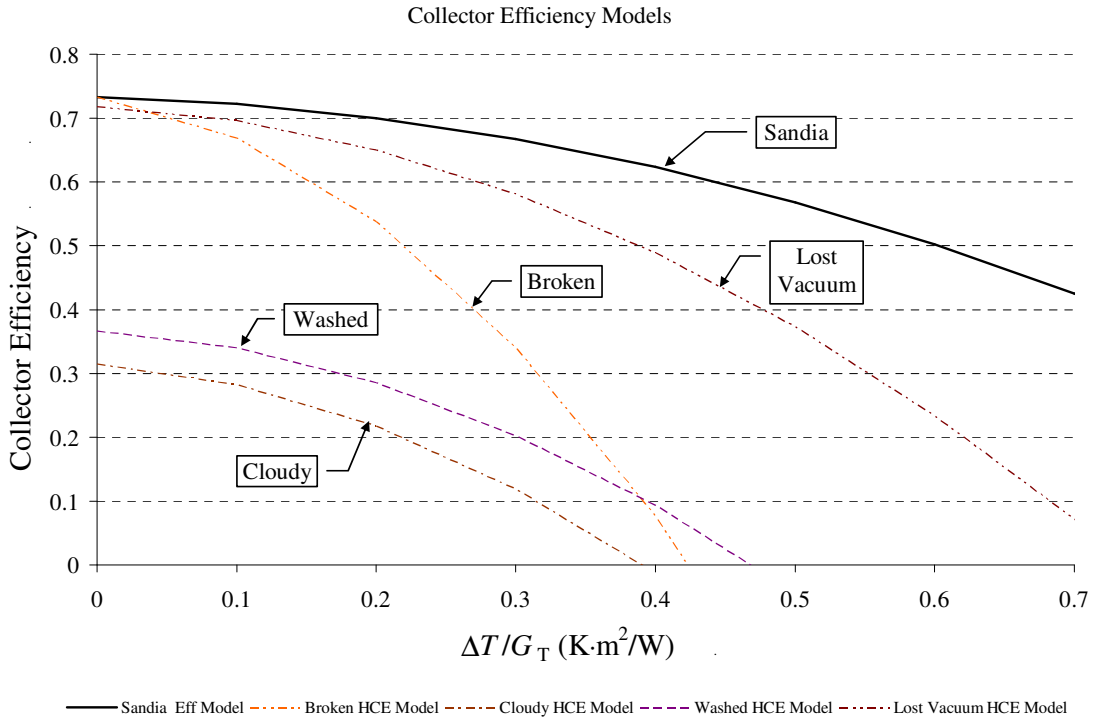

Figure 4.4.5: "Zoo" Collector Efficiency Models (Efficiency vs. Solar Parameter)

CHAPTER 5: THEORETICAL RECEIVER TUBE THERMAL PERFORMANCE MODELING

5.1 OVERVIEW OF THERMAL RESISTANCE MODEL IN ENGINEERING EQUATION SOLVER

The proposed low-cost receiver tube includes a Pyromark-coated absorber pipe and gas-filled annulus, similar to the refurbished HCEs employed at SEGS. To simulate the performance of a low-cost receiver with atmospheric air in the annulus, the Test Loop collector model for refurbished HCEs would suffice; however, none of the current collector models account for varying pressure or different gases within the annulus, so to observe these effects a theoretical approach was taken. A single receiver tube thermal resistance model was developed in Engineering Equation Solver (EES) to calculate the proposed tubes' theoretical thermal behavior under various conditions.

This model uses the one-dimensional thermal circuit analogy, generalized by Equations 2.5.4 and 2.5.5, to determine the resistance to heat loss from the receiver and resistance to heat collection by the heat transfer fluid. It operates on several assumptions in order to simplify the calculations. The following are assumed for all calculations in the model:

1) One dimensional heat transfer between HTF and ambient
2) Uniform temperature distribution over the circumference at a given radius
3) Uniform material/fluid properties at average temperature of a given section
4) Steady state-steady conditions throughout system
5) Uniform temperature across 1m length of receiver

The second assumption is a consequence of the one dimensional analysis. The range of fluid and material properties over the temperature range used in the model is small enough to cause negligible changes in system heat loss, making the third assumption valid. The assumption of steady state conditions in the system is used, because the solar field and plant models typically eliminate data from the early morning and evening when the solar field is starting up

or shutting down. Only data from peak hours when the solar field is fully operational, and has reached steady state conditions, is used. Assuming a uniform temperature across a one meter length of receiver tube yields heat loss rates per meter of pipe, which can then be applied to any number of SCAs to find the total heat loss. This assumption makes the model more robust, and eliminates the need to enter different lengths for collector groups composed of varying numbers of SCAs.

A cross-section of the receiver tube with basic heat flows included is illustrated in Figure 5.1.1.

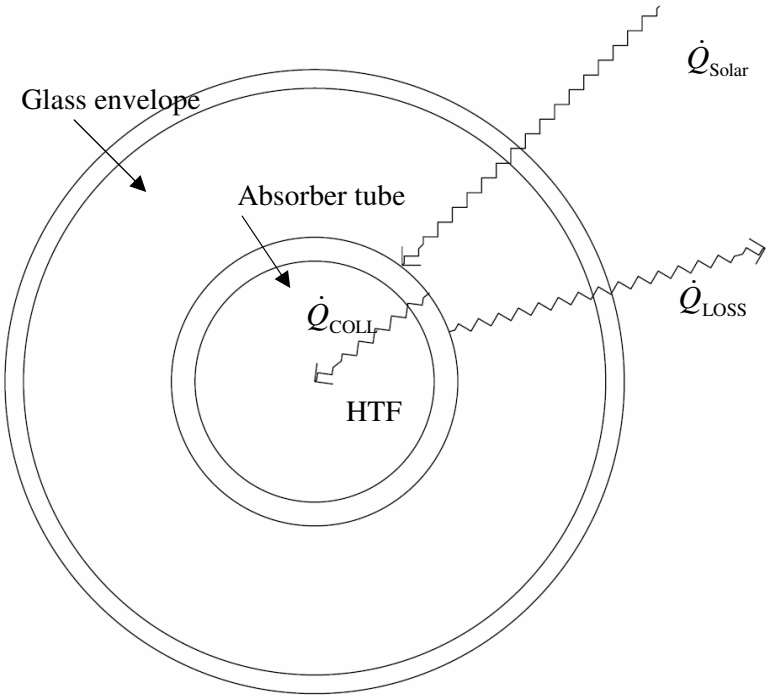

Figure 5.1.1: Cross-Section of Receiver Tube

In the field, incident solar radiation, reflected from the concentrating parabolic trough onto the receiver, is transmitted through the glass envelope and absorbed by the solar selective coating on the absorber pipe. A small amount of this radiation is absorbed by the glass envelope or lost due to optical inefficiencies, but the majority reaches and heats the absorber pipe. The outer absorber surface is thus at the highest temperature in the system. From this

point, heat is either transferred through the absorber wall then collected by the HTF, or it is lost to the ambient air via the annular gap and glass envelope.

The model does not incorporate incident solar radiation on the receiver into its calculations. Instead, it models the heat transfer through the system based solely on temperature differences, and independently of external energy inputs into the system. This approach is consistent with Equation 2.5.5, where the heat loss term is independent of the collected energy term. Using the thermal resistance method, the useful heat collected, $\dot{Q}_U$, and heat lost to the ambient, $\dot{Q}_L$, can be represented by the following equations:

$$\dot{Q}_U = \frac{T_S - T_F}{R_{COLL}} \tag{5.1.1}$$

$$\dot{Q}_L = \frac{T_S - T_A}{R_{LOSS}} \tag{5.1.1b}$$

Here, T_S is the absorber outer surface temperature, T_F is the bulk fluid temperature, and T_A is the ambient air temperature. The resistances to heat collection and heat loss are represented by R_{COLL} and R_{LOSS}, respectively. Substituting these expressions into Equation 2.5.5 yields the following:

$$\dot{Q}_{COLL} = \frac{T_S - T_F}{R_{COLL}} = \eta_o G_{BT} A_{ap} - \frac{T_S - T_A}{R_{LOSS}} \tag{5.1.2}$$

The EES model calculates the two resistances at various system temperatures, so that temperature dependent expressions for each can be developed based on the results. These formulas can then be combined with measured field temperature and irradiance data to predict the proposed collector's performance. The simple thermal network defined by these parameters is shown in Figure 5.1.2.

In order to determine these resistances, the thermal network is further dissected into nodes that separate identifiable modes of heat transfer. The thermal resistance between each node is calculated based on accepted formulas and correlations for the heat transfer mode(s)

present at each specific location. Heat transfer between the heat transfer fluid and absorber pipe occurs by way of forced convection due to the flow of the HTF. Heat transfer through the walls of the absorber pipe and glass envelope is by way of solid conduction. Within the annular space, heat is transferred by a combination of radiation from the absorber pipe coating and natural (free) convection through the annulus gas. Finally, heat loss to the ambient atmosphere occurs via radiation from the outer surface of the glass envelope to the sky and by convection through the ambient air. Ambient convection can be either free or forced depending on the wind conditions. Based on this knowledge, the thermal resistance network for the receiver tube is arranged as illustrated in Figure 5.1.3.

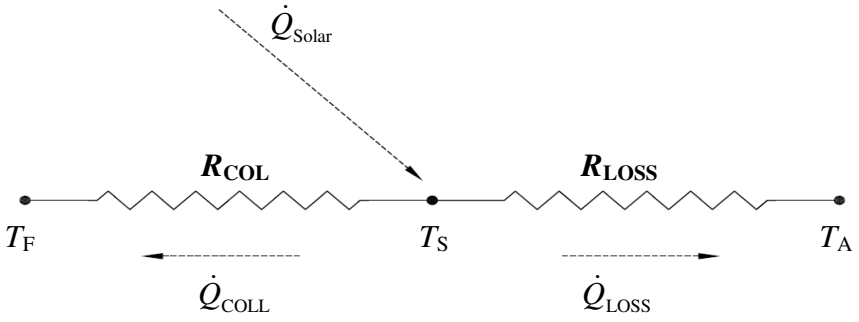

Figure 5.1.2: Simple Resistance Network for Receiver Tube

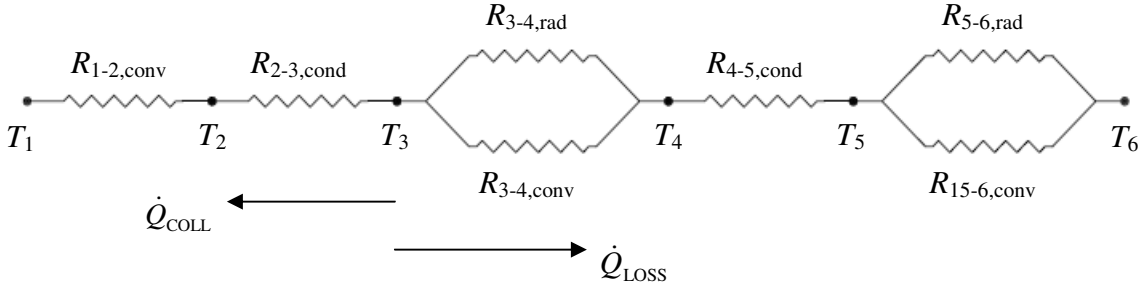

Figure 5.1.3: Complete Thermal Resistance Network for Receiver Tube

Table 5.1.1: Surfaces and Nodes of the Receiver Resistance Network

Node	Surface/Location
1	Bulk of Heat Transfer Fluid (HTF)
2	Inner Absorber Surface
3	Outer Absorber Surface
4	Inner Envelope Surface
5	Outer Envelope Surface
6	Ambient Air

The EES program iteratively calculates all node temperatures and all thermal resistances between nodes based on inputted values of HTF temperature and ambient temperature, the same temperatures measured in the field. The total resistances to heat loss, R_{LOSS}, and heat collection, R_{COLL}, are found by the following combinations of the individual resistances.

$$R_{\text{LOSS}} = R_{3-4,\text{Total}} + R_{4-5,\text{Cond}} + R_{5-6,\text{Total}} \tag{5.1.3a}$$

$$R_{3-4,\text{Total}} = \frac{R_{3-4,\text{Rad}} R_{3-4,\text{Conv}}}{R_{3-4,\text{Rad}} + R_{3-4,\text{Conv}}} \tag{5.1.3b}$$

$$R_{5-6,\text{Total}} = \frac{R_{5-6,\text{Rad}} R_{5-6,\text{Conv}}}{R_{5-6,\text{Rad}} + R_{5-6,\text{Conv}}} \tag{5.1.3c}$$

$$R_{\text{COLL}} = R_{1-2,\text{Conv}} + R_{2-3,\text{Cond}} \tag{5.1.4}$$

Because the model only considers heat transfer after incident solar radiation has been absorbed, it does not account for the heating of the absorber surface by this incident energy, which causes the absorber surface temperature, T_S, to be higher than the fluid temperature. Due to the high conductance of the absorber tube and the HTF, the different between surface and fluid temperatures is small, typically about 5 °C. There is a negligible change in the temperature dependent property values of a given fluid or material when the temperature varies by 5°C. So, for the purpose of determining the thermal resistances in this model, the

surface temperature can be assumed to be equal to the fluid temperature without significantly affecting the results.

When calculating the total useful heat collection of a given receiver, from Equation 5.1.2, the incident energy is accounted for and the true raised absorber surface temperature must be used in this calculation to ensure accuracy. Manipulation of Equation 5.1.2 results in an expression for the true surface temperature.

$$T_S = \left\{ \frac{\eta_{OPT} G_{BT} A_{ap} R_{COLL} R_{LOSS} - R_{COLL} \left(T_F - T_{AMB} \right)}{R_{LOSS} + R_{COLL}} \right\} + T_F \qquad (5.1.5)$$

The surfaces temperature obtained from this equation is used in Equation 5.1.2 when calculating the useful heat collection.

5.2 INPUT VARIABLES OF THE THERMAL RESISTANCE MODEL

Resistance model calculations are based on several user-defined variables that simulate the operating conditions of a receiver in the solar collector field.

Heat Transfer Fluid

Temperature dependent property data for two heat transfer fluids is integrated into the EES model. The two fluids are Therminol-VP1 and Syltherm 800. Therminol-VP1 is the fluid used in SEGS units VIII and IX. Data for Syltherm 800, a silicone heat transfer fluid, is included in the model for comparative purposes. Syltherm was used as the HTF in Sandia's rotating platform collector heat loss tests [Dudley, 1993]. The publication of NREL's EES collector heat loss model also reports calculation results based on Syltherm as the working fluid [Forristal, 2003]. Thus, Syltherm is included in the current model for the sole purpose of comparing the model calculations to SNL test and NREL model results. All calculations

pertaining to the SEGS collector efficiency model are conducted using Therminol-VP1 as the heat transfer fluid.

Property data for Therminol was obtained from a technical bulletin released by Solutia. Fluid properties of Syltherm were found in a specification sheet produced by Dow Corning. Tabulated values were fit to quadratic regression models using the Poly Regression program in VBA to obtain equations for each fluid property based on fluid temperature. The resultant property relationships are listed in Table 5.2.1.

Table 5.2.1: Temperature Dependence of Therminol VP-1 and Syltherm 800 Fluid Properties

Fluid Property	Temperature Dependence (T in ^{o}C)	
	Therminol-VP1 [Solutia, 1999]	**Syltherm 800 [Dow, 2001]**
Density, ρ (kg/m^3)	$\rho = 978.126 - 0.0128T + 0.00174T^2$	$\rho = 912.121 - 0.479T - 0.00108T^2$
Viscosity, μ (kg/m-s)	$\mu = 8.59\text{E}(-4) - 3.15\text{E}(-6)T + 3.42\text{E}(-9)T^2$	$\mu = 0.0033 - 1.5\text{E}(-5)T + 1.84\text{E}(-8)T^2$
Heat Capacity, C_p (kJ/kg-K)	$C_p = 1.877 + 0.000203T + 4.17\text{E}(-6)T^2$	$C_p = 1.574571 + 0.001706T$
Conductivity, k (W/m-K)	$k = 0.137 - 8.00\text{E}(-5)T - 1.80\text{E}(-7)T^2$	$K = 0.139 - 0.00019T$

Absorber pipe coating

To improve the solar irradiation absorption characteristics of collectors, the absorber pipes are coated with a highly absorptive enamel or cermet material. Several different materials have been used in this capacity. The first HCEs developed by Luz International used a flat black chrome enamel that effectively absorbed incident solar radiation but also had relatively high emissivity. The second generation Luz receiver tubes employed a solar selective cermet coating, which had improved absorption and minimal emissive characteristics. The UVACs, developed by Solel, have a coating with absorptive and emissive properties similar to those of the cermet used by Luz. Refurbished collectors are

recoated with Pyromark, a flat black enamel with relatively high emissivity but good absorptive properties and tolerance to high temperatures.

The SEGS unit under consideration employs each of these coating types in different HCEs throughout the solar field. The EES model contains absorption and temperature-dependent emissivity data for each coating type, so that the effect of the coating type on system heat loss can be studied. Expressions for the emissivity of several of these materials based on absorber temperature were developed by NREL. These equations were used in the current model, as were NREL's values for coating absorptance, a constant for each coating type. Table 5.2.2 lists the emittance, absorptance, and envelope transmittance data for each coating used in the program.

Table 5.2.2: Emittance, Absorptance, Envelope Transmittance of Absorber Coatings [Forristal, 2003]

Coating Type	Emittance, ε (Temp-dependent, T in Celsius)	Absorptance, α
Luz Black Chrome	0.0005333 (T + 273.15) – 0.0856	0.94
Luz Cermet	0.000327 (T + 273.15) – 0.065971	0.92
Solel UVAC Cermet (avg)	$(1.91 \times 10^{-7})T^2 + (1.21 \times 10^{-4})T + 7.00 \times 10^{-2}$	0.965
Pyromark [Wade, 1962]	0.78 - 0.95	0.95

Annulus Gas and Pressure

The model allows the user to define the gas that is present in the annular space between the absorber pipe and glass envelope. The gas pressure can also be varied to compare the annulus heat transfer characteristics at hard vacuum, atmospheric pressure (lost vacuum), and any intermediate pressures. The three gases used in calculations are air, hydrogen, and argon. Using air at atmospheric pressure simulates the common case of an HCE that has lost vacuum due to a hole in the glass envelope or a leak at the glass-to-metal

seal of the bellow. Hydrogen is included so that the model can simulate the effects of a hydrogen leak into the annulus. The third gas, argon, is included to observe the insulating effects of an inert gas with low thermal conductivity. Such gases have been proposed as a solution to the hydrogen leak problem, but they may also be employed as a standard component in low temperature HCEs to improve cost effective operation.

Heat Transfer Fluid Mass Flow Rate

The mass flow rate of the heat transfer fluid controls its heat collection capabilities. At higher flow rates, turbulent flow is induced, which increases the heat transfer between the absorber and the fluid. At lower flow rates, the heat conductance is reduced resulting in less collected energy. At SEGS, the HTF flow rate is closely monitored and adjusted to maintain constant solar field inlet and outlet temperatures. The flow rate can be varied in the EES model in order to observe its modulating affect on heat collection.

Ambient wind speed

The wind conditions during operation cause convection heat loss from the receiver tube. The significance of wind speed fluctuation on heat loss varies depending on the elements of the system, such as absorber coating and annulus gas pressure. It is important to observe receiver tube behavior at various wind speeds in order to determine if its fluctuations are significant in comparison to temperature fluctuations. If so, then the resistance models will need to account for wind speed. Annual SEGS data for 2005 and 2006 shows that the average wind speed on site is approximately 7 mph, but periodically reaches speeds around 30 mph. Because of this, the ambient wind speed is designated as a user-defined variable in the model.

Calculations were conducted for various values and combinations of these parameters to determine heat loss characteristics of different receiver types under varying conditions.

5.3 THERMAL RESISTANCE EQUATIONS USED IN CALCULATIONS

Each thermal resistance was determined by using the appropriate correlations for the observed heat transfer mode at the given location.

Convection Between the HTF and the Inner Absorber Wall

The heat loss due to convection between the HTF and absorber wall can be modeled using Newton's Law of Cooling [Incropera, 2002], which is expressed by the following equation:

$$\dot{Q}_{1-2} = h_{\text{conv}} A_2 (T_2 - T_1) \tag{5.3.1}$$

Where h_{conv} represents the local convection heat transfer coefficient in W/m^2-K, and A_2 is the inner surface area of absorber pipe in m^2. The thermal resistance for this mode is then,

$$R_{1-2,\text{Conv}} = \frac{1}{h_{\text{conv}} A_2} \tag{5.3.2}$$

Where,

$$h_{\text{conv}} = \frac{\text{Nu}_\text{D} k_{\text{HTF}}}{D_2}$$

Nu_D = Nusselt Number
k_{HTF} = Thermal Conductivity of Heat Transfer Fluid (W/m-K)
D_2 = Inner diameter of absorber pipe

For laminar flow, assuming fully developed conditions and constant wall heat flux, the Nusselt Number is assumed to be constant and equal to $Nu_\text{D} = 4.36$ [Incropera, 2002]. For

Reynolds Numbers above 3 x 10^5 the absorber wall is assumed to be "smooth", and the following correlation is used to determine the turbulent Nusselt Number [Gnielinski, 1976].

$$\mathrm{Nu_D} = \frac{\left(f/8\right)\left(\mathrm{Re}-1000\right)\mathrm{Pr_1}}{1+12.7\sqrt{f/8}\left(\mathrm{Pr_1}^{2/3}-1\right)}\left(\frac{\mathrm{Pr_1}}{\mathrm{Pr_2}}\right)^{0.11} \tag{5.3.3}$$

$$f = \left(1.82\log_{10}\left(\mathrm{Re}\right)-1.64\right)^{-2} \tag{5.3.4}$$

f = Friction Coefficient
Re = Reynolds Number
$\mathrm{Pr_1}$ = Prandtl Number at bulk temperature of HTF
$\mathrm{Pr_2}$ = Prandtl Number at inner absorber surface temperature

Gnielinski's equation gives validity over the largest range of Prandtl and Reynolds Numbers. It is considered accurate for Prandtl numbers between 0.5 and 2000, and for Reynolds Numbers between 3000 and 5 x 10^6. This eliminates the need for added conditional statements and allows one equation to cover the entire range of turbulent flow conditions that the program will model.

Conduction Through Absorber Wall

Conduction through the absorber wall is modeled using the method presented by Incropera and DeWitt, which combines the temperature distribution in the radial direction with Fourier's Law of conduction [Incropera, 2002]. The thermal resistance associated with this approach is a modified version of the plane wall conduction resistance involving the logarithmic ratio of the inner and outer pipe radii.

$$R_{2-3,\mathrm{Cond}} = \frac{\ln\left(\frac{r_2}{r_1}\right)}{2\pi L k_{\mathrm{abs}}} \tag{5.3.5}$$

r_2 = outer radius of absorber pipe (m)

r_i = inner radius of absorber pipe (m)
L = axial length of receiver tube (m)
k_{abs} = thermal conductivity of absorber pipe (W/m-K)

Absorber pipe conduction is evaluated for AISI 316 stainless steel, but EES has property libraries for several different grades of stainless steel that could also be used.

Radiation Between Outer Absorber Surface and Inner Envelope Surface

Incropera and DeWitt present the standard result for the radiation heat transfer between two long concentric cylinders, where the view factor is equal to 1. [Incropera, 2002]. Algebraic manipulation of this equation gives the heat loss as a function of a temperature change and a second complex expression, from which a thermal radiation resistance can be deduced. See for example, Jeter [1979]. The results of this manipulation are employed in the EES model to calculate the radiation resistance in the annulus.

$$R_{3-4,\mathrm{Rad}} = \frac{1}{H_R A_3} \tag{5.3.6}$$

$$H_R = \frac{\sigma \varepsilon_{abs} \varepsilon_{glass} \left(T_3^{\,2} + T_4^{\,2}\right)\left(T_3 + T_4\right)}{\varepsilon_{glass} + \varepsilon_{abs} \dfrac{\left(1 - \varepsilon_{glass}\right) r_3}{r_4}} \tag{5.3.7}$$

H_R = coefficient of radiation heat transfer (W/m^2-K)
A_3 = outer surface area of absorber pipe (m^2)
σ = Stefan-Boltzmann constant (= 5.67 x 10^{-8} W/m^2-K^4)
ε_{abs} = emissivity of absorber coating
ε_{glass} = emissivity of glass envelope (Pyrex)
T_3 = outer absorber surface temperature (°C)
T_4 = inner glass envelope surface temperature (°C)
r_3 = outer absorber radius (m)
r_4 = inner glass envelope radius (m)

The emissivity of the Pyrex glass is kept constant at 0.86, because its temperature dependence over the range of field operating temperatures is negligible.

Depending on the pressure in the annular space between the absorber pipe and glass envelope, radiation can have more or less of an effect on the total heat transfer through the system. At high annulus gas pressures, free convection causes significant thermal losses; however, as pressure decreases and approaches vacuum, losses to free convection also decrease. The absorptivity and emissivity of the absorber coating are not dependent on pressure, only temperature. Thus, radiation heat loss will not be affected by pressure changes and will have more influence on system heat loss with the annulus at vacuum, when convective effects are minimized.

Convection Between Outer Absorber and Inner Envelope Surface

The presence of a gas within the annulus results in heat transfer across the annular gap by way of convection. The convective heat loss takes on one of two forms depending on the pressure of the gas. At higher pressures heat is transferred through the gas by free convection. At lower pressures convective heat loss through the annulus is minimal due to a lack of moving fluid, but a small amount of heat is transferred through the annulus gas by way of free molecular conduction.

The thermal resistance from convection in the annulus is determined using the correlation for concentric cylinders [Raithby & Hollands, 1975].

$$R_{3-4,\text{FreeConv}} = \frac{\ln\left(\frac{D_4}{D_3}\right)}{2\pi L k_{\text{eff}}} \tag{5.3.8}$$

D_4 = inner glass envelope diameter (m)
D_3 = outer absorber pipe diameter (m)
L = length of receiver tube (m)

The effective conductivity, k_{eff}, is defined as "the thermal conductivity that a stationary fluid should have to transfer the same amount of heat as the moving fluid" [Incropera, 2002]. In the case of free convection, the effective conductivity is calculated by the following equation:

$$k_{\text{eff}} = 0.386 k_{34} \left(\frac{\text{Pr}_{34}\, \text{Ra}_{\text{C}}}{0.861 + \text{Pr}_{34}} \right)^{1/4} \tag{5.3.9}$$

k_{34} = thermal conductivity of annulus gas at T_{34} (W/m-K)
Pr_{34} = Prandtl Number of annulus gas at
Ra_{C} = effective Rayleigh Number

The effective Rayleigh number, Ra_{C}, is a function of the standard Rayleigh number for a fluid flowing past a single cylinder with characteristic length equal to the difference of the inner and outer annulus radii, $R_4 - R_3$.

$$\text{Ra}_{\text{C}} = \frac{\left[\ln(D_4/D_3)\right]^4}{L_{\text{C}}{}^3 \left(D_3{}^{-3/5} + D_4{}^{-3/5} \right)^5} \text{Ra}_{\text{L}} \tag{5.3.10}$$

$$\text{Ra}_{\text{L}} = \frac{g \beta_{34} (T_3 - T_4) \text{Pr}_{34}\, L_{\text{C}}{}^3}{\nu_{34}{}^2} \tag{5.3.11}$$

Ra_{L} = standard Rayleigh Number for characteristic length, L
L_C = characteristic length of concentric cylinder geometry ($R_4 - R_3$)
g = gravitational acceleration
β_{34} = volumetric expansion coefficient (= 1/T for ideal gases)
ν_{34} = kinematic viscosity of annulus gas at T_{34} (m^2/s)

For the case of molecular conduction, the resistance is determined by Equation 5.3.8 using the effective thermal conductivity defined by Equation 5.3.12, presented below [Ratzel, 1977].

$$k_{\text{eff}} = \frac{k_{\text{STD}}}{r_3 \ln(r_4/r_3) + b\lambda\{(r_3/r_4)+1\}} \tag{5.3.12}$$

Here, k_{STD} is the thermal conductivity of the annulus gas at standard atmospheric conditions. λ is the mean free path of the gas in cm, and it is determined by [Odeh, 1998],

$$\lambda = 2.331\text{x}10^{-10}\frac{T_{\text{m}}}{P\delta^2} \tag{5.3.13}$$

where T_{m} the mean absorber-gas temperature in Kelvin, P is is the annulus pressure in Torr, and δ is the molecular diameter of the annulus gas in cm. The variable *b* in Equation 5.3.12 represents the following expression [Odeh, 1998]:

$$b = \frac{2-c}{c}\left\{\frac{9\gamma-5}{2(\gamma+1)}\right\} \tag{5.3.14}$$

C = Accommodation coefficient for surface-gas interaction
γ = Specific heat ratio of annulus gas at mean temperature

The accommodation coefficient is assumed to be equal to one unless the surfaces are extremely clean [Dudley, 1993]. This assumption is made for all resistance calculations performed here. The model computes the resistances from both free convection and molecular conduction and assigns the lower value as the annulus convection resistance. The lower of the two resistances is used, because this form will result in greater heat loss. Based on model calculations, the transition between annulus convection modes occurs at a pressure of about 70 torr.

Conduction Between Inner and Outer Glass Envelope Surfaces

Heat lost through the wall of the glass envelope is by way of conduction. It follows the same law as that of conduction across the absorber pipe.

$$R_{4-5,\text{Cond}} = \frac{\ln\left(\frac{r_5}{r_4}\right)}{2\pi L k_{\text{glass}}} \tag{5.3.15}$$

r_5 = inner radius of glass envelope (m)
r_4 = outer radius of glass envelope(m)
L = axial length of receiver tube (m)
k_{glass} = thermal conductivity of glass envelope (W/m-K)

The conductivity of the Pyrex glass is kept constant at 1.4 W/m-K, because its temperature dependence over the range of field operating temperatures is negligible.

Radiation Between Glass Envelope and Ambient Environment

Heat loss from the glass envelope surface by way of radiation is calculated using the basic equation for radiation heat transfer from a gray surface to its "surroundings". In this case, the receivers are surrounded by the sky. The thermal resistance to ambient radiation heat loss is thus calculated by the following equation [Incropera, 2002]:

$$R_{5-6,\text{Rad}} = \frac{1}{H_{\text{R}} A_5} \tag{5.3.16}$$

$$H_{\text{R}} = \varepsilon_{\text{glass}} \sigma \left(T_5 + T_{\text{sky}}\right)\left(T_5^2 + T_{\text{sky}}^2\right) \tag{5.3.17}$$

H_{R} = coefficient of radiation heat transfer (W/m^2-K)
A_5 = outer surface area of glass envelope (m^2)
σ = Stefan-Boltzmann constant (= 5.67 x 10^{-8} W/m^2-K^4)
$\varepsilon_{\text{glass}}$ = emissivity of glass envelope (Pyrex)
T_5 = outer glass envelope temperature (°C)
T_{sky} = effective sky temperature (°C)

The effective sky temperature, T_{sky}, is slightly lower than the local ambient air temperature, T_6. It can vary due to atmospheric conditions such as wind and cloud cover, and is hence

difficult to generalize for the sake of modeling. Several equations have been developed that relate the sky temperature to other measurable parameters, such as local ambient temperature or dew point temperature; however, these relationships typically assume ideal clear sky conditions, which is often not the case in practical applications. In addition, they assume a flat surface completely surrounded by sky cover, but the receiver tube is surrounded by the parabolic trough reflector in some areas. The presence of the reflecting mirrors should serve to increase the effective sky temperature used for calculations. Although there are many variables affecting this parameter, Duffie and Beckman explain that the variation between sky temperature and local air temperature will not significantly alter the thermal radiation or heat loss from a surface [Duffie, 1980]. Previous receiver heat loss models have approximated the sky temperature to be 8°C below the local ambient air temperature to simplify calculations, and the results were still in agreement with measured performance data [Forristal, 2003]. Therefore, for calculations in this model, the receiver is assumed to be surrounded by sky at 8 °C below the ambient air temperature. The radiation resistance is referenced to the ambient air temperature so that it is compatible with the ambient convection resistance [Duffie, 1980].

Convection Between Outer Glass Envelope and Ambient Environment

The presence of air around the glass envelope causes heat losses in the form of either free convection or forced convection. Free convection occurs when the ambient air is stagnant, or its velocity is ≈ 0, and forced convection takes over when wind moves the air across the tube. The ratio of Grashof number to the square of the Reynolds number, Gr/Re_D^2, is used to determine the mode of convection that is dominant. At a ratio of less than about 0.99, forced convection is dominant and free convection effects can be neglected. At a ratio greater than approximately 1.01, free convection is dominant, and at a ratio of approximately 1, both modes occur simultaneously [Incropera, 2002]. For free convection calculations, the correlation for free convection from a long horizontal cylinder is employed to determine the average Nusselt number [Churchill, 1975].

$$\mathrm{Nu_D} = \left\{ 0.60 + \frac{0.387 \mathrm{Ra_D^{1/6}}}{\left[1 + \left(0.559/\mathrm{Pr_{5-6}}\right)^{9/16}\right]^{8/27}} \right\}^2 \tag{5.3.18}$$

$$\mathrm{Ra_D} = \frac{g \beta_{5-6} (T_5 - T_6) \mathrm{Pr_{5-6}} D_5^{\,3}}{\nu_{5-6}^{\,2}} \tag{5.3.19}$$

$\mathrm{Ra_D}$ = Rayleigh number
$\mathrm{Pr_{5-6}}$ = Prandtl number of air at the glass envelope-air film temperature
g = gravitational acceleration (9.8 m/s^2)
β_{5-6} = thermal expansion coefficient of air at the glass envelope-air film temperature (1/K)
T_5 = glass envelope temperature (°C)
T_6 = local ambient air temperature (°C)
D_5 = glass envelope outer diameter (m)
ν_{5-6} = kinematic viscosity of air at the glass envelope-air film temperature (m^2/s)

Churchill and Chu's correlation is valid over the widest range of Rayleigh numbers $\left(\mathrm{Ra_D} \le 10^{12}\right)$, eliminating the need for multiple conditional calculations in the model.

When wind speed is above the threshold value, the Nusselt number is calculated using Hilpert's correlation for convection on a horizontal cylinder in cross flow [Hilpert, 1933].

$$\mathrm{Nu_D} = C\, \mathrm{Re}_D^{m}\, \mathrm{Pr}_{5-6}^{1/3} \tag{5.3.20}$$

The constants C and m vary based on the value of the Reynolds number, $\mathrm{Re_D}$. Table 5.3.1 lists the values of these constants for given ranges of Reynolds number values.

Table 5.3.1: Constants of Equation 5.3.20 Based on Reynolds Number [Incropera, 2002]

Re_D	C	m
0.4 – 4	0.989	0.330
4 – 40	0.911	0.385
40 – 4000	0.683	0.466
4000 – 40,000	0.193	0.618
40,000 – 400,000	0.027	0.805

A correlation for cross flow convection, or flow running perpendicular to the axial direction of the receiver tube, yields the highest possible heat loss values. Air flow at the SEGS solar field is not consistently in a direction perpendicular to the collectors; flow patterns are likely inconsistent and unpredictable, and move at varying orientations (from cross flow to parallel flow) to the receiver tubes. Assuming constant cross flow will overestimate the convection heat losses on the outer glass surface, but the resistance model still produces heat loss results lower than those measured by Sandia due to the neglecting of certain heat loss paths. These sources and model adjustments will be discussed in the next section. The overestimation of ambient convection losses is therefore insignificant, and the cross flow correlation provides sufficient accuracy.

5.4 PRELIMINARY MODEL CALCULATIONS AND PARAMETER DEPENDENCE

Preliminary resistance calculations were performed for varying combinations of the aforementioned user-defined variables. These preliminary calculations were designed to show the proposed collectors' behavior under different operating conditions and to observe the dependence of system heat transfer on different parameters. Separate calculations were conducted for a range in values of each specific parameter while the others were held constant. Since proposed collectors with different annulus pressures are to be tested in plant simulations, each parameter was evaluated at four different annulus pressures. The constant

control values for each user-controlled variable are listed in Table 5.4.1. All of the preliminary calculations used Pyromark as the absorber coating and Therminol-VP1 as the heat transfer fluid. The properties of Pyromark and Therminol-VP1 are presented in Section 5.2. Figures 5.4.1 – 5.4.5 illustrate plots of the parameter dependence of the calculated resistance to heat loss, R_{LOSS}. Similar plots for the resistance to heat collection, R_{COLL}, are shown in Figures 3.17 and 3.18.

Based on model calculations, the transition from free convection to molecular conduction heat loss occurs between 60 and 70 torr. This observation does not fully agree with NREL's observation that the transition occurs closer to 1 torr; however, in comparing a Heat Loss vs. Pressure plot from resistance model calculations to a similar plot presented by NREL, the heat loss behavior appears to agree even though the transition occurs at different pressures. The variance in transition pressure may result from near equal thermal resistance from free convection and molecular conduction in the range of 1 torr to approximately 70 torr. As Figure 5.4.1 shows, the relationship between heat loss and pressure is difficult to express by a single simple function. Such evaluation is unnecessary since the proposed receiver types will be tested at a pre-determined pressure. Simulation resistance models will be calculated at different pressures separately since annulus pressure is not a measurable parameter in the field.

Table 5.4.1: Parameter Constant Control Values for Preliminary Resistance Calculations

Parameter	Control Value
Heat Transfer Fluid Temperature, T_{HTF}	350 °C
Ambient Temperature, T_{AMB}	25 °C
Annulus Pressure	760 torr , 400 torr, 100 torr, 0.0001 torr
Wind Speed	5 m/s
HTF Mass Flow Rate, $\dot{m}_{HTF}$	6 kg/s

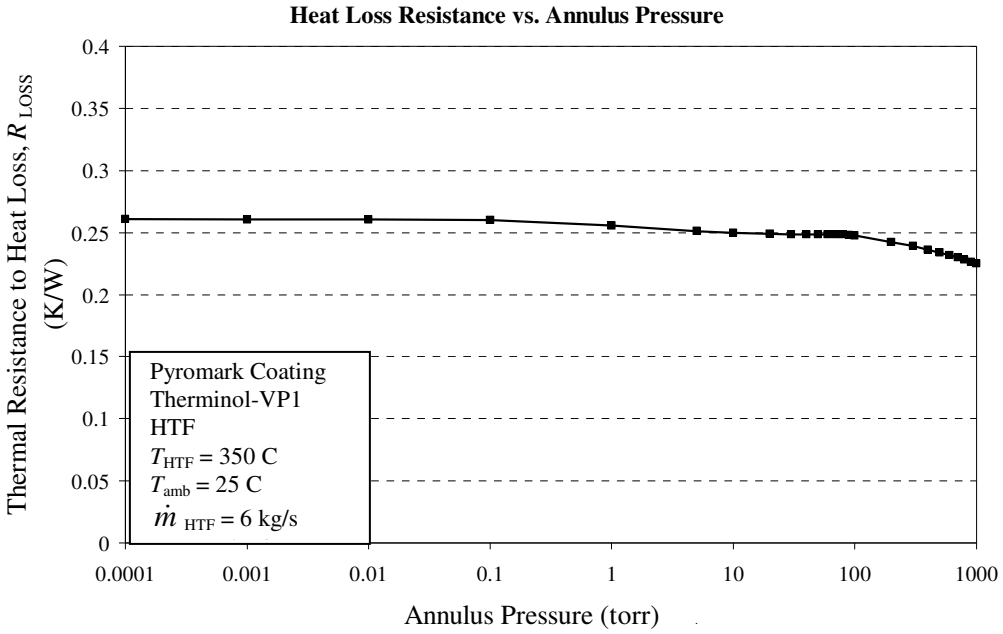

Figure 5.4.1: Heat Loss Resistance Pressure Dependence Plot

With a highly emissive coating like Pyromark on the absorber pipe, the benefit of a vacuum sealed annulus is small. As Figure 5.4.1 illustrates, the heat loss resistance at vacuum is only 15.8 % greater than the resistance with atmospheric air in the annulus. Figure 5.4.1b compares the pressure dependent heat loss resistance of the Pyromark-coated receiver to that of a receiver with solar-selective absorber coating. Using the solar-selective coating, the heat loss resistance improves by over 150% with the annulus held at vacuum. The abrupt change in shape of the solar-selective curve at approximately 70 torr is due to the immediate shift from free convection to molecular conduction in the model. In reality, there is a transitional range of pressures where both forms of heat transfer are significant simultaneously. Since the model does not account for this gradual transition, the result is a sharp change in shape, where in real life the variation would be smoother.

The large discrepancy in pressure dependent performance of the two receiver types shows that heat loss by radiation is much more significant than by convection in the annulus with a highly emissive coating. In contrast, the solar-selective coating appears to minimize radiation effects to the point where free convection dictates the amount of heat lost through the annulus. Table 5.4.2 gives further evidence to this claim. It shows the significant

calculated thermal resistances and temperatures for the low efficiency and high efficiency receivers at both low and high pressures. Each of these modeled sets of conditions assumed a HTF temperature of 330 °C, ambient temperature of 25 °C, HTF flow rate of 6 kg/s, and wind speed of 5 m/s. The "high pressure" modeled is 760 torr, and the "low pressure" is 1 torr.

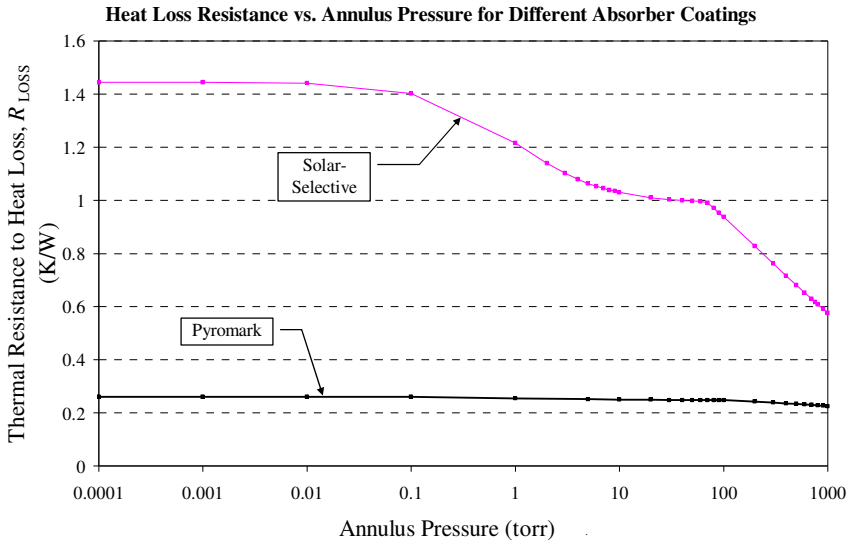

Figure 5.4.1b: Heat Loss Resistance Pressure Dependence for Different Absorber Coatings

Table 5.4.2: Comparison of Resistance Model Results at High/Low Annulus Pressures

Receiver Conditions	HTF Temp	$R_{3\text{-}4,\ Conv}$ (K/W/m)	$R_{3\text{-}4,\ Rad}$ (K/W/m)	Glass Env Temp	$R_{5\text{-}6,\ Conv}$ (K/W/m)	$R_{5\text{-}6,\ Rad}$ (K/W/m)
Solar Selective High Pressure	330 °C	0.8354	1.41	69.9 °C	0.1097	0.4441
Solar Selective Low Pressure	330 °C	6.584	1.497	46.43 °C	0.1087	0.4977
High ε Coating High Pressure	330 °C	0.9112	0.1994	129.7 °C	0.1120	0.3358
High ε Coating Low Pressure	330 °C	6.884	0.2061	117.25 °C	0.1115	0.3555

For all cases, the resistance to ambient convection is approximately 0.11 K/W/m. The resistance to ambient radiation with the solar selective coating is 0.4441 K/W/m at high annulus pressure, and nearly the same, 0.4977K/W/m, as low annulus pressure. With the high emissivity coating, the resistance to ambient radiation is approximately 0.34 K/W/m for both pressure cases. The increase in annulus convection resistance from high pressure to low pressure is virtually the same for the two coatings; it increases from 0.8354 to 6.584 W/K/m for the solar selective coating, and from 0.9112 to 6.884 K/W/m for the high emissivity coating. The resistance to radiation from the absorber surface changes drastically between the solar selective and high emissivity coatings. The average value for the solar selective coating is 1.45 K/W/m, while the average value for the high emissivity coating is 0.203 K/W/m.

While the resistances to annulus convection, ambient radiation, and ambient convection are relatively consistent between each case, the resistance to annulus radiation from the absorber changes drastically. The values for the high emissivity coating cases are nearly 10 times lower than those for the solar selective coating cases. In addition, $R_{3\text{-}4,\,\mathrm{Rad}}$ is greater than $R_{3\text{-}4,\,\mathrm{Conv}}$ using the solar selective coating, meaning convection effects will dominate the heat loss. Using the high emissivity coating $R_{3\text{-}4,\,\mathrm{Rad}}$ is so much lower than $R_{3\text{-}4,\,\mathrm{Conv}}$ that the increase in convection resistance at lower pressures causes little overall change. These results explain the discrepancy in pressure dependence of the two receiver types illustrated in Figure 5.4.1b.

The dependence of heat loss resistance on fluid temperature is plotted in Figure 5.4.2. According to the Figure, fluid temperature has the largest impact on the receiver's resistance to heat loss. At atmospheric pressure in the annulus, the resistance drops approximately 25 % from field inlet temperature ($\approx$ 270 °C) to field outlet temperature ($\approx$ 380 °C). The resistance with a vacuum annulus drops about 30% over the range of field operating temperatures. The difference in resistance between the annulus at vacuum and at atmospheric pressure is more significant at low temperatures than at high temperatures. This is because at low temperatures radiation from the absorber surface is reduced, creating more of a dependence on convection and pressure.

At low velocities, variation in wind speed can cause substantial changes in heat loss behavior, lowering heat loss resistance by nearly 25% from 0 to 10 m/s. At higher speeds, above 10 m/s, the effect of increasing wind speed becomes negligible, as is evidenced by the near horizontal section of the curve in Figure 5.4.3. The change in shape of the curve as the wind speed approaches zero is caused by the transition from forced to free convection. The average measured wind speed in the test loop data is only 3.18 m/s with a standard deviation of about 3 m/s, meaning wind velocity is generally in the range where its variance will influence the overall thermal behavior of the receivers.

As Figures 5.4.4 and 5.4.5 illustrate, variation in ambient temperature and HTF flow rate have little influence on the thermal resistance to heat loss. It makes sense that flow rate does not affect ambient heat loss, which occurs between the absorber surface and the ambient air. Flow rate variations should, however, have a large impact on heat collected by the fluid. This relationship is examined in Figure 5.4.7. Although variation in ambient air temperature does not cause significant changes in the heat loss behavior of the receiver, its low values create the large temperature difference with respect to the absorber surface that drives heat transfer away from the surface. Therefore, the ambient temperature is still incorporated into the resistance regression models, despite the weak influence of its fluctuations.

Figures 5.4.6 and 5.4.7 show calculation results for the resistance to heat collection, R_{COLL}. Since heat collection occurs between the absorber and the HTF, conditions occurring outside of the absorber pipe will have negligible affect on heat collection. The only parameters whose variation will influence heat collection are hence the HTF temperature and flow rate. The relationship between heat collection resistance and fluid temperature is nearly linear, but a quadratic regression is likely necessary to ensure accurate modeling of the effects of fluid temperature changes. Figure 5.4.7 shows a very large dependence on the fluid flow rate; however, in the field the flow rate is monitored and adjusted to maintain a constant temperature difference between the solar field inlet and outlet. Therefore, the temperature dependence of the heat collection is the most important factor to consider for regression modeling.

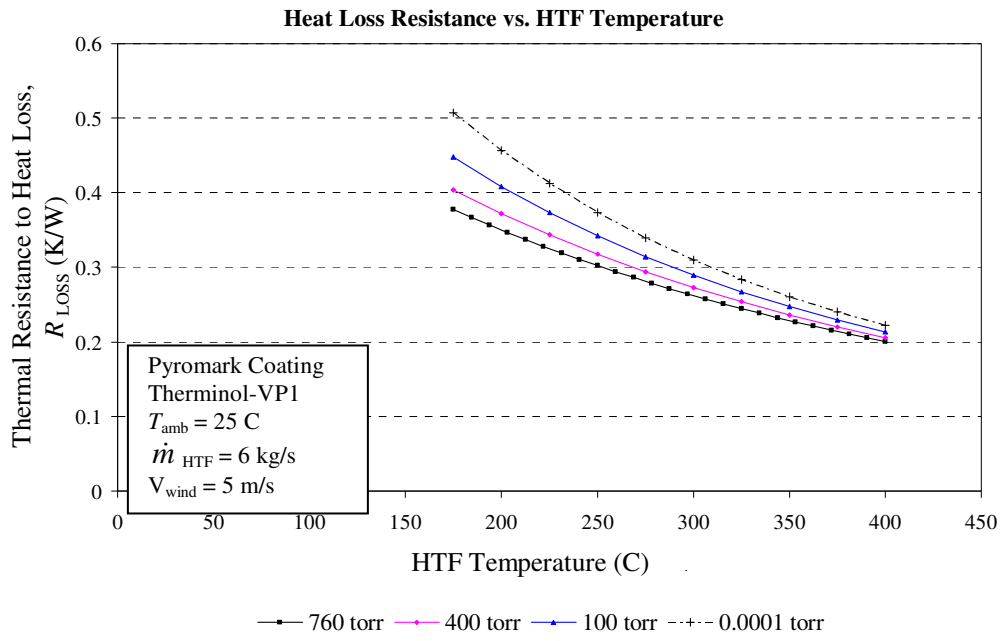

Figure 5.4.2: Heat Loss Resistance HTF Temperature Dependence Plot

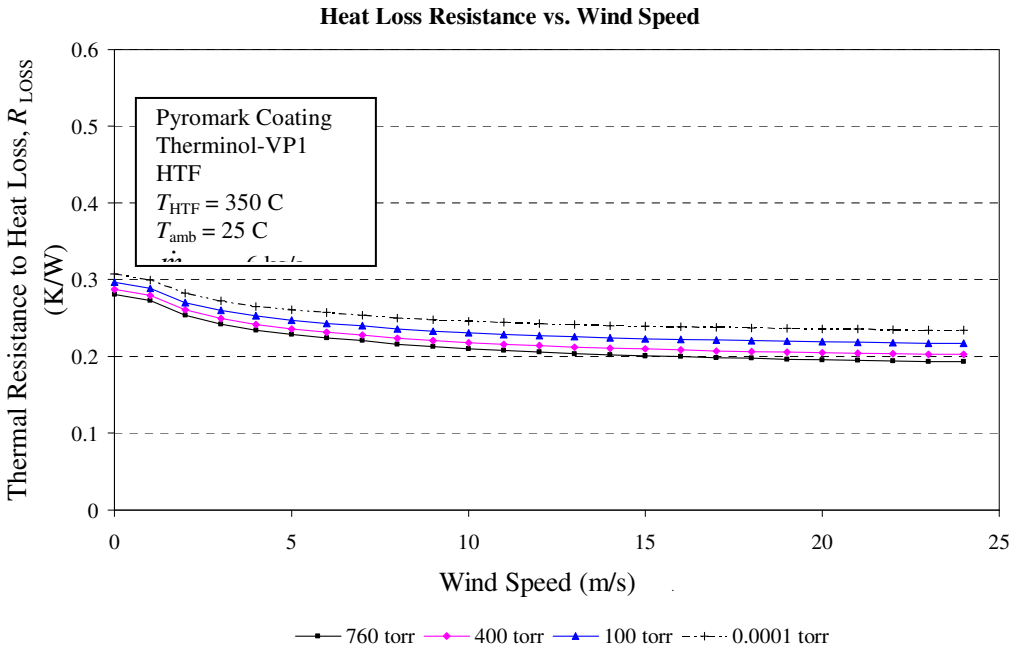

Figure 5.4.3: Heat Loss Resistance Wind Speed Dependence Plot

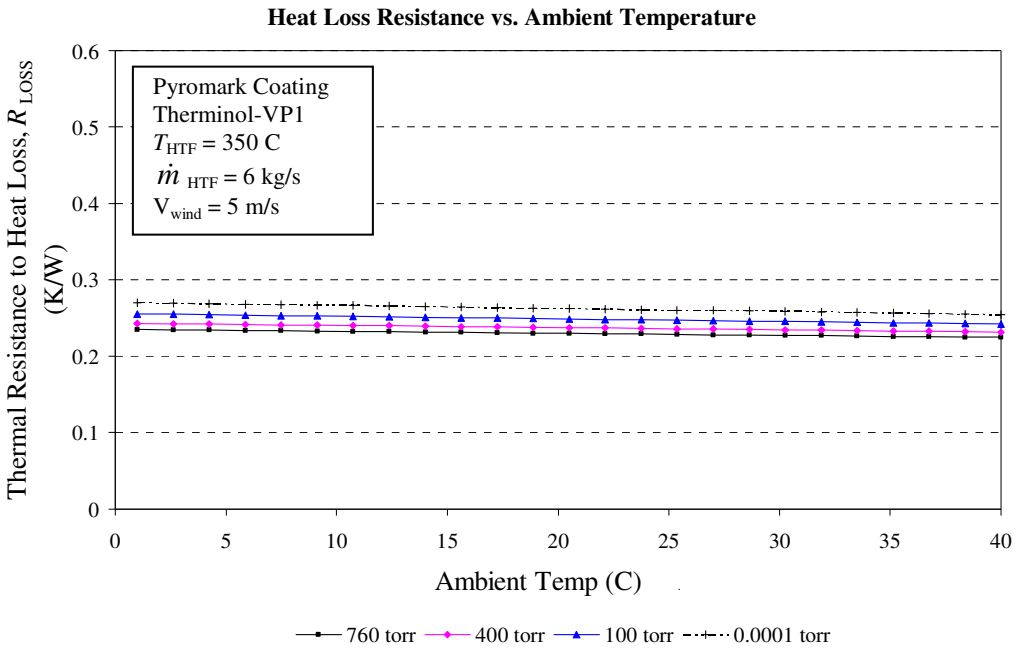

Figure 5.4.4: Heat Loss Resistance Ambient Temperature Dependence Plot

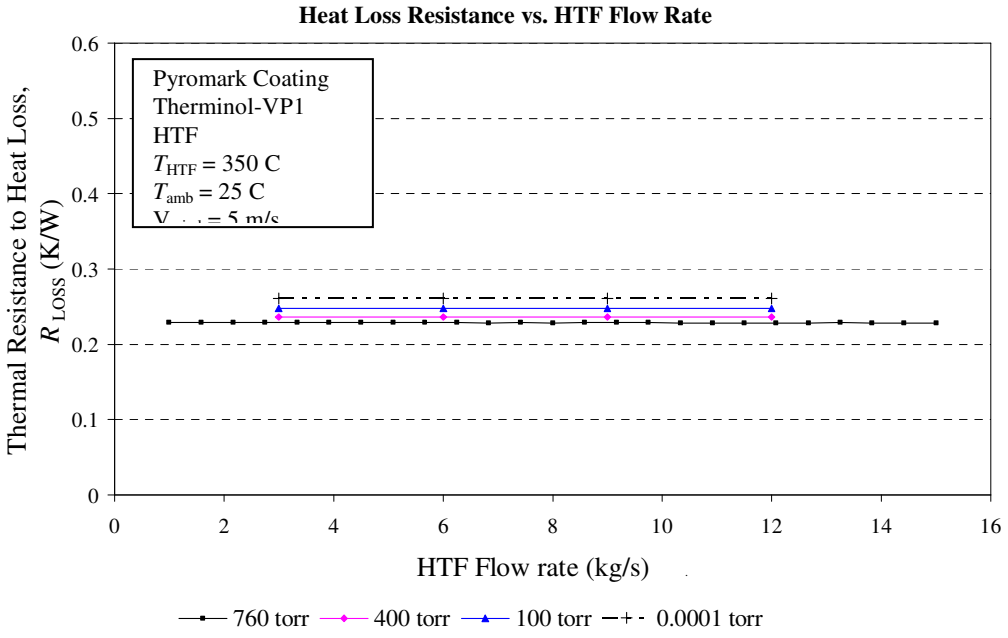

Figure 5.4.5: Heat Loss Resistance HTF Flow Rate Dependence Plot

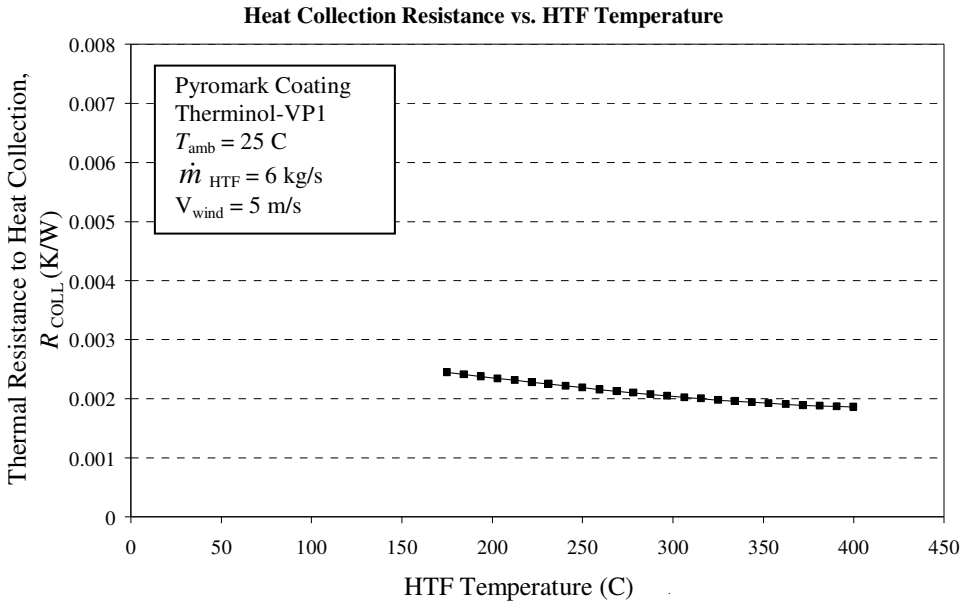

Figure 5.4.6: Heat Collection Resistance HTF Temperature Dependence Plot

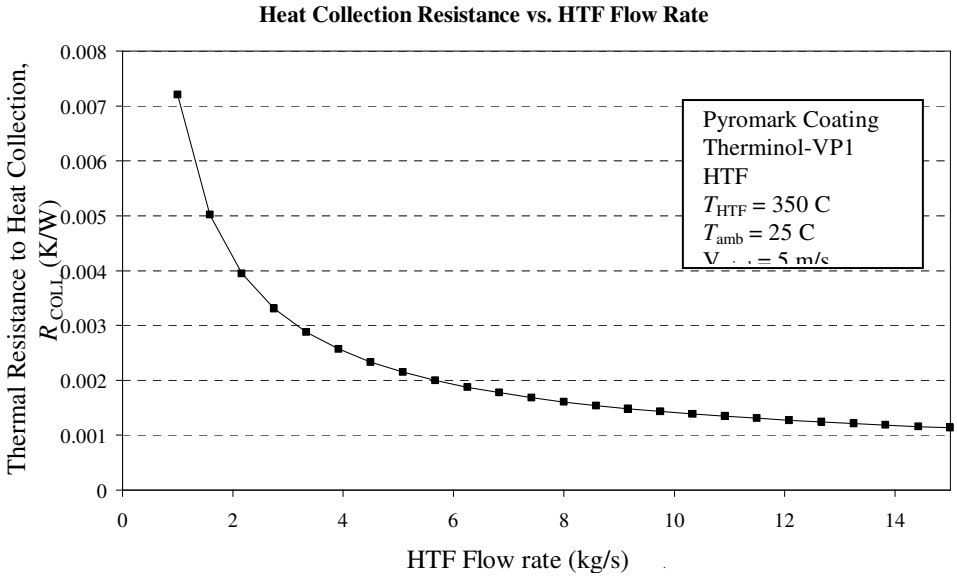

Figure 5.4.7: Heat Collection Resistance HTF Flow Rate Dependence Plot

5.5 REGRESSION MODELING OF THEORETICAL RESISTANCE CALCULATIONS

The EES model described above is adequate for representing the heat loss from the receiver. However, a simpler algebraic model similar to the empirical model already in use was deemed to be more suitable for incorporation into the existing simulation model. Hence, the analytical results of this complex EES model were used to develop simple regression models for the thermal resistance to heat loss, R_{LOSS}, and resistance to heat collection, R_{COLL}. Using these regression models allows the complex analytical receiver performance model to be accurately represented in the SEGS plant model by a minimal number of basic polynomial functions.

Based on evaluation of the initial EES model calculations (Figures 5.4.1 – 5.4.7) the R_{LOSS} regression model incorporated a combination of fluid temperature and ambient temperature, and the R_{COLL} model used only fluid temperature. Although wind speed and fluid flow rate fluctuations have an evident effect on heat loss resistance and heat collection resistance, respectively, the SEGS plant simulation model (SEGS simulator introduced in Chapter 6) does not incorporate these parameters into performance calculations. There is no way to define the wind conditions at any given time without introducing measured data into the simulation program. In addition, it is very difficult to estimate the wind conditions at the receiver tube with a typical receiver surrounded by many acres of other collectors serving as partial wind shields. The wind conditions at the receiver level are likely less significant than the actual wind measured at the level of the instrumentation. The plant model cannot account for these variations, so wind speed and fluid flow rate were kept constant for calculations in the resistance model. The average values of these two parameters from the test loop data were assigned as the constants in order to maintain consistency between the resistance model and the original collector efficiency models. The average wind speed was 2.88 m/s, and the average fluid flow rate was 3.18 kg/s.

To observe the effects of neglecting wind variation in the regression models, a more complex regression of the heat loss resistance was developed that included wind as a variable. This regression model was difficult to substantiate statistically, but did produce

resistance values that were reasonably consistent with values calculated by the analytical model. Using available wind data from SEGS, this more complex model was used to calculate the low efficiency receivers' performance in an annual SEGS plant performance simulation. This simulation assumed a solar field comprised completely of low efficiency receivers. The same simulation was conducted using the simple regression model of heat loss resistance, which neglects wind effects. The calculated total annual solar field heat collection from using the wind inclusive model was only 1.7% higher than the value obtained using the simple, temperature dependent regression model. Hence, for the purposes of modeling the performance of the entire solar field over an annual period, neglecting the effect of wind variation does not significantly alter the overall results.

Separate regression models were developed for theoretical "low efficiency" receiver tubes, with pressurized air or argon in the annulus and Pyromark as the absorber coating. Further, for each annulus gas, individual regression coefficients were calculated for receivers at different annulus pressures. The first regressions for R_{LOSS} considered T_{HTF} and T_{amb} as two independent variables, giving $R_{\mathrm{LOSS}} = f\left(T_{\mathrm{HTF}}, T_{\mathrm{HTF}}^2, T_{\mathrm{amb}}\right)$. This approach accounted for the slight variation in heat loss due to ambient temperature fluctuation. The regression based on these variables produced abnormally high uncertainties in the results, so a different method was used. The two temperatures were combined and represented as a single variable, ΔT, similar to that used in the original heat loss regressions of the collector efficiency models, giving $R_{\mathrm{LOSS}} = f\left(\Delta T, \Delta T^2\right)$. The uncertainties associated with the new results were near zero, validating the statistical accuracy of the models. A "high efficiency" receiver tube, with solar selective low emitting absorber coating and vacuum annulus, was also modeled with the EES program. These results were also represented by a quadratic regression on ΔT.

The quadratic regression for R_{COLL} was based only on T_{HTF}, yielding a function for the heat collection resistance of the form $R_{\mathrm{COLL}} = f\left(T_{\mathrm{HTF}}, T_{\mathrm{HTF}}^2\right)$. Representative plots of the R_{LOSS} vs. ΔT and R_{COLL} vs. $T_{\mathbf{HTF}}$ regressions are shown in Figures 5.5.1 and 5.5.2, respectively. The variation in Figure 5.5.1 is caused by a slight dependence of the heat loss resistance on ambient temperature. Tables 5.5.1 – 5.5.4 list the resultant coefficients of each regression,

along with the uncertainty, alpha risk, and R-squared values for each. All values are rounded to four significant digits.

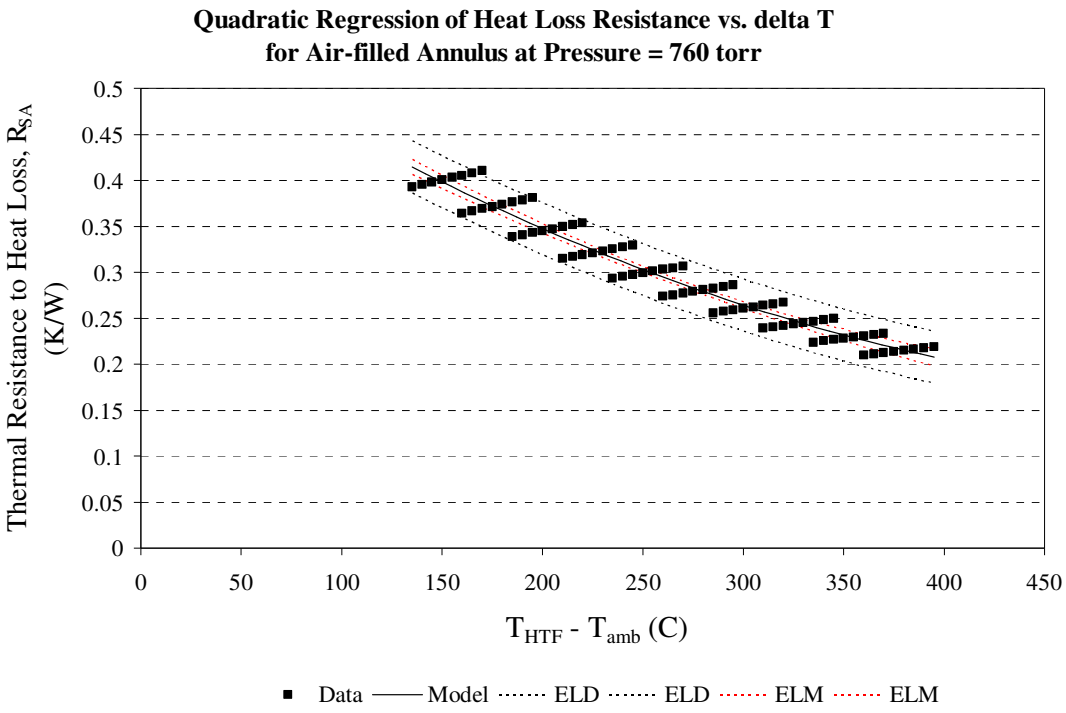

Figure 5.5.1: Representative Plot of R_{LOSS} Regression with Independent Variable ΔT

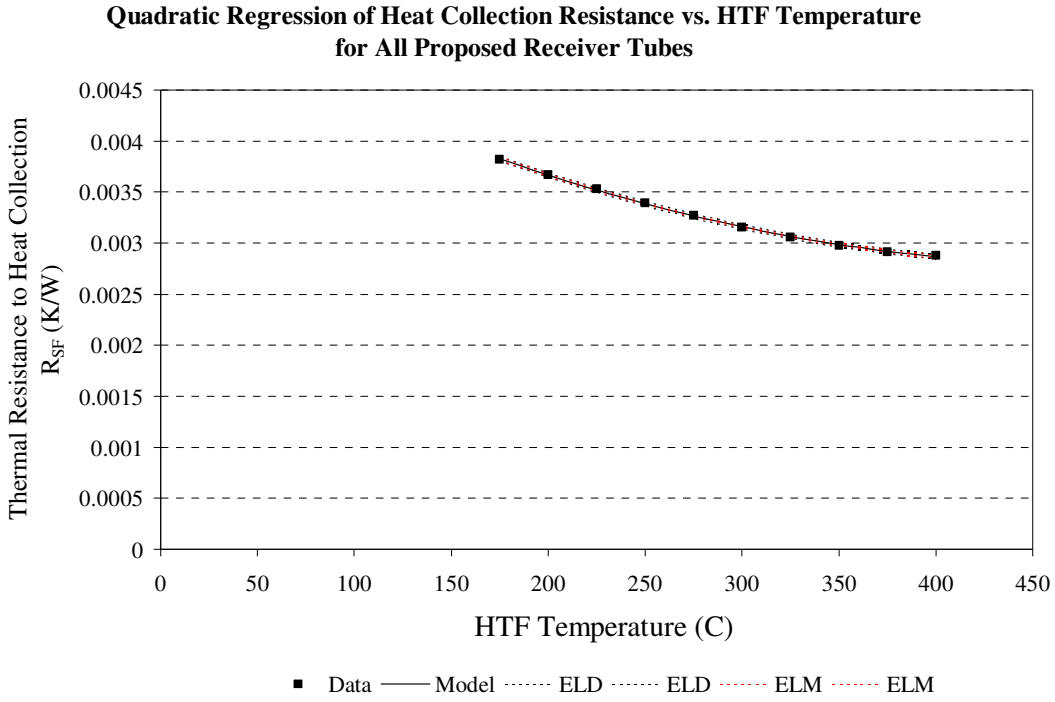

Figure 5.5.2: Representative Plot of R_{COLL} Regression with Independent Variable T_{HTF}

Table 5.5.1: Heat Loss Resistance Regression Model Coefficients for "Low Efficiency" Receiver w/ Air-filled Annulus

Annulus Gas Pressure	R_{SA} Constant	R_{SA} ΔT Coeff	R_{SA} ΔT^2 Coeff	Model U_A	Model R^2	Model Alpha Risk
760 torr	0.5866	- 0.001437	1.210E-06	0.0054	0.9456	≈0
400 torr	0.6387	- 0.001657	1.463E-06	0.006093	0.9439	≈0
100 torr	0.7277	- 0.002046	1.918E-06	0.007358	0.9403	≈0
0.0001 torr	0.8568	- 0.002645	2.660E-06	0.009227	0.9355	≈0

Table 5.5.2: Heat Loss Resistance Regression Model Coefficients for "Low Efficiency" Receiver w/ Argon-filled Annulus

Annulus Gas Pressure	R_{LOSS} Constant, L_1	R_{LOSS} ΔT Coeff, L_2	R_{LOSS} ΔT^2 Coeff, L_3	Model U_A	Model R^2	Model Alpha Risk
760 torr	0.642389	-0.00167	1.471E-06	0.0061	0.9438	≈0
400 torr	0.687846	-0.00187	1.705E-06	0.0068	0.9422	≈0
100 torr	0.761118	-0.0022	2.102E-06	0.0078	0.9392	≈0
0.0001 torr	0.856747	-0.00265	2.66E-06	0.0092	0.9355	≈0

Table 5.5.3: Heat Loss Resistance Regression Model Coefficients for "High-Efficiency" Receiver

R_{LOSS} Constant, L_1	R_{LOSS} ΔT Coeff, L_2	R_{LOSS} ΔT^2 Coeff, L_3	Model U_A	Model R^2	Model Alpha Risk
8.0768	-0.0322	3.654E-05	0.096	0.9362	≈0

Table 5.5.4: Heat Collection Resistance Regression Model Coefficients for All Receivers

R_{COLL} Constant, C_1	R_{COLL} T_{HTF} Coeff, C_2	R_{COLL} T_{HTF}^2 Coeff, C_3	Model U_A	Model R^2	Model Alpha Risk
0.005322	-1.041E-05	1.068E-08	1.06E-05	0.9994	≈0

Using the coefficients from these Tables, the resistance to heat loss and heat collection for a given receiver type is calculated using the following equations.

$$R_{\mathrm{LOSS}} = L_1 + L_2 \Delta T + L_3 \Delta T^2 \tag{5.5.1}$$

$$R_{\mathrm{COLL}} = C_1 + C_2 T_{\mathrm{HTF}} + C_3 T_{\mathrm{HTF}}^2 \tag{5.5.2}$$

These models can then be used to determine the theoretical heat collected by a receiver tube. Equation 5.1.2 has only one unknown variable, the absorber surface temperature, T_{S}. The value of T_{S} is determined from Equation 5.1.5, then Equation 5.1.2 is used to compute the total heat collected, $\dot{Q}_{\mathrm{COLL}}$, by the receiver.

$$\dot{Q}_{\mathrm{COLL}} = \eta_{\mathrm{OPT}} G_{\mathrm{BT}} A_{\mathrm{ap}} - \frac{T_{\mathrm{S}} - T_{\mathrm{A}}}{R_{\mathrm{LOSS}}} \tag{5.5.3}$$

To test the validity of this resistance model, Equations 5.5.1 – 5.5.3 were implemented into the Test Loop Processor and used to calculate the theoretical collector efficiencies of the low efficiency and high efficiency receivers. The results of these calculations were compared to the original collector efficiency data, determined from SEGS test loop data and represented in Figures 4.3.1 – 4.3.4. The low efficiency receiver calculations were compared to the refurbished collector data, as these two share the same absorber coating and annulus properties. This comparison is shown in Figure 5.5.3. The high efficiency receiver calculations were compared to the UVAC collector data, illustrated by Figure 5.5.4.

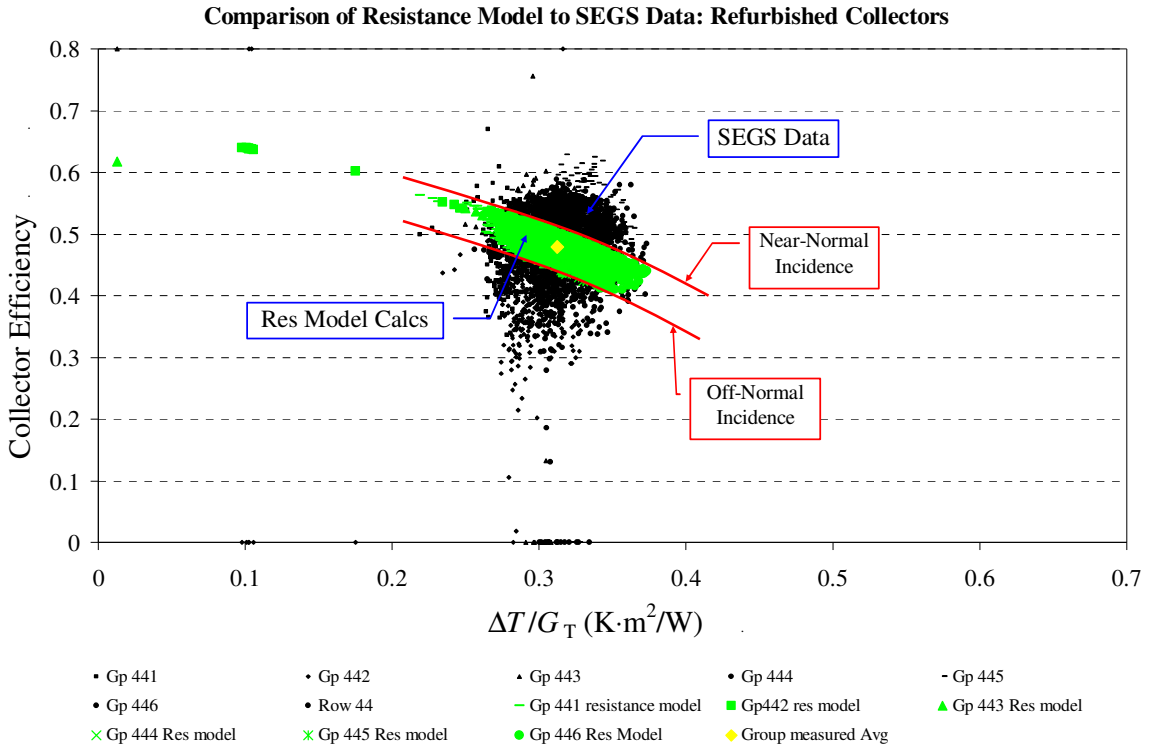

Figure 5.5.3: Efficiency Comparison of Resistance Model Calculations for Low Efficiency Receiver to SEGS Data for Refurbished Collectors

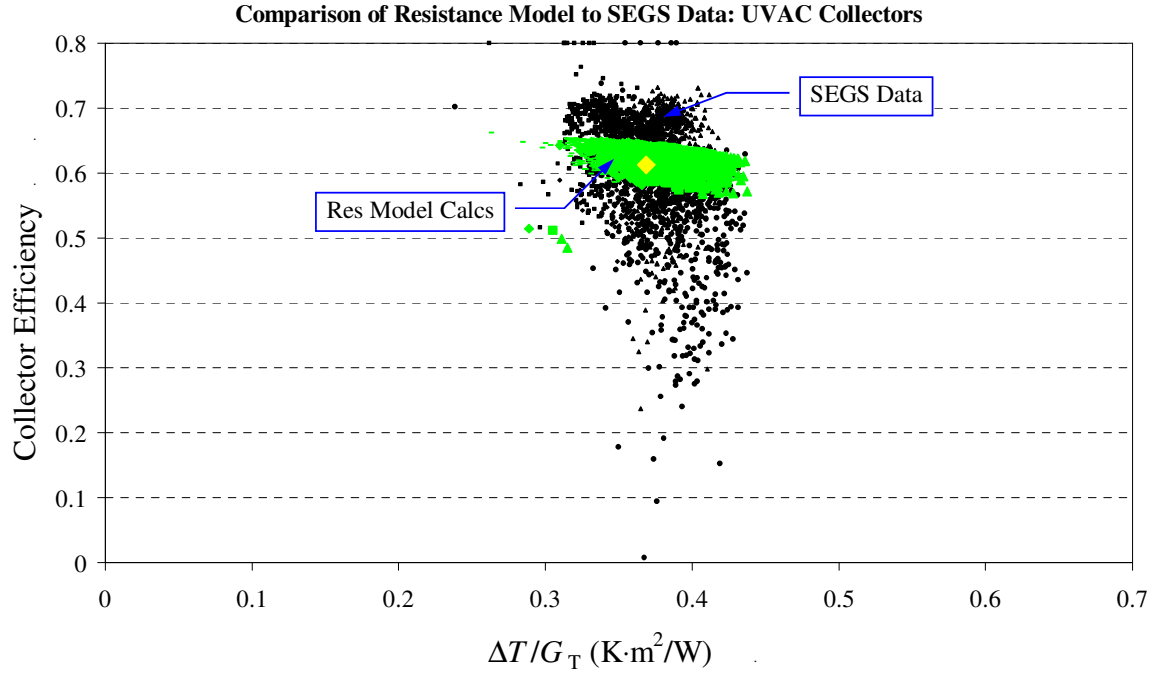

Figure 5.5.4: Efficiency Comparison of Resistance Model Calculations for High Efficiency Receiver to SEGS Data for UVAC Collectors

The graphical comparisons show agreement between the resistance model and measured data. In both cases, the model calculation results lie in the middle of the SEGS data and pass through the average point of the data, denoted by the yellow diamond. The scatter in the model calculations is likely due to one of three factors. The main source of scatter is variation in the calculated optical efficiency due to off-normal effects, which causes the efficiency curve to shift vertically up or down on the plot. When the incident radiation is near normal to the collector, the optical efficiency and collector efficiency maximized. At higher incident angles, corresponding to off-normal radiation, the optical efficiency decreases, and consequently so does the total collector efficiency. This behavior is represented in Figure 5.5.3 by the red lines along the top and bottom of the group of points from the resistance model calculations. Two other possible, but less influential, sources are non-linearity in the resistance model and variations in thermal resistance due to ambient temperature and flow rate that are not accounted for in the model. Due to time constraints, these factors could not be addressed to minimize the scatter. For future studies, these effects should be considered and accounted for.

Comparing the low and high efficiency receiver calculations, those of the low efficiency receivers correctly show a more rapid drop in performance with increasing temperature. This further ascertains the validity of the resistance model. Based on Figures 5.5.3 and 5.5.4, it was concluded that the resistance model is accurate in predicting the heat loss performance of the various receiver types. Since the model results are in agreement with actual data from SEGS, there is no need to compare it with other theoretical models, such as the NREL receiver tube heat loss model [Forristal, 2003], for validation.

CHAPTER 6: MODELING SEGS PLANT PERFORMANCE

6.1 PLANT PERFORMANCE DATA AND ENERGY CONVERSION MODELS

Plant performance data was collected at the SEGS facility using the instrumentation illustrated in Figure 3.2.2. Measurements were taken every two minutes and the data was recorded into an Excel spreadsheet for each month. Using Visual Basic code, the raw data was averaged over each hour, and hourly performance data was recorded in a summary data file for each month. The monthly summary files were compiled into an annual plant performance data file for the year 2005, with hourly lines of data including the following parameters:

Table 6.1.1: Parameters Recorded in the Annual Plant Performance Data File (by Index)

1. day of year	7. gross electric power	13. power block2inlet temp
2. hour of day	8. net electric power	14. power block1 outlet temp
3. ambient temperature	9. solar field inlet temp	15. power block 2 outlet temp
4. beam normal irradiance	10. solar field outlet temp	16. avg gas heater inlet temp
5. solar field heat rate	11. wind speed	17. gas heaters outlet temp
6. gas heater heat rate	12. power block1 inlet temp	

The beam normal irradiance (4) was measured simultaneously by three independent Normal Incidence Pyrheliometers (NIP). The largest measured irradiance value from the three NIPs for a given period of data was used for calculation of the hourly average. The SEGS facility employs four natural gas heaters, so the gas heater inlet and outlet temperatures were obtained by averaging the measured inlet and outlet temperatures of each independent heater.

The previously developed collector efficiency models can be employed in the plant simulation to calculate the predicted performance of the solar field, in particular the heat

collected by the field. In order to model the performance of the energy conversion plant, that is its effectiveness in converting collected heat into electric energy, a mathematical relationship between solar field heat collection and steam cycle electric power generation needed to be developed. A purely thermodynamic approach was a feasible option given the plant data available; however, this method would be excessively complex and would require extensive fluid property data, which is not readily available in the Visual Basic program, to be manually added to the model. To maintain simplicity in the model, a basic statistical analysis of the raw plant performance data was used to generate the necessary mathematical model for energy conversion.

The plant power output is dictated by three factors, the heat rate to the plant, the inlet temperature of the HTF to the plant from the solar field, and the heat rejection temperature of the steam cycle. Because of the way the field is operated, the heat rejection temperature does not change enough to cause significant changes in output. The inlet temperature is directly dependent on the heat rate, so for modeling purposes it can be assumed that the plant heat data also accounts for the changes in solar field outlet temperature. This assumption allows the electric power output to be defined by a function of only one variable, simplifying the model. Graphical comparison of the total heat generation data, which is the solar field heat collection plus the heat generated from the gas heaters, to the gross electric power output data exhibited a relatively linear relationship between the two. Hence, a linear regression of hourly gross electric power output, $\dot{E}_{\text{gross}}$, on hourly heat input, $\dot{Q}_{\text{total}}$, was performed to obtain the following equation:

$$\dot{E}_{\text{gross}} = B_{\text{Const}} + C_{\text{Coeff}}\dot{Q}_{\text{total}} \tag{6.1.1}$$

This equation is used to determine the gross electric energy produced for a given heat input to the conversion plant. Figure 6.1.1 shows the representative plot of this regression analysis, and Table 6.1.2 lists the statistical results and regression constants.

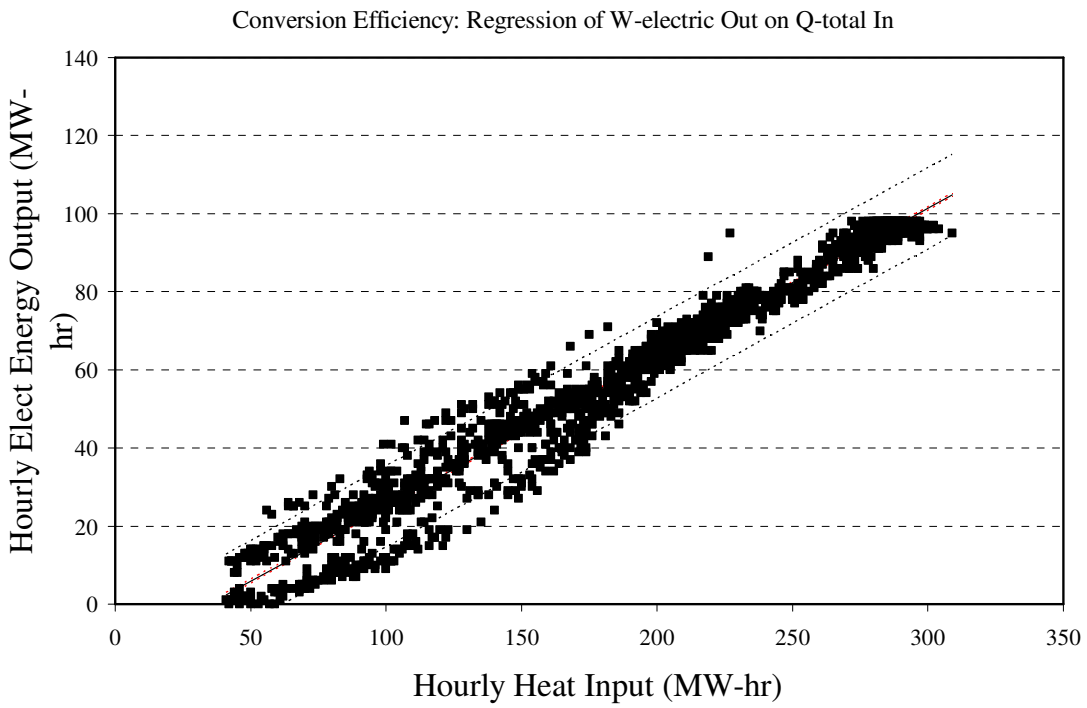

Figure 6.1.1: Regression Plot of Hourly Electric Energy Output on Hourly Heat Input

Table 6.1.2: Results of Regression of Electric Energy Output on Heat Input

B_{Const}	C_{Coeff}	Avg U_A	R^2	Alpha Risk
-13.1995	0.381957	0.36	0.964522	0

A similar analysis was conducted between data for the gross electric output and net electric energy delivered to the grid, $\dot{E}_{\text{net}}$. The results are presented in Figure 6.1.2 and Table 6.1.3. As the graph in Figure 6.1.2 shows, there is a clear linear relationship between the two. About 90 percent of the total electric energy produced is delivered to the grid for distribution, while the rest is sent back to power the plant itself. The equation for net electric output with respect to gross electric output, based on the statistical analysis, is as follows:

$$\dot{E}_{\text{net}} = D_{\text{Const}} + F_{\text{Coeff}} \dot{E}_{\text{gross}} \tag{6.1.2}$$

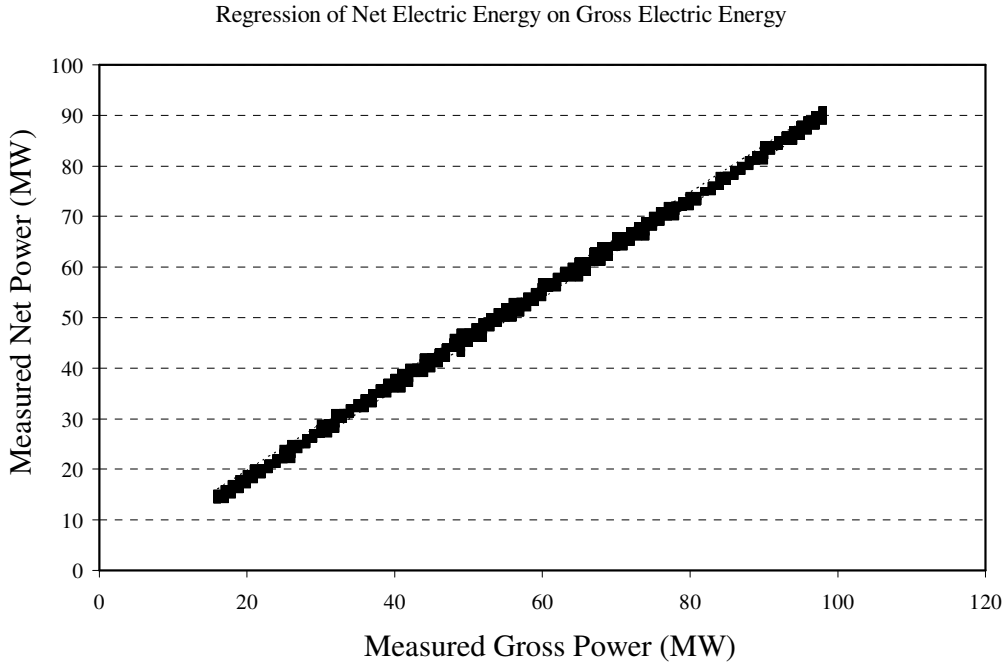

Figure 6.1.2: Regression Plot of Net Power Output to Gross Power Output

Table 6.1.3: Results of Regression of Electric Energy Output on Heat Input

D_{Const}	F_{Coeff}	Avg U_A	R^2	Alpha Risk
0.119574	0.917813	0.045	0.999142	0

Using Equations 6.1.1 and 6.1.2, the plant power output can be modeled given the total heat input to the heat transfer fluid.

6.2 MODELING SEGS PLANT PERFORMANCE USING THE SOLAR SIMULATOR PROGRAM

The Solar Simulator program combines the collector efficiency models, developed in the Test Loop Processor, with the theoretical collector heat loss models from EES

calculations and the energy conversion models, created using plant performance data, to simulate the overall annual performance of the entire SEGS unit. The model, written in Visual Basic for Excel, consists of several subroutines that perform calculations for individual systems within the SEGS facility. The main subroutines are as follows:

- Overall Modeling Routine
- Solar and Tracking Angle Calculation Routine
- Individual Solar Collector Performance Routine
- Solar Field Performance Routine
- Energy Conversion Plant Performance Routine

Hourly raw data from the annual plant performance data file, listed by index in Table 6.1.1, is inputted into the simulator at the start of the modeling routine. Data for day of the year, hour, ambient temperature, and solar irradiance are used throughout the program to perform various modeling calculations. The rest of the raw data is used only for comparative purposes after modeling has been completed. In the modeling routine, the solar field inlet and outlet temperatures are assigned their nominal values of 520 °F (271.1 °C) and 720 °F (382.2 °C) for on-peak operation. For off-peak operation, the solar field inlet temperature is increased by 20 °C. On and off-peak plant operation will be discussed in a later section. These temperatures are kept constant during operation by modulating the HTF flow rate through the field, so it is accurate to use these values for modeling. The solar field performance routine is called within the modeling routine. Here, the inlet and outlet temperatures for each SCA in the loop are calculated. The field performance routine then calls the collector performance routine. The collector performance routine calls the solar/tracking angle function, which calculates the incidence and tracking angle of the solar collectors based on the time of day and day of the year. The collector performance routine uses the calculated incidence angle, SCA temperatures, and measured ambient temperature to determine the efficiency and total heat collected by each collector type used in the simulation. These values are inputted back to the field performance routine, which uses them to compute the total solar field heat collection and field efficiency. The plant performance routine uses the field heat collection to model the electric power generation of the plant, as well as the plant conversion efficiency. Pertinent output values from each subroutine are recorded in an

output spreadsheet in Excel. Figure 6.2.1 shows a representative block diagram of the subroutine execution in the Solar Simulator. Pertinent inputs and outputs to each subroutine are shown next to the input/output arrows.

6.3 SOLAR SIMULATOR SUBROUTINES

Data Reader Subroutine

The Data Reader subroutine assigns values to all constant parameters used in modeling calculations. These values are specified in a data spreadsheet prior to executing the simulation and define certain specifications of the SEGS facility, as well as variables used for collector modeling. Table 6.3.2 lists the parameters defined in the Data Reader and their assigned values.

Table 6.3.2: Constant Parameters Used by Solar Simulator

site latitude	34.87
site longitude	116.78
length of data period	1 hr
optical efficiency on normal	0.733
Sandia Heat Loss Model Linear Coeff	0.05145 (W/m^2-K)
Sandia Heat Loss Model Quadratic Coeff	0.00069 (W/m^2-K^2)
incidence angle modifier	0.004
SCA area	548.4 (m^2)
number of loops in field	SEGS VIII = 142 / SEGS IX = 148

The optical efficiency and heat loss modifiers, f_{OPT} and f_{HL}, for the efficiency models represented by Equation 4.3.2 are entered in a table located in the data spreadsheet, and assigned an index number based on collector type. The Data Reader function reads and assigns each pair of modifiers to the corresponding collector type index (1-7). Similarly, regression coefficients for the resistance models represented by Equations 5.5.1 and 5.5.2 are

entered in a separate spreadsheet for proposed collector types not currently used at SEGS. For any theoretical collector types included in a given simulation, the Data Reader also assigns these regression coefficients to the corresponding index.

The simulated arrangement of collector types in the solar field is controlled by an input matrix located in the data spreadsheet. Each row of the matrix represents a specific collector (receiver tube) type, and each column represents an SCA location in the field loop. The SCA positions are labeled 1 – 6, 1 being the first SCA nearest the inlet and 6 representing the last SCA nearest the outlet. The intersecting cell of a given collector type – SCA position combination represents the fraction of SCAs at the specific loop location being filled by the specific collector type. For example, Figure 6.2.2 shows an unfilled input matrix. According to the matrix, 30 % of the SCAs at position 1 in the loop are filled with lost vacuum collectors, and 60% of the SCAs at position 3 are filled with used HCEs. Fractions are allocated to each cell so that the sum for each SCA location is one.

Collector Type	SCA index =	1	2	3	4	5	6
broken	1	0.05	0.04	0.02	0	0	0
cloudy	2	0.02	0.02	0.02	0	0	0
washed	3	0.03	0.04	0.02	0	0	0
lost vac	4	**0.30**	0.20	0.20	0.15	0.20	0.15
refurb	5	0.10	0.10	0.14	0.20	0.20	0.20
used	6	0.50	0.60	**0.60**	0.65	0.60	0.65
new	7	0	0	0	0	0	0
sum		1.000	1.000	1.000	1.000	1.000	1.000

Figure 6.2.2: Example SCA/Collector Combination Input Matrix

Embedded loops within the Data Reader subroutine assign fractions for each collector type – SCA position combination. Each possible combination is represented by a two-dimensional array variable, HCE_fraction (type_index, SCA_index).

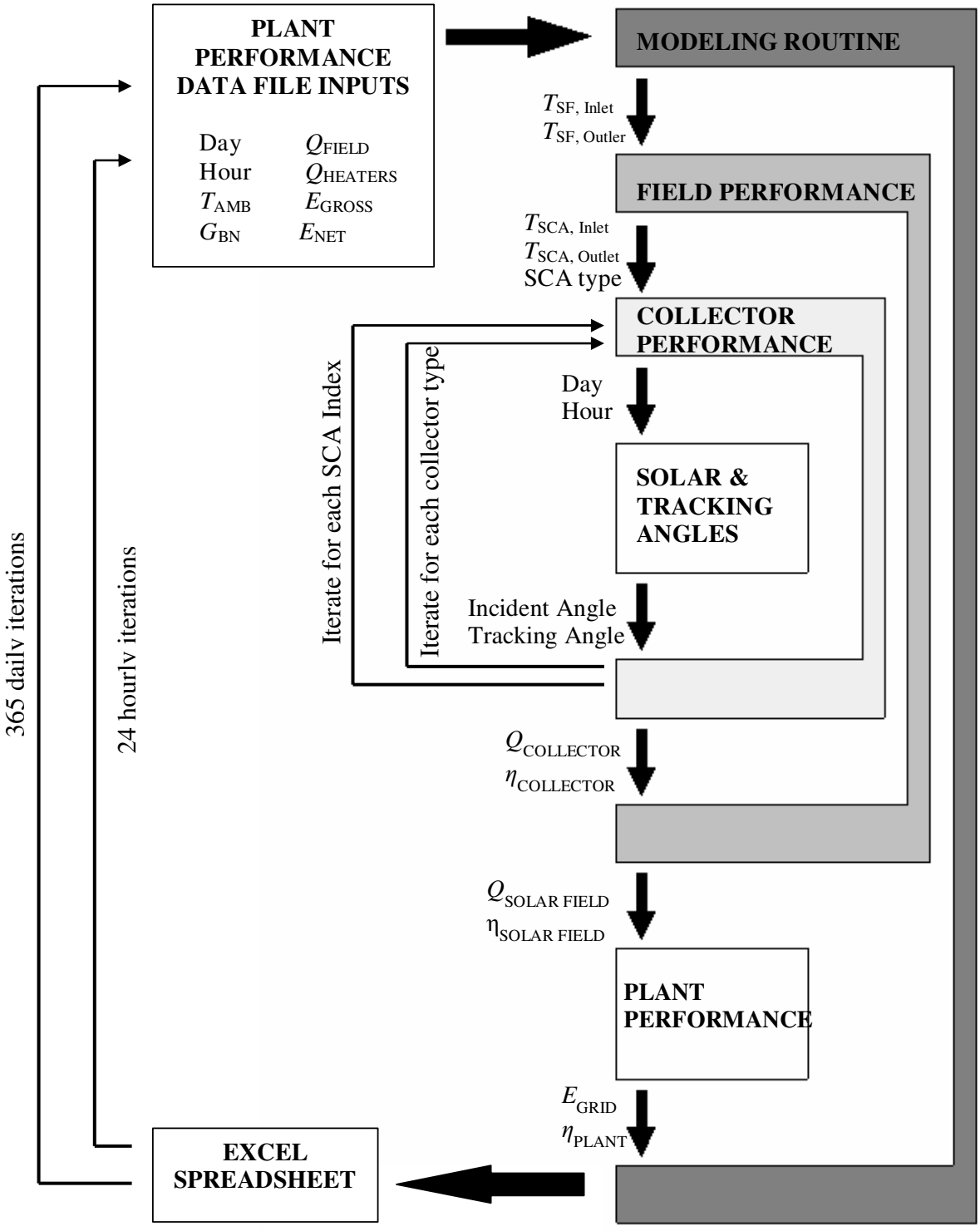

Figure 6.2.1: Block Diagram of Solar Simulator Code Execution by Subroutines

Modeling Routine

The Modeling Routine is the main function of the Solar Simulator, in which all other modeling routines are embedded. It consists, primarily, of two loops. The first is a 365 count loop representing each day of the year. Within that is a 24 count loop, in which the collector, field, and plant performance subroutines are called to perform the modeling calculations for each hour of the specified day. The schedule of on-peak and off-peak plant operation is also designated in this routine. On-peak operation occurs during the summer months when energy demand is very high. During on-peak operation, the gas heaters are used to supplement the heat transfer fluid and increase the plant's power output to meet the high demand. At off-peak times, typically in the winter months and on weekends, the solar field operates alone without the gas heaters. For simulations, the designated on-peak operation times are between 12:00 noon and 6:00 pm on weekdays between May 12 and September 28. These dates are based on observation of the gas heater outputs from plant data.

Field Performance Subroutine

The Field Performance Subroutine first calculates the inlet and outlet temperatures of each SCA in a loop. Based on the temperature scans from the test loop data, exemplified in Figure 4.1.1, the temperature change across a loop is assumed to be linear. Thus, the change in temperature over each SCA is determined by dividing the total solar field temperature change by six, the number of SCAs in a loop. Then, the inlet and outlet temperatures at each SCA are found by adding the incremental temperature change. The subroutine contains a six count SCA position loop embedded with a seven count loop for each collector type.

For each SCA index (1 – 6), the heat collected by each collector type is evaluated in the Collector Performance subroutine. The calculated heat collection is then multiplied by the fraction assigned in the collector/SCA input matrix. The computed heat collections from each type/SCA pair are summed to obtain the gross solar field heat collection, $\dot{Q}_{\mathrm{SF,GROSS}}$. An additional loss coefficient, U_{FIELD}, is introduced in computing the net solar field heat

collection, $\dot{Q}_{SF,NET}$, to account for any additional auxiliary losses that may be discovered during operation. The resulting equation for $\dot{Q}_{SF,NET}$ is as follows:

$$\dot{Q}_{SF,NET} = \dot{Q}_{SF,GROSS} - U_{FIELD}(T_{HTF} - T_{AMB}) \tag{6.3.1}$$

As no additional sources of loss have been found to this point, the field loss coefficient is set to zero, leaving the net heat collection equal to the gross heat collection.

Collector Performance Subroutine

The Collector Performance subroutine utilizes either the previously developed collector efficiency model, discussed in Chapter 4, or the receiver tube heat resistance model, presented in Chapter 5, to calculate the total heat collection by the designated collector type at a given SCA position. Collector types currently used at the SEGS plant are modeled with the test loop collector efficiency equations. Multiplying Equation 4.3.2 by the tilted beam irradiance and adding incident angle effects on the optical efficiency results in the following equations for heat collection per unit area.

$$\dot{Q}''_{COLL} = X_{END}\eta_{OPT}G_T - f_{RHL}C_1\Delta T + C_2(\Delta T)^2 \tag{6.3.2a}$$

$$\eta_{OPT} = f_{OPT}C_{off\text{-}axis}\eta_{OPT,NOM} - f_\theta\theta\left(\frac{1}{\cos\theta} - 1\right) \tag{6.3.2b}$$

X_{END} = End Effect Coefficient
$\Delta T = (T_F - T_{AMB})$
$C_{off\text{-}axis}$ = Off-axis Correction Coefficient
f_θ = Incidence Angle Modifier
θ = Incidence Angle (deg)

Collectors with theoretical receiver tubes are evaluated using the resistance models defined by Equations 5.5.1 – 5.5.3. The optical efficiency is computed using Equation 6.3.2b. Since the thermal resistance program does not model incident radiation on the receiver, the losses from imperfect absorptivity of the absorber surface are neglected. Although these losses are small, they may become significant when modeling performance over an extended period of time. Thus, the surface absorptance, as well as the SCA string end effects, are represented by coefficients to the optical efficiency and added to Equation 5.1.5, yielding the following equation for surface temperature:

$$T_S = \left\{ \frac{\alpha_{ABS} X_{END} \eta_{OPT} G_T A_{ap} R_{COLL} R_{LOSS} - R_{COLL} \left(T_F - T_{AMB} \right)}{R_{LOSS} + R_{COLL}} \right\} + T_F \tag{6.3.3}$$

The resistance model also neglects radiation absorbed by the glass envelope that is eventually lost to the ambient. Again, although this is a small amount of energy, it can accumulate over time and have significant effects on annual performance models. The heat loss from radiation absorption by the envelope is added to the original heat loss term in Equation 5.5.3. The Collector Performance routine computed the heat collection per unit area with the following equation.

$$\dot{Q}''_{COLL} = \alpha_{ABS} X_{END} \eta_{OPT} G_{BT} - \left\{ \frac{T_S - T_A}{A_{ap} R_{LOSS}} + \dot{Q}_{ENV} \right\} \tag{6.3.4}$$

$$\dot{Q}_{ENV} = \eta_{OPT} \alpha_{ENV} G_T \tag{6.3.5}$$

The heat transfer fluid temperature, T_F, is modeled as being constant across the length of one SCA. The value used is the average of the SCA inlet and outlet temperatures. The heat collected per area is multiplied by the aperture area to obtain the total heat collected for the given SCA location by the given collector type.

Plant Performance Subroutine

The Plant Performance subroutine models the energy conversion process. Prior to any calculations, the target on-peak gross power output, $\dot{E}_{G,Target}$, is set at 97 MW, and the maximum heat rate from the gas heaters is set at 200 MW. The maximum gas heat was determined based on observed plant performance data. The Solar Simulator provides the option of modeling or not modeling the gas heaters. If the heater model is off, the heat from the gas heaters, $\dot{Q}_{GAS}$, is assigned the measured value from the plant performance data. If the heater model is on, the subroutine calculates the gas heat based on the operating condition of the plant. For off-peak hours, the gas heaters are assumed to be off, so $\dot{Q}_{GAS} = 0$. For on-peak hours, the target total heat production, $\dot{Q}_{TOT,\,Target}$, can be calculated with the energy conversion model, Equation 6.1.1, and the target gross power output.

$$\dot{Q}_{TOT,\,Target} = \frac{\dot{E}_{G,\,Target} - B_{Const}}{C_{Coeff}} \tag{6.3.6}$$

The heater heat rate is then the difference between the target heat rate and the solar field heat collection.

$$\dot{Q}_{GAS} = \dot{Q}_{TOT,\,Target} - \dot{Q}_{SF,\,NET} \tag{6.3.7}$$

The change in heater heat rate over each hour is monitored to ensure that the increase or decrease is feasible for a one hour time period. The maximum change in heater heat rate is set at 35 MW for all simulations. If this value is exceeded the heater heat rate is set to 35 MW above or below the previous hour's value. The total heat rate to the conversion plant is then computed from:

$$\dot{Q}_{TOTAL} = \dot{Q}_{SF,\,NET} + \dot{Q}_{GAS} \tag{6.3.8}$$

Given the total heat rate, Equations 6.1.1 and 6.1.2 are employed to calculate the net electric energy delivered to the grid. The plant conversion efficiency is defined as the net energy over total heat rate.

$$\eta_{\text{PLANT}} = \frac{\dot{E}_{\text{GRID, NET}}}{\dot{Q}_{\text{TOTAL}}} \tag{6.3.8}$$

Program Outputs

As aforementioned, the Solar Simulator program combines the data-based collector efficiency models, theoretical receiver heat resistance models, and the statistical data-based energy conversion models to simulate the performance of the SEGS solar field and conversion plant. The main calculated outputs of the program are the total solar field heat collection, gas heat, net electric power to the grid, and total plant conversion efficiency. These output parameters are calculated at each hour and recorded in the Excel output sheet. Also recorded in this sheet are the measured SEGS performance parameters obtained from the annual data summary file. The hourly values of each parameter are summed to obtain cumulative annual quantities. As will be discussed in Chapter 7, the simulation results of the current SEGS VIII solar field are in very close agreement with the measured performance data from 2005. The annual gas heat production and on and off peak electric power outputs are important outputs of the program, as they are necessary to conduct the solar field optimization analysis, which will be discussed in Chapter 7.

CHAPTER 7: SIMULATION RESULTS & SOLAR FIELD OPTIMIZATION

7.1 MODELING THE CURRENT SEGS UNIT

To test the accuracy of the Solar Simulator, the current SEGS VIII solar field collector arrangement was modeled. The calculations were compared to the measured plant performance data from the annual summary file. Table 7.1.1 shows the model results and measured data from 2005 for a select group of parameters. As evidenced by the simple error analysis, the Solar Simulator was able to predict the cumulative annual power output with great accuracy, differing only by 3 % from the actual measured output. The other calculated parameters were in even closer agreement with measured data.

Table 7.1.1: SEGS Plant Model Results for Current SEGS VIII Solar Field Arrangement

	Calculated Value	Measured Value	% Error of Model
Net Electric Power (MW-hr)	134,031	138,212	3.03 %
Total Gas Heat (MW-hr)	60,483	61,250	1.25 %
Total Field Heat Collection (MW-hr)	428,832	438,605	2.23 %
Plant Efficiency	0.405	0.414	2.17 %

A graphical comparison of modeled and measured data is presented in Figures 7.1.1 and 7.1.2. Figure 7.1.1 shows calculated and measured values of tilted beam irradiance (incident solar energy), solar field heat collection, gas heat, total plant heat, and net electric power output as functions of time during days 99 – 105. These are days of off-peak plant operation. Figure 7.1.2 presents the same hourly parameter values for days 183 – 189, which fall within the period of on-peak operation. As aforementioned, on-peak operation is modeled from 12:00 noon to 6:00pm on weekdays between May 12 and September 28. All heat rates and power outputs in Figures 7.1.1 and 7.1.2 are represented in MW. Analysis of

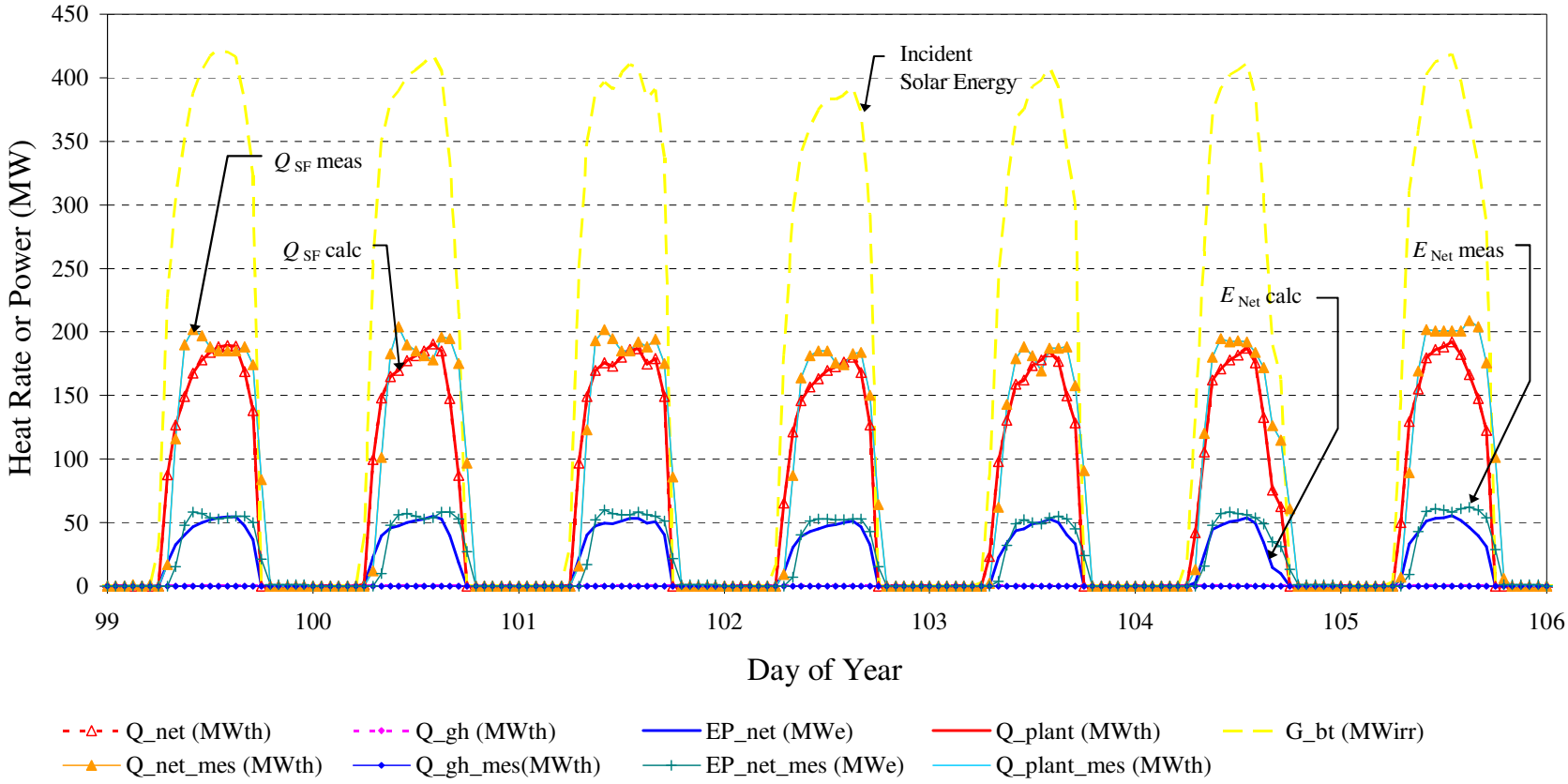

Figure 7.1.1: Graphical Comparison of Simulated SEGS Model to Measured Data (Off-Peak Operation)

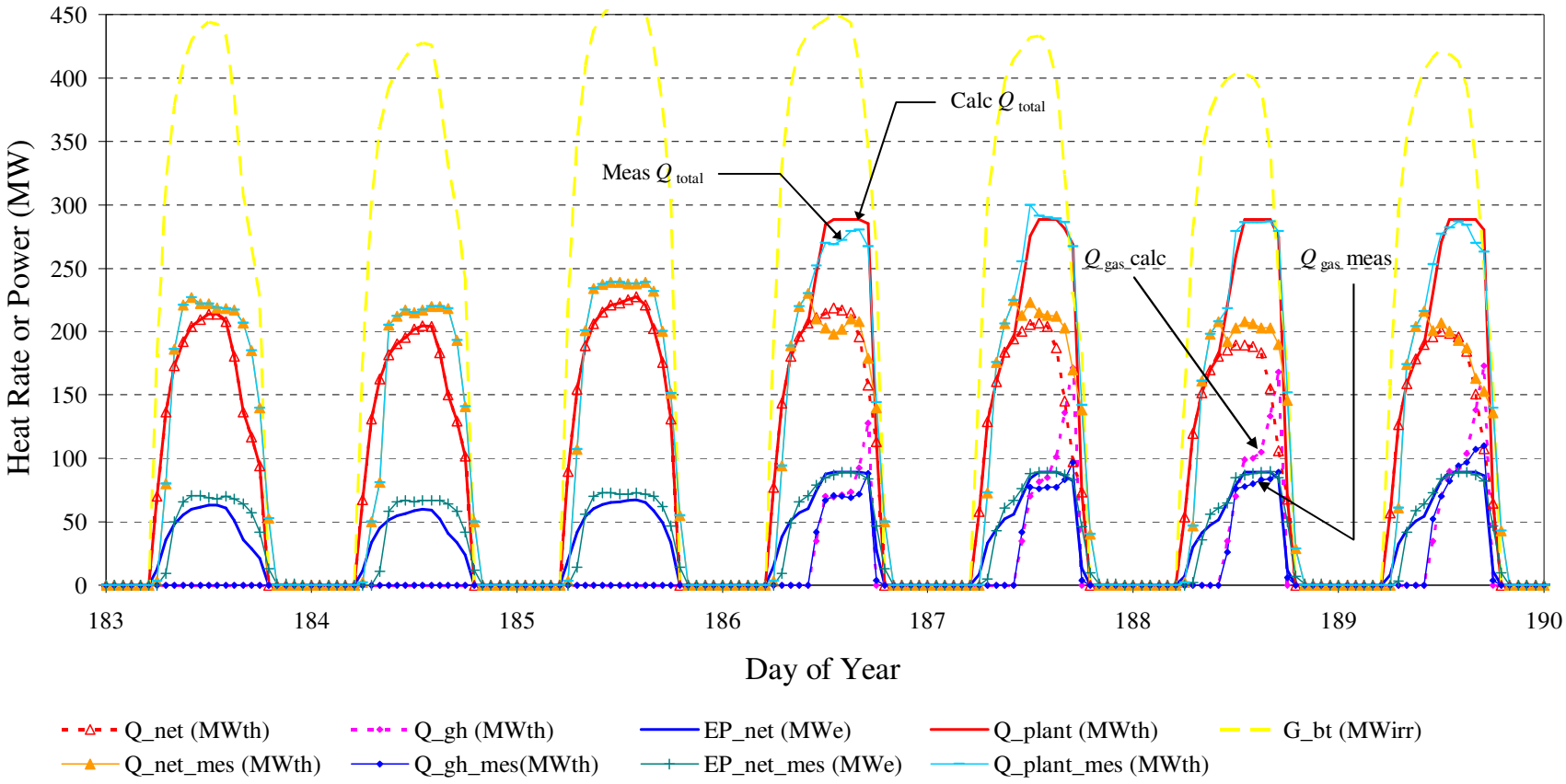

Figure 7.1.2: Graphical Comparison of Simulated SEGS Model to Measured Data (On-Peak Operation)

these graphical results gives further evidence of the accuracy of the Solar Simulator program, as the calculation results and SEGS data are virtually congruent.

The total plant heat, as discussed in Section 6.3, is the sum of the solar field heat collected and gas heat produced. The total heat correctly aligns with the solar field heat during off-peak operation, when no gas heat is produced, and increases significantly during on-peak operation with gas heat added. The calculated total heat plateaus in the middle of on peak days as a result of the bounds implemented in the simulation program.

The simulator does not account for any lag in the heating of the field in the morning and cooling of the field in the evening. Rather, it assumes that the field is operating at steady state at all times, causing heat collection calculations to strictly follow the change in irradiance. During actual operation at SEGS the field takes time to heat once exposed to the sun and to cool down once the sun moves past normal incidence. Therefore, it is typical to see the calculated solar field heat increase before the measured data does at the beginning of the day. At the end of the day the calculated value typically drops before the data shows a decrease in heat collection. This behavior is illustrates in Figures 7.1.1 and 7.1.2. Consequently, there is a slight time offset between the calculated and measured gas heat produced. As Figure 7.1.2 shows, the calculated gas heat rises suddenly at the end of the day due to the premature drop in calculated field heat, while the data shows no such rise.

Discrepancy in the gas heat results may also be due to varying target power outputs at SEGS. In actual application, the energy demand may fluctuate from day to day, so the target power output is likely not constant as the model assumes. This may also explain the slight deviation between the calculated and measured gas heater outputs.

Despite these slight inconsistencies, the Solar Simulator still predicts the desired outputs with relative accuracy. The time lag in the measured data is less significant when looking at the cumulative annual results. It is the annual quantities that are evaluated when conducting the collector field optimization analysis, which will be discussed in Section 7.3.

7.2 SIMULATION RESULTS FOR THEORETICAL COLLECTOR ARRANGEMENTS

Once its accuracy was verified, the Solar Simulator was used to model the performance of a SEGS plant with different collector field configurations. Each of the evaluated field arrangements contained some combination of "low efficiency receivers", LER, and "high efficiency receivers", HER. The modeled LER contains air at atmospheric pressure in its annulus, and its absorber tube is coated with Pyromark ($\alpha \approx 0.95$, $\varepsilon \approx 0.875$). The modeled HER has a vacuum annulus and solar selective coating, with a slightly improved absorptance of 0.965 and low emissivity. The theoretical performance of these receiver types was calculated with the resistance model defined by Equations 5.5.1 – 5.5.3. The heat loss resistance calculations for the LER used regression coefficients from Table 5.5.1. Those for the HER used regression coefficients from Table 5.5.3. The characteristics of the two receiver types used for simulations are summarized in Table 7.2.1.

Table 7.2.1: Properties of Simulated Theoretical Receiver Types

Receiver Type	Annulus State	Absorber Coating	Coating α	Coating ε	Heat Loss Resistance Coeffs Used
LER	Atmospheric Air	Pyromark	0.95	0.875	Table 5.5.1
HER	Vacuum	Solar Selective	0.965	0.07 – 0.14 (Temp dependent)	Table 5.5.3

Plant simulations were conducted for different loop SCA combinations of these two collector types. The number of SCAs filled with LER collectors in the loop was varied for each calculation and the remaining undefined SCAs were filled with HER collectors. The first calculation was conducted with 100% HER collectors in the field. The second simulation had LER collectors in the first SCA position, corresponding to the inlet of the loop, and HER collectors in the last five SCA positions. Each subsequent calculation placed LER collectors in the next SCA position in the loop, while keeping the remaining SCAs filled with HERs, until the final calculation had 100% LER collectors. Figure 7.2.1

illustrates the distribution of collector types in the SCA loops for each of the simulations that was conducted.

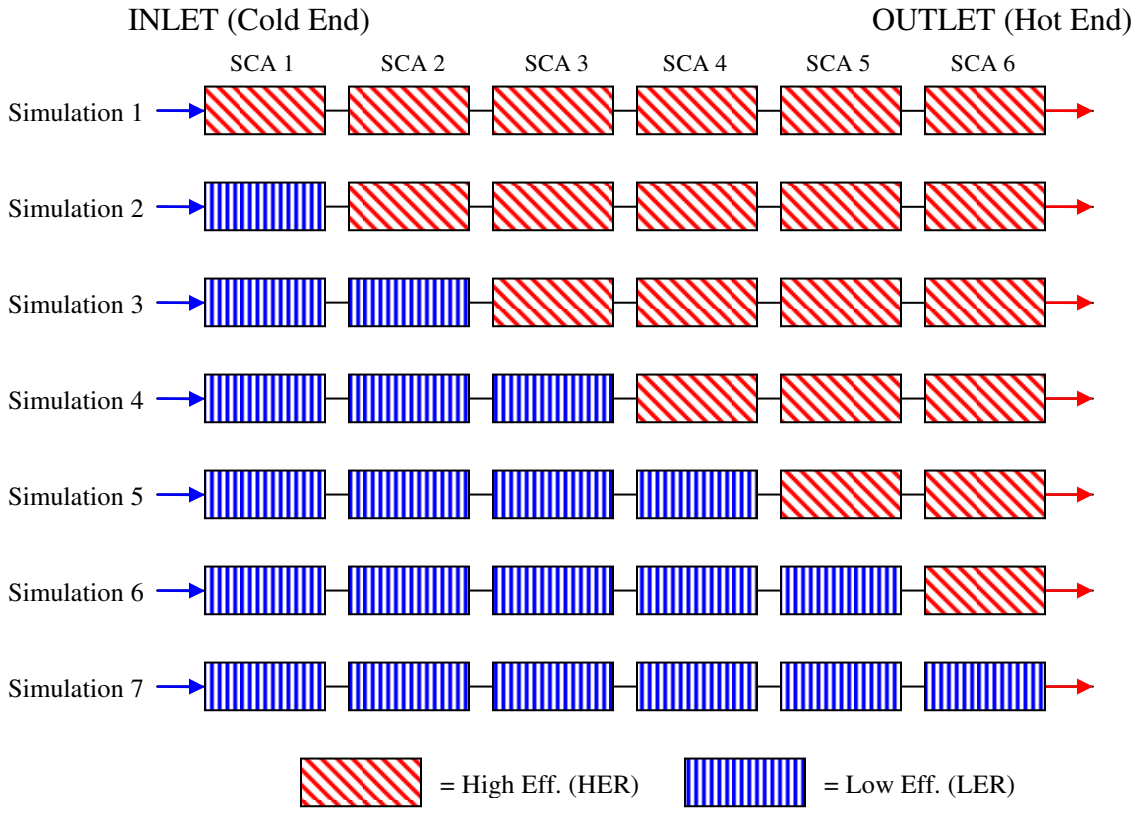

Figure 7.2.1: Distribution of Collector Types for Plant Simulations

Figure 7.2.2 shows the results of the seven simulations described above. Simulation 1, with 100% HER collectors, corresponds to zero on the x-axis, and simulation 7, with 100% LER collectors, corresponds to 6. Measured SEGS performance data are represented by the horizontal lines. Simulation results show that a solar field comprised almost entirely of LER collectors would perform as well as the current SEGS VIII solar field, of which about 60% of the collectors contain vacuum covered Luz receivers. The remaining collectors in SEGS VIII have either lost vacuum or been broken or degraded.

The simulation routine of Figure 7.2.1 was also performed with low efficiency receivers of different annulus gas pressures to observe the insulating effect of lowering the

pressure. Varying annulus pressure was only considered for the LER collectors, while the HERs were assumed to be at hard vacuum for all simulations. The simulation results are presented in Figure 7.2.3. A comparison of solar field performance and net power output between low efficiency receivers with air-filled and argon-filled envelopes is presented in Figure 7.2.4. Argon was examined because of its low thermal conductivity, lower than that of air, which could significantly improve annual collector performance.

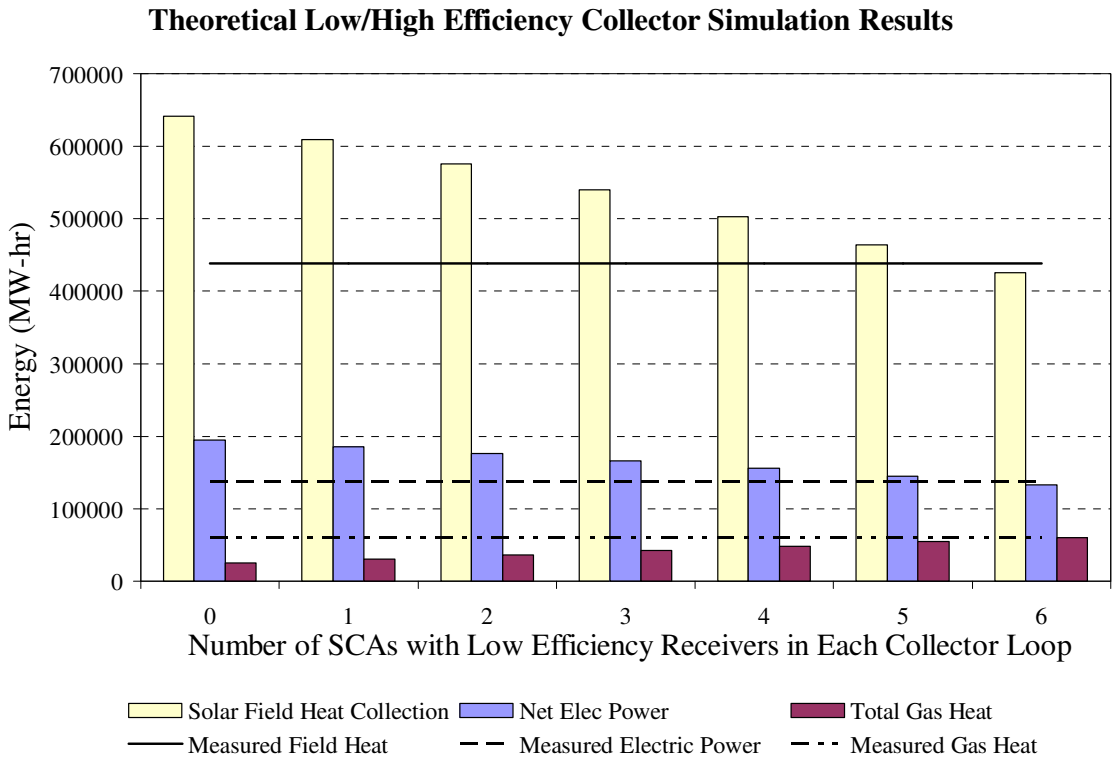

Figure 7.2.2: Simulation Results for Varying LER-HER Collector Combinations

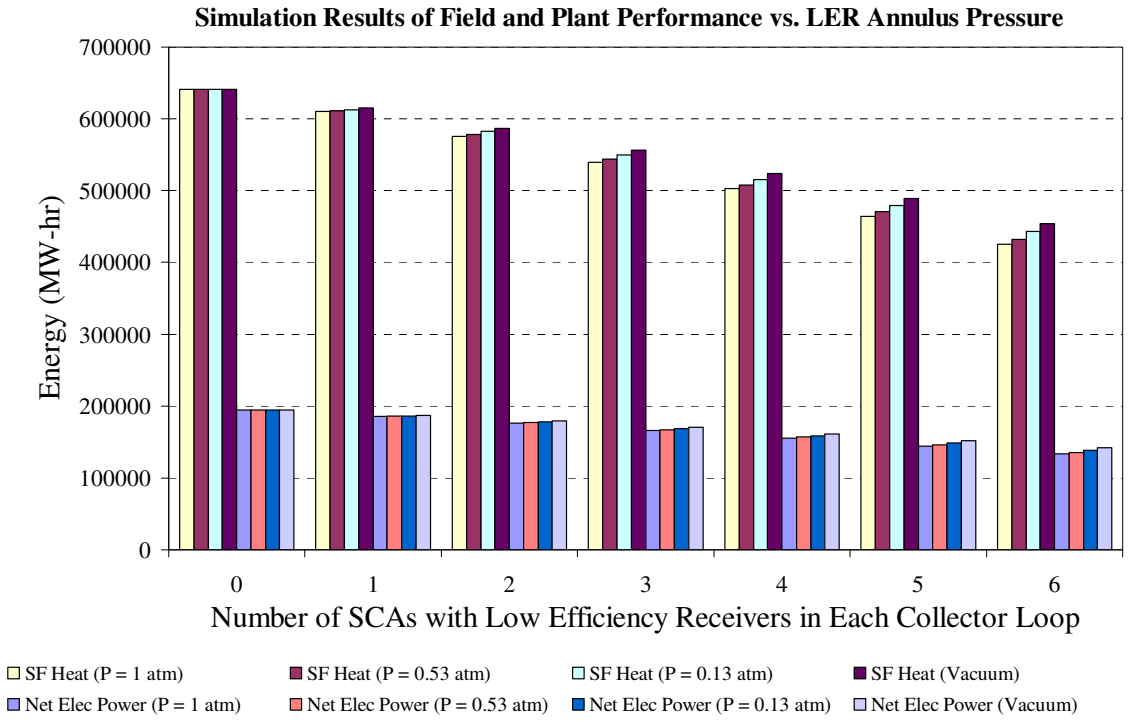

Figure 7.2.3: SF Heat Collection and Net Power Output at Various Annulus Pressures in the LERs (HERs kept at hard vacuum)

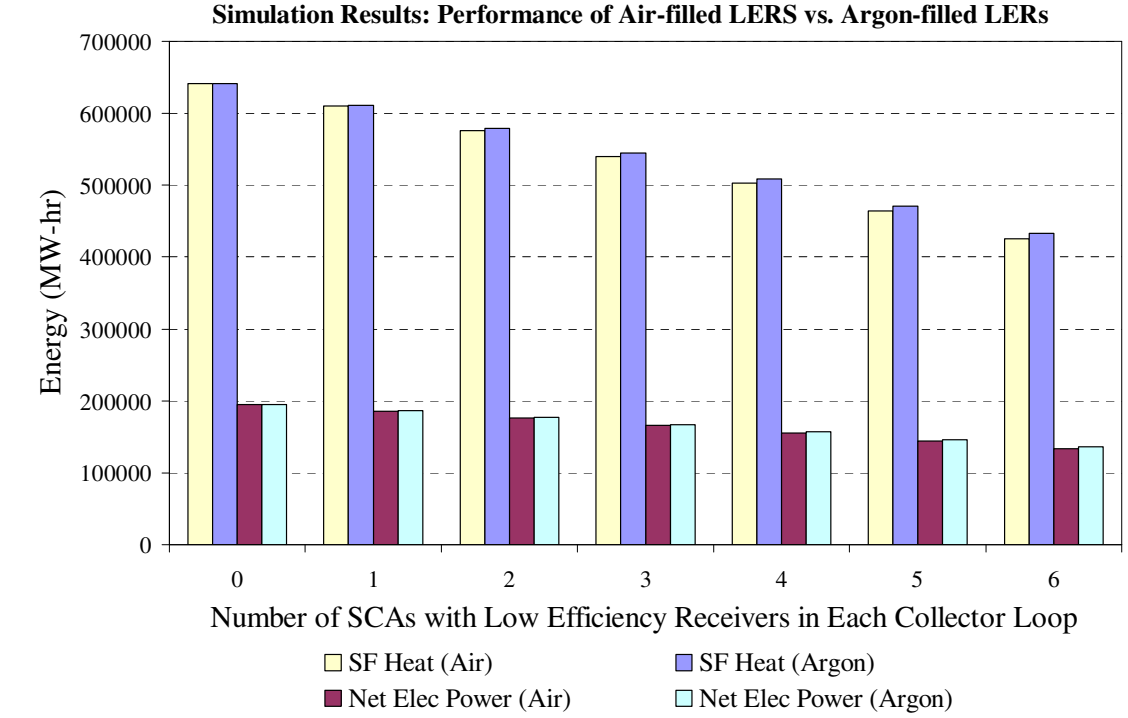

Figure 7.2.4: Field and Plant Performance with Air-filled and Argon-filled Annuli in the LERs (HERs kept at hard vacuum)

As Figure 7.2.4 illustrates, lack of vacuum has only a minor influence on performance when LER collectors are used. Evacuating the annulus in the low efficiency receiver produces only a slight increase in performance. This outcome is concurrent with the pressure dependent resistance of the low efficiency receiver, shown in Figures 5.4.1 and 5.4.1b. The high emissivity of the coating in the LER increases the radiation heat loss and minimizes the benefit of keeping the annulus at vacuum. For a solar field comprised entirely of low efficiency receivers, the annual field heat collection with vacuum covered tubes is only 6.3 % higher than that with receivers filled with atmospheric air. The difference in net electric power output is less than 6 %. The production cost of this receiver would likely be significantly lower without having the annulus at vacuum. In addition, as evidenced by the current SEGS receivers, there is a chance that the vacuum will be compromised at some point during operation, lessening its efficiency. The increased plant output from using vacuum receivers of this type does not appear to outweigh the cost disadvantages it creates. Therefore, the original low efficiency receiver with annulus at atmospheric pressure is likely the most cost effective.

The same can be said for the argon-filled receivers. Adding argon only increases the total electricity output by 1.7% over the air-filled receivers, and injecting and sealing argon within in the envelope would undoubtedly increase production costs. Again, an air-filled annulus appears to be the best alternative for the low efficiency receivers.

7.3: COLLECTOR FIELD OPTIMIZATION

The optimal arrangement of collector types in the collector field can be defined economically as that which maximizes the economic benefits (benefits – costs) of power production. The cost of new receivers is an almost instantaneous cost incurred at the start of the refurbishment project, while the economic benefit extends for many years into the future. Therefore, some type of analysis is necessary to account for the present worth of the future benefits. This type of analysis is generally called Life Cycle Cost Analysis (LCCA). See Fuller [2005] for an exposition and explanation of an influential requirement for LCCA. It is

noted that the connotation, but not necessarily the academic definition, of LCCA is an analysis that accounts for the future costs of construction, owning and operating, and even disposing of a physical asset. In slight contrast, Fuller [2005] defines Life Cycle Costs (LCC) as "…the sum of present values of investment costs, capital costs, installation costs, energy costs, operating costs, maintenance costs, and disposal costs over the life-time of the project, product, or measure." By this definition, the planning period covered by the LCCA may be the physical life of the project, but it is more commonly a shorter period representing the economic horizon of the entity making the investment. For this study the planning period is only three years, which is consistent with usual practice in entrepreneurial private industry. Since the planning period is so short, inflation of costs or benefits or the discounting of future costs can be disregarded. Hence, a simplified LCCA, which ignores inflation and future discounting, for a relatively brief planning period is used for this analysis. To minimize any confusion, the result will be called herein the Planning Period Cost (PPC).

The field optimization analysis is aimed at maximizing the annualized planning period benefit of a SEGS plant. The net annual benefit, AB_{NET}, can be represented by the difference between the annual revenue earned from energy sales and the cost of natural gas used in energy production.

$$AB_{\text{NET}} = \{P_{\text{OP}}E_{\text{OP}} + P_{\text{NP}}E_{\text{NP}}\} - C_{\text{GAS}}Q_{\text{HEATERS}} \tag{7.3.1}$$

A distinction must be made between on-peak power output, E_{OP}, and off-peak power output, E_{NP}, as there is a large discrepancy between their selling prices, P_{OP} and P_{NP}. The natural gas cost per gigajoule is denoted by C_{GAS}. The gas heat in Equation 7.3.1, Q_{HEATERS}, is based on the simulated annual gas heater output, but it also accounts for the efficiency of the gas heaters. Because the heaters are not 100% efficient, more gas is required to overcome losses and produce the desired heat output. Therefore, the efficiency must be accounted for to ensure accurate costs of gas used. Based on information obtained from SEGS personnel, the gas heater efficiency used in the optimization calculations is 92% based on the lower heating

value of the fuel. The net planning period benefit, PPB_{NET}, is calculated from the following equation:

$$PPB_{NET} = LCCF \cdot AB_{NET} - PPC_{EQUIP} \tag{7.3.2}$$

The life-cycle cost factor, *LCCF*, accounts for the time value of money over the payback period of the receiver tubes. In this simplistic analysis, inflation and discount are ignored, so the *LCCF* is merely the number of years in the planning period. Hence,

$$LCCF = Y_{PP} \tag{7.3.3}$$

In terms of identifying relevant costs, only those that differ among collector types need be included in this analysis. The only two relevant sources of cost are that of the natural gas, used in the gas heaters, and the planning period cost of the receiver tubes. The former is already accounted for in Equation 7.3.1. The planning period cost of the equipment, PPC_{EQUIP}, includes all acquisition and maintenance costs of each receiver tube in the field. It does not include any equipment costs that have already been incurred, such as original equipment installation, or future costs that do not differ among alternatives, such as maintenance of the reflecting mirrors. The *PPC* of a given receiver is represented by the receiver's installed "capital cost", CAP_{REC}. With a variety of receiver types being employed, the total planning period cost of equipment is determined by the following:

$$PPC_{EQUIP} = \sum CAP_{REC} N_{REC} \tag{7.3.4}$$

Here N_{REC} is the number of receivers of that type in the field. In the electric power industry, annualized costs are commonly used, so a simple annualized benefit should be calculated. Dividing Equation 7.3.2 by the *LCCF* and substituting Equations 7.3.1, 7.3.3, and 7.3.4 yields the following expression for the Annualized Planning Period Benefit (*APPB*) of the refurbishment of a SEGS collector field.

$$APPB = \{P_{OP}E_{OP} + P_{NP}E_{NP}\} - \left\{C_{GAS}Q_{HEATERS} + \frac{\sum CAP_{REC}N_{REC}}{Y_{SPB}}\right\} \quad (7.3.5)$$

Equation 7.3.5 was employed to determine the optimal combination of low efficiency and high efficiency receiver tubes in the field. Results from the original simulations are summarized in Table 7.3.2. These computed values, along with the cost and price estimates shown in Table 7.3.1, were substituted into Equation 7.3.5 to determine the annualized planning period benefit for each simulated arrangement of collectors. The planning period cost of one low efficiency receiver is estimated at $300, while that one of high efficiency receiver is estimated at $1500. These values are based on input from SEGS personnel. The combination yielding the highest *APPB* is the optimal collector field design. The results of this analysis are presented in Table 7.3.3 and Figure 7.3.1.

Table 7.3.1: Cost and Price Estimates for Optimization Analysis

Off-peak Energy Price ($/kW-hr)	0.03
On-Peak Energy Price ($/kW-hr)	0.15
Natural Gas Cost ($/Gigajoule)	7
PPC of Low Temp Receiver ($)	300
PPC of High Eff Receiver ($)	1500
Planning Period (years)	3

Table 7.3.2: Simulation Results for Low/High Efficiency Receiver Combinations

Number of LER Collectors in Loop	Net Electric Energy (MW-hr)	Total Gas Heat (MW-hr)	Total Field Heat (MW-hr)	Calculated Efficiency	Net On-Peak Energy (MW-hr)	Net Off-Peak Energy (MW-hr)	Number of HER Collectors in Loop
0	194668	25029.8	641217	0.605941	79446.4	115221	**6**
1	185655	30250.5	609775	0.576229	77845.8	107809	**5**
2	176069	36150.7	575871	0.544190	76156.3	99913.1	**4**
3	165906	42266.4	539989	0.510283	74222.1	91684.1	**3**
4	155335	48528.8	502612	0.474962	72051.4	83283.4	**2**
5	144399	54620.8	464203	0.438665	69608.5	74790.0	**1**
6	133279	60301.2	425462	0.402056	66884.5	66394.1	**0**

Table 7.3.3: Results of Collector Field Optimization

Number of LER Collectors in Loop	On-Peak Revenue ($ million)	Off-Peak Revenue ($ million)	Annual Revenue ($ million)	Gas Cost ($ million)	Receiver PPC ($ million)	Annual Cost ($ million)	Planning Period Benefit ($ million)
0	11.9170	3.4566	15.3736	0.6856	10.2240	10.9096	4.4640
1	11.6769	3.2343	14.9111	0.8286	8.8608	9.6894	5.2217
2	11.4235	2.9974	14.4208	0.9902	7.4976	8.4878	5.9330
3	11.1333	2.7505	13.8838	1.1577	6.1344	7.2921	6.5917
4	10.8077	2.4985	13.3062	1.3293	4.7712	6.1005	7.2057
5	10.4413	2.2437	12.6850	1.4961	3.4080	4.9041	7.7808
6	10.0327	1.9918	12.0245	1.6517	2.0448	3.6965	8.3280

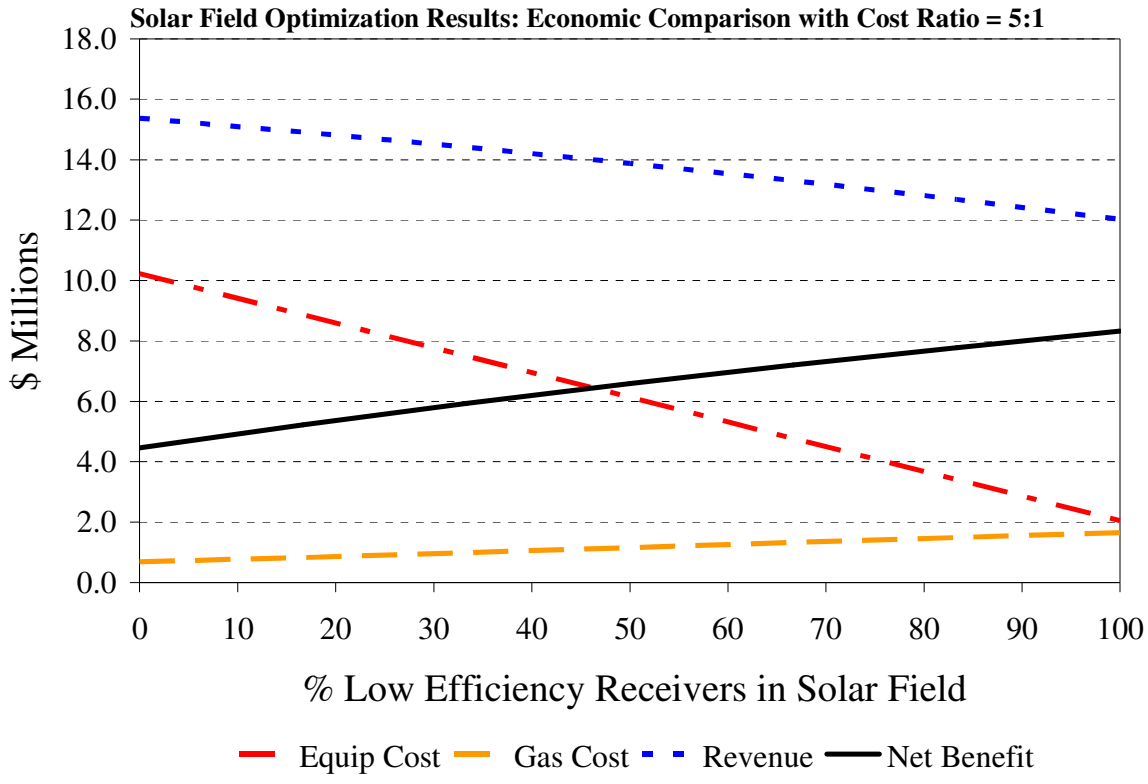

Figure 7.3.1: Graphical Results of Collector Field Optimization with High Eff. to Low Eff. Receiver Cost Ratio = 5:1

The results suggest that the maximum annualized planning period benefit would be realized with a solar field comprised entirely of the proposed low efficiency receivers. The slope of the equipment cost curve is visibly greater than the slope of the revenue curve, indicating that the incremental loss of revenue from converting an additional SCA position to low efficiency receivers is smaller than the decrease in cost (Cost Savings > Revenue Loss).

It is possible that the cost differential between the high and low efficiency receivers was overestimated. To account for an inflated cost ratio, a second optimization analysis was conducted using a high efficiency to low efficiency receiver cost ratio of 3:1. These optimization results are displayed in Figure 7.3.2.

Using the new cost ratio, as the number of low efficiency receivers increases the equipment cost and revenue appear to decrease at nearly the same rate. The net benefit is nearly constant, but appears to peak between 20 and 50 percent low efficiency receivers. A magnified graph of net benefit more clearly emphasizes the optimal collector arrangement.

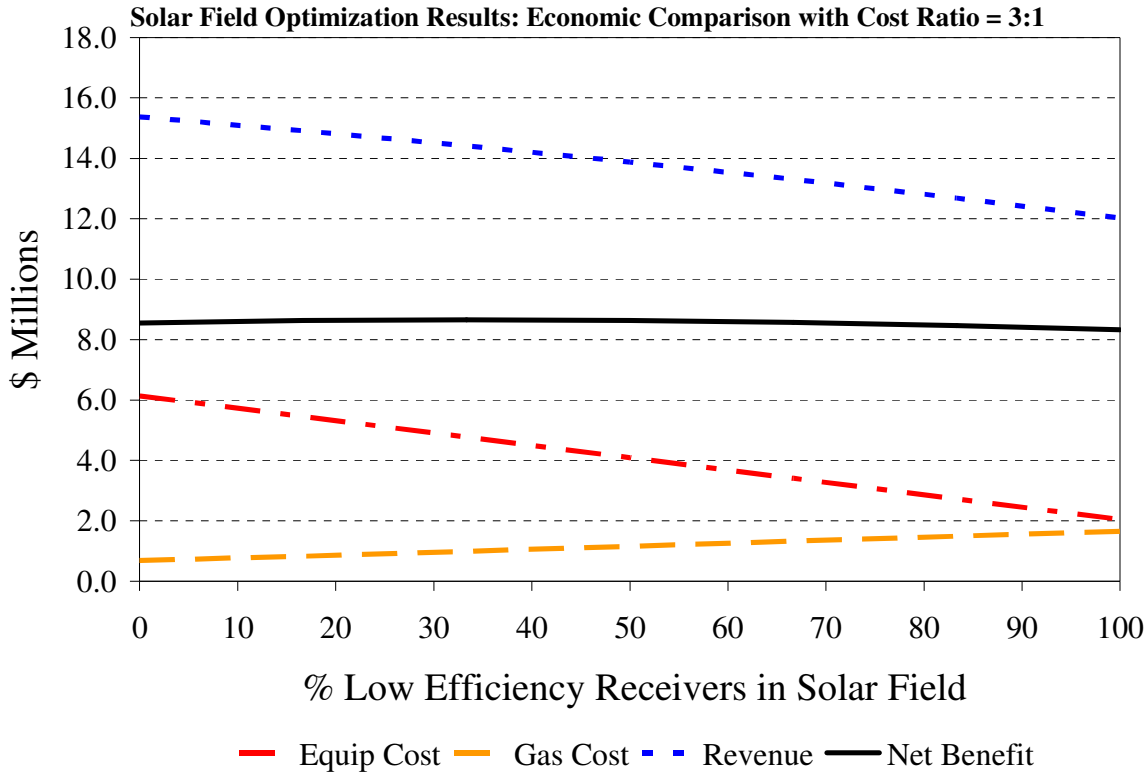

Figure 7.3.2: Graphical Results of Collector Field Optimization with High Eff. to Low Eff. Receiver Cost Ratio = 3:1

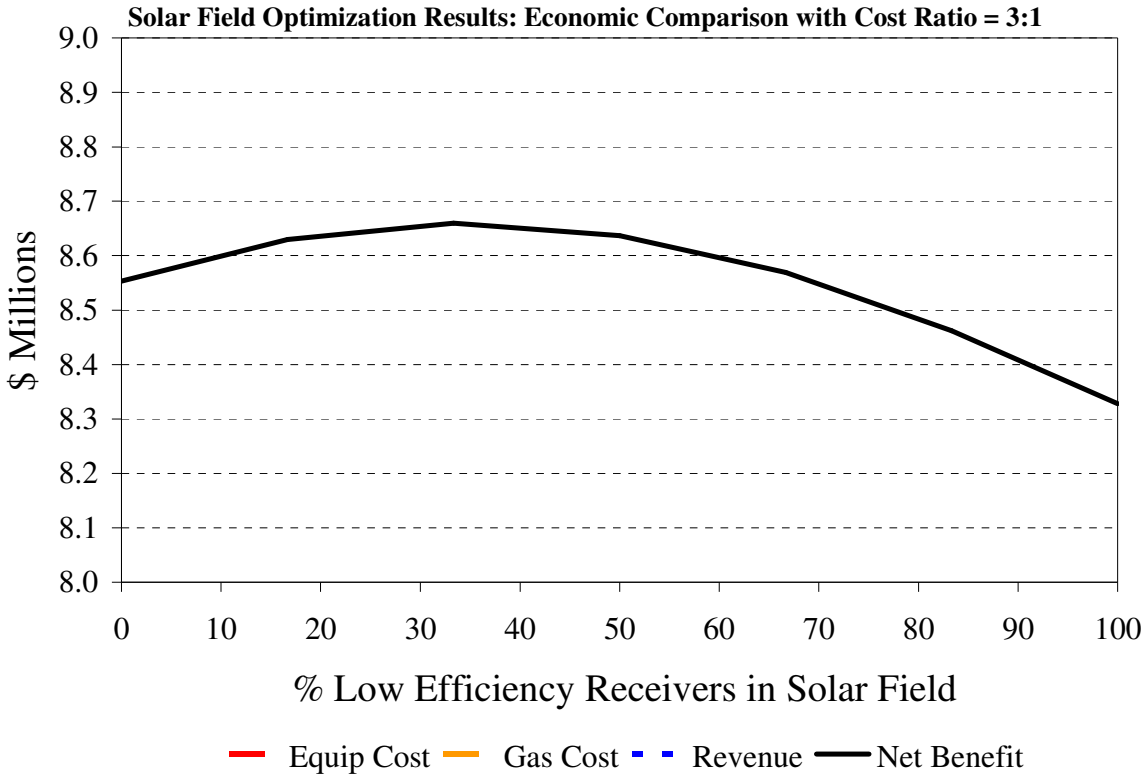

Figure 7.3.3: Magnified Net Benefit vs. % Low Efficiency Receiver Graph

Assuming a 3:1 cost ratio, a collector field comprised of approximately one third low efficiency receivers and two thirds high efficiency receivers will be the most economically beneficial. This corresponds to each loop having low efficiency receivers in the first two SCA positions and high efficiency receivers in the last four SCA positions. Figure 7.3.4 shows the annualized planning period benefit as a function of % low efficiency receivers in the field for several different cost ratios. The cost of the LER collectors was kept constant at $300 while adjusting the HER collector cost accordingly, so the benefit from using 100% LER collectors is the same for each case. As the Figure shows, the only cost ratio yielding the maximum benefit with no LER collectors in the field is the 2:1 ratio, and it is unlikely that the costs of the two receivers would be that close in value. The high relative cost of the solar-selective coating and of evacuating and maintaining the annulus vacuum would more than likely result in a cost ratio much larger than 2:1.

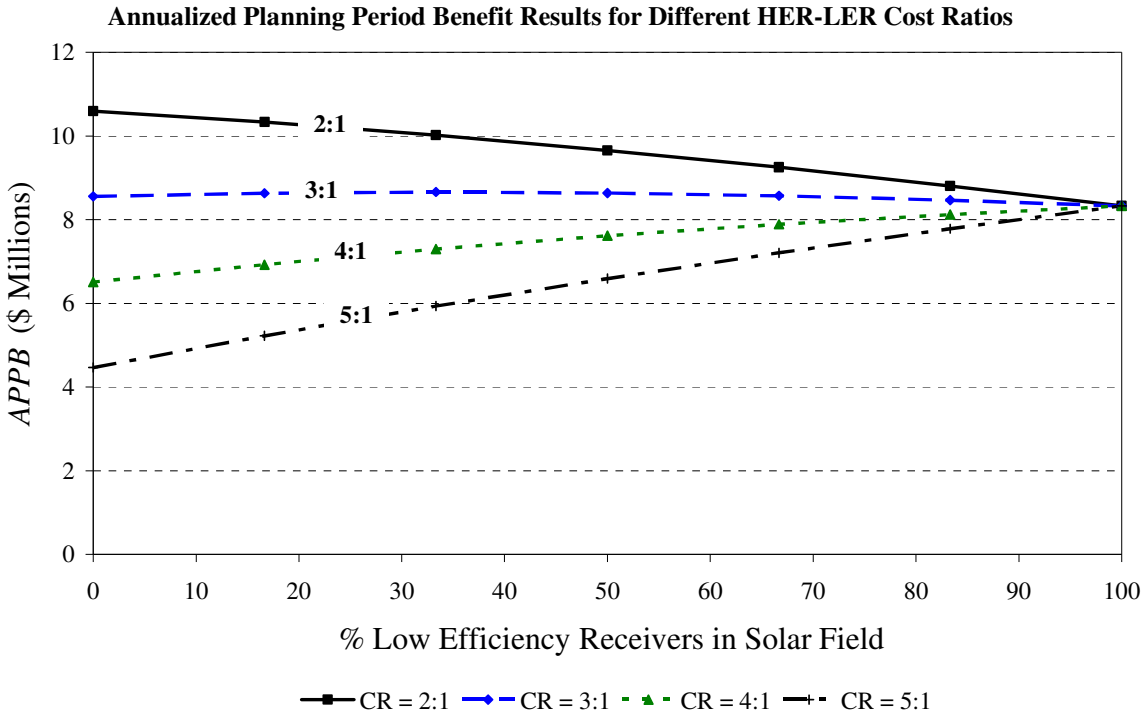

Figure 7.3.4: Annualized Planning Period Benefit of Collector Field Designs for Various High-to-Low Efficiency Receiver Cost Ratios

Although the actual cost differential of the high and low efficiency receivers is unclear, analysis of several cost ratios leads to the conclusion that the current approach of using only the highest efficiency receiver tubes in the collector field is not optimal. The important conclusion from this analysis is that employing some number of low efficiency receivers will increase the overall economic benefit of SEGS plant operation, confirming the initial hypothesis of this study. Since current SEGS units use only the highest efficiency collectors, this is a significant and innovative observation that could make SEGS plants more economically competitive in the electric power industry. These conclusions should endorse the need for further research on this subject.

CONCLUSIONS

This thesis has presented an effective method for modeling the collector field and energy conversion plant of a typical SEGS facility, as well as techniques for determining the optimal arrangement of collector types in a SEGS solar field for maximum economic benefit. Individual collector efficiency models were developed from SEGS test loop data and used to simulate the performance of the solar field. The energy conversion plant was also modeled based on performance data from SEGS. A thermal resistance model was developed to calculate the theoretical thermal performance of proposed low efficiency and high efficiency receiver tubes. It was initially hypothesized that employing low efficiency receivers in the cold end of the collector loops, while decreasing the total heat collection, would ultimately lower costs and increase the economic benefit of power production.

The SEGS solar field was simulated for various combinations of HER and LER collectors. An annualized planning period benefit analysis, assuming a 3 year planning period and appropriately using a simplified present worth analysis, of the various simulated heat productions and power outputs substantiated the initial hypothesis. Although the actual equipment costs of the low and high efficiency receivers are not certain, results for multiple estimated cost ratios indicated that employing low efficiency receivers, to some extent, in the field would maximize economic benefits.

To more accurately and precisely evaluate the economics behind a collector field with a mixture of high and low efficiency receivers, it is recommended that an in depth cost analysis of both receiver types be conducted. Such an analysis should include manufacturing and installation costs, as well as forecasted maintenance costs. The high efficiency receiver would likely incur higher maintenance costs, as the vacuum in the annulus has proven to be easily compromised, leading to decreased performance and decomposition of the solar-selective coating. The low efficiency receiver already has air in the annulus and employs a more durable coating, making it less susceptible to degradation.

Another recommendation is to build a single test receiver tube, in a laboratory setting, that can be used to obtain experimental heat loss data for any proposed receiver tube

configurations. Experimental results from such tests could be used to improve the original collector efficiency models. As discussed, these models were based on a qualitative analysis of SEGS efficiency data, because no experimental data for optical efficiency or heat loss was available for the different collector types. Since measuring heat losses from collectors in the field is disruptive to the operation of the plant, the most feasible approach is to build a single test receiver to run under simulated solar field conditions. Heat loss test results could also be used to verify the validity of the theoretical resistance models.

The conclusions gathered from this project should encourage further research into the use of inexpensive but robust low-technology receivers, without vacuum insulation, in the low temperature portions of SEGS solar collector fields. The apparent economic benefit from employing these collectors could make solar thermal power more competitive with traditional forms of large-scale electricity production. With the design of several new solar thermal facilities underway in the Southeastern US and other areas of the World, the innovative collector field designs explored in this study could prove to be advantageous to these future plants, as well as to the refurbishments of the nine SEGS units already in operation.

REFERENCES

1. BEES, NRC Letter Report: Critique of the Sargent and Lundy Assessment of Concentrating Solar Power Cost and Performance Forecasts. Board on Energy and Environmental Systems (BEES), Nov. 22, 2002.

2. Bliss, R. W. , Jr, "Derivations of Several 'Plate-efficiency factors' Useful in the Design of Flat-Plate Solar Heat Collectors", *Solar Energy*, Vol 3, No. 4, 1 October 1959.

3. Churchill, S.W., and H.H.S. Chu, "*Correlating Equations for Laminar and Turbulent Free Convection from Horizontal Cylinder*", Int. Journal of Heat and Mass Transfer, Vol. 18, 1975.

4. Dow Chemical, *"Form No. 176-01469-1101 AM: Syltherm 800 Product Information*", Dow Chemical Company, 2001

5. Dudley, V., et al, *"Efficiency Testing of SEGS Parabolic Trough Collector",* Proceedings of the 1993 American Solar Energy Society Annual Conference, Washington, D.C., April 22–28, 1993.

6. Duffie, John A., and William A. Beckman. Solar *Engineering of Thermal Processes*. New York: John Wiley & Sons, Inc., 1980.

7. Energy Blog, *"Parabolic Trough Solar."* The Energy Blog. 3 Sept. 2005. 24 June 2007 <http://thefraserdomain.typepad.com/energy/>.

8. Energy Information Administration. U.S. Department of Energy. Jan. 2007, available online at <www.eia.doe.gov>.

9. Forristal, R. *Heat Transfer Analysis and Modeling of a Parabolic Trough Solar Receiver Implemented in Engineering Equation Solver*. National Renewable Energy Laboratory. Golden, CO, 2003.

10. Fuller, S.K., *"Guidance on Life-Cycle Cost Analysis Required by Executive Order 13123"*. Federal Energy Management Program, Dept. of Energy. Washington, 2005.

11. Gnielinski, V., "*New Equations for Heat and Mass Transfer in Pipe and Channel Flows*", International Chemical Engineering, Vol. 16, p. 359, 1976.

12. Hilpert, R., Forsch. Geb. Ingenieurwes., 1933.

13. Hottel, H. C., and A. Whillier, “Evaluation of Flat Plate Collector Performance”, Transactions of a Conference on the Use of Solar Energy, University of Arizona, 1955.

14. Incropera, Frank P., and David P. De Witt. *Introduction to Heat Transfer*. 4th ed. New York: John Wiley & Sons, Inc., 2002.

15. Jeter, Sheldon M. *Optical and Thermal Effects in Linear Solar Concentrating Collectors*. Diss. Georgia Institute of Technology, 1979.

16. Kennedy, C.E. *Review of Mid- to High- Temperature Solar Selective Absorber Materials*. National Renewable Energy Laboratory. Golden, CO, 2003.

17. Odeh, S D., G L. Morrison, and M Behnia. "*Modeling of Parabolic Trough Direct Steam Generation Solar Collectors*." Solar Energy, Vol. 62, pp. 395-406 , 1998.

18. OSET, *“Solar Trough Power Plants*”. Office of Solar Energy Technologies (OSET): U.S. Dept of Energy. 2000.

19. Price, Henry W., and Stephen Carpenter. *The Potential for Low-Cost Concentrating Solar Power Systems*. National Renewable Energy Laboratory. Golden, CO, 1999.

20. Quaschning, Volker. *"Technical and Economical System Comparison of Photovoltaic and Concentrating Solar Thermal Power Systems Depending on Annual Global Irradiation."* Solar Energy 77 (2004): 171-178.

21. Raithby, G.D., and K.G.T. Hollands, “*A General Method of Obtaining Approximate Solutions to Laminar and Turbulent Free Convection Problems*,” in T.F. Irvine and J.P. Hartnett, Eds., *Advances in Heat Transfer*, Vol. 11, Academic Press, New York, 1975.

22. Ratzel, A. C., C. E. Hickox, and D. K. Gartling. *“Techniques for Reducing Thermal Conduction and Natural Convection Heat Losses in Annular Receiver Geometries”*. Heat Transfer in Solar Energy Systems; Proceedings of the Winter Annual Meeting of ASME, Atlanta, Ga, 27 Nov. 1977. pp. 17-24. 1977

23. Solutia, *“Technical Bulletin 7239115B: Therminol VP-1 Heat Transfer Fluid”*. Solutia Inc., 1999.

24. Sweet, William. *Kicking the Carbon Habit*. New York, Columbia UP, 2006.

25. Thekaekara, M. P. and A. J. Drummond. “*Standard Values of the Solar Constant and its Spectral Components*”. Nature, Vol. 229, pp. 6-9, 1971.

26. U.S. Dept. Of Energy, "*Energy Secretary Announces $170 Million Solicitation for Solar Energy Technologies*" available on line at http://www.energy.gov/news/3790.htm. June 28, 2006.

27. Wade, William R., and Wayne S. Slemp. *Measurements of Total Emittance of Several Refractory Oxides, Cermets, and Ceramics for Temperatures From 600 F to 2000 F*. NASA. Washington, 1962.

28. Winter, C.-J., R.L. Sizmann, and L.L. Vant-Hull, eds. *Solar Power Plants*. New York: Springer-Verlag, 1991.